

Dynamic Imaging of Lipid Membranes by Means of Water

Thèse N° 9270

Présentée le 5 avril 2019

à la Faculté des sciences et techniques de l'ingénieur

Chaire Julia Jacobi de photomédecine - Laboratoire de biophotonique fondamentale

Programme doctoral en photonique

pour l'obtention du grade de Docteur ès Sciences

par

Orly Bagunu TARUN

Acceptée sur proposition du jury

Prof. L. Thévenaz, président du jury

Prof. S. Roke, directrice de thèse

Prof. G. Pabst, rapporteur

Prof. P. Wittung-Stafshede, rapporteuse

Prof. A. Radenovic, rapporteuse

2019



ÉCOLE POLYTECHNIQUE
FÉDÉRALE DE LAUSANNE

Achievements stem from ambitions,
supported by the belief and
the persistent attitude to succeed.
The seed of which are dreams.
Never stop dreaming!
— Orly B. Tarun

To my parents, brothers, and sisters,
this is our achievement. . .

Acknowledgements

First, I would like to express my warmest gratitude to my supervisor Prof. Sylvie Roke for giving me the opportunity to work on my Ph.D. at the Laboratory for Fundamental Biophotonics (LBP). Coming from across the globe, Sylvie bestowed me her trust without any assurance except for the few skype interviews and motivation letters that I have sent. My almost five years of Ph.D. were not easy, especially my first year when I struggled to be an effective researcher. Through the years, Sylvie continuously provided support and guidance to help me get through my Ph.D. I am forever grateful for all the discussions about science, writing and personal advice about life. I have learned a lot under her guidance that will forever stay with me for the rest of my life.

I would also like to thank my committee a priori, Prof. Luc Thévenaz, Prof. Georg Pabst, Prof. Aleksandra Radenovic, and Prof. Pernilla Wittung-Stafshede. Their inputs can only make this thesis better.

I would like to thank our collaborators in Linz, Prof. Peter Pohl, Dr. Christof Hanneschlaeger, and Dr. Lukas Winter. Nine months into my Ph.D., I learned how to form freestanding lipid bilayers from Christof and Lukas. This timely collaboration, 3 months before my candidacy allowed me to survive my first year of PhD and propelled me to a wonderful scientific journey. I have enjoyed working with you and I am happy that our efforts were fruitful.

I would like to thank the past and present members of LBP. To Carlos Macias-Romero, then post-doc for helping me in my first year of Ph.D., to Nikolay Smolentsev, Yixing Chen, Cornelis Lütgebaucks, Halil Okur and Arianna Machioro with whom I have shared most of my Ph.D. years. Special mention to my past and present office mates throughout the years: Nathan Dupertuis, Jan Dedic, Sergy Kulic, Vitalijs Zubkovs, Siyuan Wang and Yvonne Hu, you have made Ph.D. life easier with all the shared laughter. I would like to give special mention to my batchmates in the lab: Evangelia Zdrali and Marie Didier with whom I have shared the ups and downs of my Ph.D. years. To the new generation of Ph.D. students especially Maksim Emeremchev who helped me a lot in my last year of Ph.D., to Marie Bichoff, Theresa Schönfeldova and David Roesel for the wonderful shared moments during lunch time. To Igor (and Anjali) for the countless dinners. Thank you to Nathan and Claire for teaching me how to speak French and to how to ski! My friends at LBP have withstood my wonderful jokes throughout the years and I have enjoyed spending time with each one of them. I would also like to thank our secretary Rebecca Veselinov for helping me with countless administrative chores.

At this point, I would like to thank all my friends, both from Switzerland and from the

Acknowledgements

Philippines. When Ph.D. life gets tough, friends are always there to relieve you of the stress and help you to take one more step forward in life.

First and foremost, I would like to thank Miguel P. Sison, my best friend and my roommate. I came to Lausanne, half a globe away from my hometown, knowing that a familiar face awaits me. In my Ph.D. years, I have seen many facets of life and I have shared these experiences with Miguel. I learned how to cook and I have enjoyed the countless discussions during dinner. I have met my better half coming to Lausanne. It all started with the knowledge that someone with whom I have shared friendship for over a decade was doing his Ph.D. in Lausanne. It was a wonderful adventure and I am happy that I did it with Miguel.

I would also like to thank my Atlantis friends, David Nguyen, Dino Carpentras (+ Miguel and almost member Emilio Morales). I enjoyed the countless dinners. Though we are now in different paths, I wish our roads will cross once more.

I would like to thank my friends from the Philippines, my DOTA friends for all the laughter and countless game sessions: Jaya, Janno, SD, Thirdy, Atchong, and Master.

I would like to express my deepest love and gratitude to my family: To Mama and Papa, Kuya Al, Ate Cynthia, Ate Millet, Kuya Ado, Kuya Balds, Kuya Wilbert, Kuya Emong, Roxinne, and Anjali. Though they are across the globe, they have always been there to support me, always ready to give me their time and love.

Lastly, I would like to thank my fiancée, Séverine Coquoz for all the love and support. Coming from a country where the sun is 24/7 and going to Switzerland where the sun is sometimes an expensive commodity, it is often moody weather. With Séverine, I have a new light. Happiness is as easy as seeing her and spending time with her. I am looking forward to spending the rest of my life with you and building our family together. I love you.

Lausanne, 16th January 2019

Orly .B. Tarun

Abstract

Lipid membranes are dynamic and self-assembled structures whose composition critically determines the properties of membranes of cells and organelles. They are complex and in a constant state of flux. However, molecular-level understanding of lipid membranes is based on spectroscopic measurements and molecular dynamics simulations of simplified lipid monolayer systems. As spectroscopic measurements rely on spatial and temporal averaging and are necessarily linked to mean field models, information about the molecular interactions and their spatiotemporal evolution in real membranes is currently unavailable. In this thesis, we use high throughput wide-field second harmonic (SH) microscopy to image water-membrane interactions at sub-second time scale to follow the spatiotemporal evolution of membrane fluctuations in freestanding lipid membranes.

To achieve this, we improve the throughput of nonlinear SH microscope by 2-3 orders of magnitude and integrate the apparatus to form freestanding lipid membranes for simultaneous electrical and optical characterization of membranes. We show in a series of experiments involving symmetric and asymmetric freestanding lipid membranes, and changes in the ionic and pH content of adjacent solutions, that the non-resonant response of water can be SH imaged on sub-second time scales. This water response has a non-random orientational distribution because of charge-dipole and hydrogen bonding interactions with the lipid head groups. We use this water response as a contrast mechanism to image the spatiotemporal evolution of membrane fluctuations.

We first characterize the formation of freestanding lipid membranes and investigate how oil redistributes within bilayers after formation. Focusing on hexadecane and squalene, we show using SH imaging that the annulus of freestanding lipid bilayers prepared with hexadecane is narrower compared to those prepared with squalene, indicating that less oil is present within bilayers prepared with hexadecane. We track the diffusion of excess oil droplets within the bilayer and show that hexadecane droplets follow directed diffusion, moving from the center of the bilayer to the annulus, with a diffusion coefficient similar to single lipids, whereas squalene shows no directed motion with a diffusion coefficient similar to lipid domains. We discuss the observed differences in terms of different coupling mechanisms between the oil and the lipid molecules induced by the different chemical structures of the oils. Hexadecane can stay within a single leaflet and can diffuse through the liquid phase of the lipids whereas squalene is bigger than a single leaflet and also more branched, so it couples to both leaflets and move slower.

Using SH imaging, we probe the diffusion of charged lipid domains at sub-second time

Abstract

scale and construct electrostatic membrane potential maps of asymmetric membranes. The average membrane potential depends quadratically on an applied external bias, which is modeled by nonlinear optical theory. We observe spatiotemporal fluctuations in the membrane potential on the order of 100 mV implying that membranes are dynamic not only in structure but also in their membrane potential landscape.

We probe the interactions of divalent cations with water and negatively charged free-standing lipid bilayers and show that at physiological concentration, Ca^{2+} , Ba^{2+} and Mg^{2+} induce short-lived (<500 ms) and micron-sized ($\sim 1.5 \mu\text{m}$) domains of ordered interfacial water. We convert the SH intensity into membrane hydration free energy, and membrane-ion binding dissociation constant maps. We obtain trends in the order $\text{Ca}^{2+} > \text{Mg}^{2+} > \text{Ba}^{2+}$, for all quantities. We quantify the ion binding dissociation constants and observe domain values that deviate up to 4 orders of magnitude from average binding dissociation constants. The transient structural domains exhibit membrane potential fluctuations of up to -386 mV (with $\Delta G = 28.6 \text{ kT}$) induce strain in the membrane resulting in temporal and spatial variations in membrane curvature.

Lastly, we perform spatiotemporal SH imaging of operational voltage-gated alamethicin ion channels in freestanding lipid membranes surrounded by aqueous solution on either side having the same physiologically relevant salt concentration. We show that the opening and closing of ion channels by an external bias lead to changes in SH intensity. Combining SH imaging with capacitance measurements, the changes in SH intensity is due to changes in the orientational distribution of water molecules induced by electric field gradients. Only a fraction, that is, 10^{-4} of the transported ions arrives at the hydrated membrane interface, leading to interfacial electrostatic changes on the time scale of a second. We quantify the spatiotemporal distribution of ion channels and record their activity during gating. Regions with a high density of ion channels exhibit a lower rate of interfacial charge buildup, which is likely caused by crowding. Our study shows that ion transport along the membrane, which is thought to be involved in the propagation of action potential, is taking place over seconds. The observation suggests a more complex mechanism for the propagation of action potentials.

In the above findings, we highlight the importance of spatiotemporal fluctuations that are linked to chemical, electrical and mechanical properties of the membrane and highlight the multi-scale response of lipid membranes to external stimuli and vice versa. On a more fundamental level, the influence of structural and temporal heterogeneity needs to be included in biochemical, physical and molecular models of membranes.

Keywords: water, membranes, second-harmonic imaging, lipids, surface potential, specific ion effects, membrane curvature, ion channels, ion transport, membrane fluctuations.

Résumé

Les membranes lipidiques sont des structures dynamiques et auto-assemblées dont la composition détermine de manière critique les propriétés des membranes des cellules et des organelles. Elles sont complexes et dans un état de flux constant. Néanmoins, la compréhension des membranes au niveau moléculaires est fondée sur des mesures spectroscopiques, et des simulations de dynamique moléculaire de systèmes à monocouche simplifiés. Comme les mesures spectroscopiques reposent sur des moyennes spatiales et temporelles et sont nécessairement liées à des modèles de champ moyen, l'information sur les interactions moléculaires et leur évolution spatiotemporelle dans les membranes réelles est indisponible à ce jour. Dans cette thèse, nous utilisons la microscopie de seconde harmonique à grand champ et rendement élevé pour imager les interactions entre l'eau et la membrane, à une échelle temporelle inférieure à la seconde, et pour suivre les évolutions spatiotemporelles des fluctuations de membranes lipidiques autoportantes.

Pour réaliser cela, nous améliorons le rendement d'un microscope non-linéaire à seconde harmonique par deux à trois ordres de grandeur, et nous y intégrons le montage pour former des membranes lipidiques autoportantes, afin de pouvoir caractériser simultanément les propriétés électriques et optiques des membranes. Par une série d'expériences impliquant des membranes lipidiques autoportantes symétriques et asymétriques, ainsi que des changements ioniques et de pH dans les solutions aqueuses environnantes, nous montrons que la réponse non résonnante de l'eau peut être imagée par seconde harmonique à des échelles temporelles inférieures à la seconde. Cette réponse a une distribution non aléatoire à cause des interactions charge-dipôle et de liaisons hydrogène avec les groupes de tête des lipides. Nous utilisons cette réponse comme un mécanisme de contraste pour imager l'évolution spatiotemporelle des fluctuations de membrane.

Nous caractérisons premièrement la formation des membranes lipidiques et étudions comment l'huile se redistribue à l'intérieur des bicouches après leur formation. En examinant les cas de l'hexadécane et du squalène, nous montrons grâce à l'imagerie par seconde harmonique que la couronne des bicouches lipidiques autoportantes préparées avec l'hexadécane est plus étroite que celle des bicouches préparées avec le squalène. Nous traquons la diffusion des gouttelettes d'huile en excès à l'intérieur de la bicouche, et démontrons que les gouttelettes d'hexadécane se diffusent selon une direction spécifique, depuis le centre de la bicouche vers sa couronne, avec un coefficient de diffusion similaire à celui des lipides individuels. A contrario, les gouttelettes d'hexadécane n'ont aucune direction préférentielle de diffusion, avec un coefficient de diffusion similaire à celui des domaines lipidiques. Nous discutons

les différences observées en terme de mécanismes de couplage différents entre l'huile et les molécules lipidiques, induits par les différences de structures chimiques des huiles. L'hexadécane peut rester à l'intérieur d'un feuillet lipidique unique, et peut se diffuser à travers la phase liquide des lipides. À l'opposé, les molécules de scalène sont plus grandes qu'un feuillet unique, et plus ramifiées que celles d'hexadécane. Par conséquent elles se couplent aux deux feuillets de la bicouche lipidique et se déplacent plus lentement.

En utilisant l'imagerie par seconde harmonique, nous sondons la diffusion de domaines lipidiques chargés à une échelle temporelle inférieure à la seconde, et construisons des cartographies du potentiel électrostatique de membranes asymétriques. Le potentiel de membrane moyen dépend quadratiquement du biais externe appliqué, ce qui est modélisé par la théorie de l'optique non-linéaire. Nous observons des fluctuations spatiotemporelles du potentiel de membrane de l'ordre de la centaine de millivolts. Ceci implique que les membranes sont dynamiques non seulement dans leur structure mais aussi dans leur distribution spatiale du potentiel de membrane.

Nous sondons les interactions de cations divalents avec l'eau et les bicouches lipidiques autoportantes, et montrons qu'à la concentration physiologique les ions Ca^{2+} , Ba^{2+} and Mg^{2+} induisent des domaines de réarrangement de l'eau à l'interface, de courte durée de vie (<500ms) et de taille micrométrique ($\sim 1.5 \mu\text{m}$). Nous convertissons l'intensité détectée de seconde harmonique en cartographie de l'énergie libre d'hydratation de la membrane, et en cartographie des constantes de dissociations membrane-ions. Nous obtenons des tendances dans l'ordre $\text{Ca}^{2+} > \text{Mg}^{2+} > \text{Ba}^{2+}$, pour toutes les quantités. Nous quantifions les constantes de dissociations ioniques, et nous observons des valeurs pour les domaines qui dévient de plus de quatre ordres de grandeur par rapport aux valeurs moyennes des constantes de dissociation. Ces domaines éphémères se caractérisent par des fluctuations du potentiel de membrane allant jusqu'à -386mV (avec $\Delta G = 28.6 \text{ kT}$) qui induisent des contraintes dans la membrane, et causent ainsi des variations spatiales et temporelles de sa courbure.

Enfin, nous réalisons une imagerie spatiotemporelle par seconde harmonique de canaux ioniques d'alaméthicine commandés par le voltage. Ces canaux sont répartis dans des membranes lipidiques autoportantes, environnées des deux côtés par des solutions aqueuses dotées des mêmes concentrations de sels ioniques, correspondant à un milieu physiologique. Nous observons que l'ouverture et la fermeture des canaux ioniques par un biais de potentiel externe conduit à des changements d'intensité de la seconde harmonique détectée. En combinant l'imagerie par seconde harmonique avec des mesures de capacitance, nous montrons que ces changements sont dus à des modifications de distribution de l'orientation des molécules d'eau causées par des gradients du champ électrique. Seule une fraction (de l'ordre de 0.01%) des ions transportés parvient à l'interface de la membrane hydratée, conduisant à des changements électrostatiques à l'interface à l'échelle temporelle de la seconde. Nous quantifions la distribution spatiotemporelle des canaux ioniques et enregistrons leur activité durant leur déclenchement. Les régions de la membrane avec une grande densité de canaux possèdent un taux plus bas d'accumulation de charges interfaciales, ce qui est probablement causé par un encombrement. Notre étude montre que le transport des ions le long de la membrane, qui est supposé être impliqué dans la propagation du potentiel d'action, se déroule en

quelques secondes. L'observation suggère un mécanisme plus complexe pour la propagation des potentiels d'action.

Dans les découvertes évoquées ci-dessus, nous soulignons l'importance des fluctuations spatiotemporelles qui sont liées aux propriétés chimiques, électriques, et mécaniques de la membrane, ainsi que la réponse -à plusieurs échelles- des membranes lipidiques aux stimuli externes, et vice-versa. À un niveau plus fondamental, les modèles biochimiques, physiques, et moléculaires des membranes doivent inclure l'influence de leur hétérogénéité structurelle et temporelle.

Mots-clés : eau, membranes, imagerie par seconde harmonique, lipides, potentiel de surface, effets ioniques spécifiques, courbure de membrane, canaux ioniques, transport des ions, fluctuations de membrane.

Contents

Acknowledgements	iii
Abstract (English/Français)	v
List of figures	xiii
List of tables	xvi
1 Introduction	1
1.1 Water and lipid membranes	1
1.1.1 A water window	1
1.1.2 From molecular-level information to microscopic function	2
1.2 State of the art in membrane imaging research	3
1.2.1 Model membranes	4
1.2.2 Approaches to membrane imaging: Advantages and limitations	6
1.2.3 State of the art in surface-sensitive nonlinear optical imaging methods	8
1.3 Second harmonic generation	9
1.4 Open opportunities in membrane imaging research	13
1.4.1 Improving the throughput of SH microscopes	13
1.4.2 Membrane asymmetry	13
1.4.3 Ion-specific effects	14
1.4.4 Ion channels	15
1.5 This Thesis	17
2 Experimental Details & Methodology	19
2.1 SH Microscope: Characterization and Throughput	20
2.1.1 Optical Setup	20
2.1.2 Characterization of the Fundamental Beam	20
2.1.3 Characterization of SH Microscope	22
2.1.4 Polarization Sensitivity of the SH microscope	23
2.1.5 Improving the Imaging Throughput of Nonlinear Microscopes	24
2.2 Sample Preparation, Formation and Characterization of Freestanding Lipid Bilayers	26
2.2.1 Lipids.	26

Contents

2.2.2	Preparing $\sim 100\text{-}\mu\text{m}$ -aperture in a $25\text{-}\mu\text{m}$ -thick Teflon Film.	27
2.2.3	Chamber design and assembly.	29
2.2.4	Formation of horizontal freestanding lipid bilayers	29
2.3	Methods to characterize horizontal freestanding lipid bilayers	31
2.3.1	Electrical Measurements	32
2.3.2	Characterization of freestanding lipid bilayers	33
3	The interaction of oil and lipids in freestanding lipid bilayer membranes	35
3.1	Introduction	36
3.2	Materials and Methods	36
3.2.1	Chemicals and lipids	36
3.2.2	Freestanding horizontal planar lipid bilayers	37
3.2.3	Imaging experiments	37
3.2.4	White light imaging and tracking	37
3.3	Results & Discussions	37
3.4	Summary and Conclusions	41
3.5	Appendix	43
3.5.1	Measurement of the width of the annulus	43
3.5.2	Diffusion of oil droplets for bilayers prepared with hexadecane and squalene	43
4	Label-free and charge-sensitive dynamic imaging of lipid membrane hydration on millisecond time scales	45
4.1	Introduction	46
4.2	Materials and Methods	47
4.2.1	Chemicals and lipids	47
4.2.2	Freestanding horizontal planar lipid bilayers	47
4.2.3	Imaging conditions and data analysis	47
4.3	Results & Discussions	48
4.3.1	SH Imaging of Membrane Hydration	48
4.3.2	SH Imaging of Membrane Structure and Dynamics	50
4.3.3	SH Imaging of Membrane Potential	51
4.4	Summary and Conclusions	54
4.5	Appendix	54
4.5.1	Verification of Transmembrane Asymmetry by Capacitance Minimization	54
4.5.2	Nonvanishing Polarization Combinations	55
4.5.3	Numerical Computations.	56
5	Divalent ions induce transient domains of interfacial ordered water in lipid membranes	59
5.1	Introduction	60
5.2	Materials and Methods	60
5.2.1	Chemicals and lipids	60
5.2.2	Second harmonic (SH) imaging.	61

5.3	Results & Discussions	61
5.3.1	Spatiotemporal ion-specific effects	61
5.3.2	Quantifying membrane potential and free energy changes.	62
5.3.3	From transient membrane structure to curvature.	64
5.4	Summary and Conclusions	66
5.5	Appendix	66
5.5.1	Spatiotemporal autocorrelation of ion-induced domains	66
5.5.2	The intensity distribution of the ion-induced domains	67
5.5.3	Single frame correction for hyper-Rayleigh scattering	68
5.5.4	From SH intensity to surface potential difference	68
6	Spatiotemporal imaging of water in operating voltage-gated ion channels reveals the slow motion of interfacial ions	71
6.1	Introduction	72
6.2	Materials and Methods	73
6.2.1	Chemicals and lipids	73
6.2.2	Formation of freestanding lipid bilayers and incorporation of alamethicin peptides	73
6.2.3	Second harmonic (SH) imaging.	73
6.2.4	Capacitance measurements of activated channels	74
6.3	Results & Discussions	74
6.3.1	SH imaging of ion channels	75
6.3.2	The interfacial structure	75
6.3.3	Crowding and spatiotemporal effects	77
6.4	Summary and Conclusions	78
6.5	Appendix	78
6.5.1	Estimation of the number of incorporated ion channels	78
7	Summary & Outlook	81
7.0.1	Summary	81
7.0.2	Outlook	82
8	List of Publications	85
	Bibliography	106
	Curriculum Vitae	107

List of Figures

1.1	A water window to fundamental membrane processes	3
1.2	Diverse model membrane systems	5
1.3	Illustration of the different methods of imaging membranes	7
1.4	Energy diagram for a resonant and a non-resonant SHG.	10
1.5	Molecular sources for possible second harmonic scattering	12
1.6	Typical ordering of cations and anions in a Hofmeister series.	14
2.1	Schematic of the optical layout.	21
2.2	Characterization of the fundamental beam.	21
2.3	Point Spread Function (PSF) of the SH microscope and spectrum of pure water.	22
2.4	Pulse duration at the focus of the SH microscope.	23
2.5	Polarization sensitivity of the SH microscope.	24
2.6	Calculated imaging throughput.	26
2.7	Experimentally measured imaging throughput.	27
2.8	Chemical structures of the lipids used in this study.	28
2.9	Image of the punching device.	28
2.10	The freestanding lipid bilayer chamber.	29
2.11	The microscope mount for the bilayer chamber.	30
2.12	Modified microscope mount for temperature measurements.	30
2.13	Illustration of the formation of freestanding horizontal planar lipid bilayer.	31
2.14	Characterization of the freestanding horizontal planar lipid bilayers.	34
3.1	Second-harmonic (SH) imaging of freestanding lipid bilayers.	38
3.2	Second-harmonic (SH) and white-light imaging of oil and lipid interactions comparing hexadecane and squalene.	40
3.3	Possible mechanisms for the interaction of oil inside a lipid bilayer.	42
3.4	Measurement of the width of the annulus of freestanding membranes.	43
3.5	Diffusion of oil droplets.	44
4.1	SH imaging of membrane hydration.	48
4.2	SH imaging of water around liquid-ordered domains of charged lipids.	51
4.3	Voltage-sensitive SH imaging of the changes in membrane surface potential.	52
4.4	Capacitance as a function of applied bias U_0	54
4.5	Non-vanishing polarization combinations.	55

List of Figures

4.6	COMSOL simulation of an asymmetric membrane.	56
5.1	Divalent cations induce transient domains of ordered interfacial water.	62
5.2	Spatiotemporal dynamics of ion-induced ordered water domains.	63
5.3	Quantifying the free energy landscape of membranes.	65
5.4	Specific ion induced transient curvature.	66
5.5	Spatiotemporal autocorrelation of ion-induced domains for different divalent cations.	67
5.6	Average intensity distribution of domains at different electrolyte conditions. . .	68
5.7	Single frame SH images of ion-induced ordered water domains.	69
5.8	SH intensity as a function of applied external bias.	70
6.1	SH imaging of voltage-gated ion channel operation.	74
6.2	Dynamic electrical and spatiotemporal imaging of voltage-gated ion channel activity in lipid membranes.	76
6.3	Quantifying the spatiotemporal distribution of ion channel opening in membranes.	79
6.4	Macroscopic conductance-voltage curve of alamethicin channel in 500 mM KCl	80

List of Tables

1.1	List of commonly known ion channel related diseases.	16
5.1	Image averaged and single domain values of $\Delta\Phi_0$, $\Delta\sigma_0$, ΔG and K_D	64

1 Introduction

Lipid membranes are key components of living organisms. They are composed of dynamic and self-assembled lipid bilayer structures whose composition critically determines the structural and dynamical properties of the membranes of cells and organelles. Lipid membranes provide a diverse environment for protein segregation, transport, and signaling. To achieve this function, the hydrating environment is crucial.

The two main subjects of this thesis are water and lipid membranes, two key elements of life and two major subjects on their own. Here they are combined to achieve a holistic approach towards the molecular-level understanding of lipid membranes by means of water.

1.1 Water and lipid membranes

Water. The guiding principle of National Aeronautics and Space Administration (NASA) in the search for extraterrestrial life is "follow the water". A Google search on the importance of water results to: "All life forms contain water", "water is the molecule of life" and "water is the matrix of life." These associations intimately link water with the life forms on Earth [1]. For example, without water lipid membranes - the highly dynamic and complex lipid bilayer structures responsible for the integrity and survival of cells, cannot self-assemble and life, indeed, would not be possible.

Lipid membranes are key elements in the evolution of life [2], shielding cells from the hostile environment. They provide structure and compartmentalization to cells and organelles, regulate and control the transport of ions and nutrients through channels and pores, and mediate interactions between the internal and external environments of the cell [3].

1.1.1 A water window

Membranes coexist with water. As such, it is practical to study membranes through their interaction with water. Furthermore, all membrane processes require some form of interaction with

the active layer of water that hydrates them. However, most membrane studies have focused on using membrane-inserted probes or examining the phase changes in the hydrophobic core, e.g., lipids [4, 5, 6], steroids and sterols [7, 8, 9], thus focusing on lipid-lipid interactions (interaction energy <1 kT [10]). While these interactions are important, it ignores hydration, electrostatic interactions (e.g., charge-dipole 10-50 kT), hydrogen bonding (5-10 kT) and the influence of the electric double layer. These interactions are much stronger than lipid-lipid interactions and are expected to play an important role in membrane structure and function. Water as a molecular dipole responds to charges through charge-dipole interaction and forms hydrogen bonds with electronegative atoms. Thus, the response of water contains molecular level information that can be used to probe hydration, the presence of local charges and the influence of the electric double layer. Moreover, current understanding of water-membrane interactions is based on studies of simple water/lipid interface, which are systems that are not directly related to realistic membranes. This thesis aims to bridge that gap by providing a water window to molecular level interactions occurring in the electrical double layer of freestanding lipid membranes.

1.1.2 From molecular-level information to microscopic function

Our current understanding of membrane electrostatics and of chemical interactions occurring in the electrical double layer are mostly obtained from spectroscopic [11, 12, 13, 14, 15] or electrode-based [16, 17, 18, 19] methods. These approaches rely on spatial and temporal averaging because of technical limitations and are necessarily linked to mean field models. It is important to ask whether the dynamic behavior of membranes can be captured by averaging the spatial and temporal fluctuations in the system. This question is partly addressed by imaging water-membrane interactions that are interrelated to hydration, the presence of local charges, ionization states and membrane potentials. Such information, when imaged at sub-second time scale would provide a pathway to study the spatiotemporal evolution of membranes and link molecular-interactions to microscopic function.

Here, I demonstrate a unique imaging method that combines molecular level information with mesoscopic structural and dynamic information by imaging the hydration of freestanding lipid membranes at sub-second time scale. We provide a water perspective of lipid membranes and use membrane hydration to investigate:

- (i) The interaction of oil (hexadecane and squalene) with lipids,
- (ii) The membrane structure and membrane potential landscape,
- (iii) Divalent ion-induced membrane chemical, electrostatic and mechanical fluctuations.
- (iv) Water ordering at operating voltage-gated ion channels.

Figure 1.1 describes the major topics and the key results of this thesis.

In what follows I present the state of the art in membrane imaging research by describing the different model membrane systems and the variety of imaging methods to study them.

1.2. State of the art in membrane imaging research

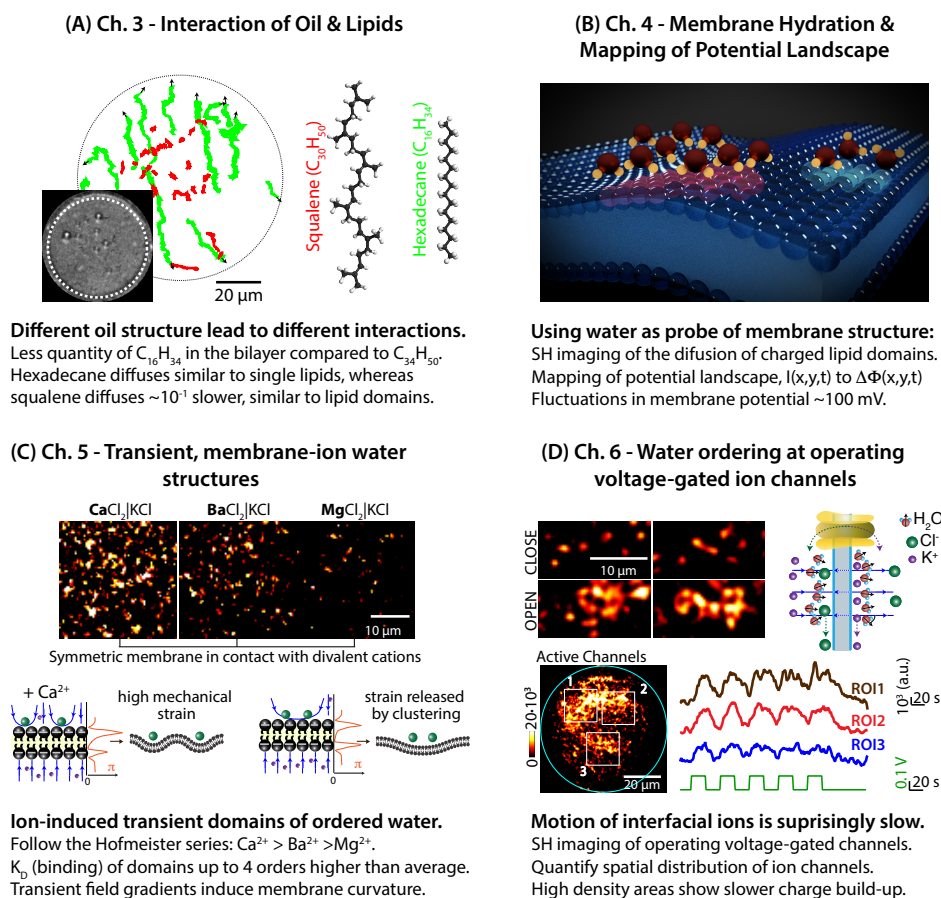


Figure 1.1 – A water window to fundamental membrane processes. Using membrane hydration to investigate (A) the interaction of oil (squalene and hexadecane) with lipids (chapter 3 of this thesis) (B) the membrane structure and membrane potential landscape (chapter 4) (C) divalent ion-induced membrane chemical, electrostatic and mechanical fluctuations (chapter 5) and (D) water ordering at operating voltage-gated ion channels (chapter 6).

I explore these methods and evaluate their advantages and disadvantages. I then introduce how label-free and non-resonant second harmonic generation (SHG) addresses the challenges of membrane imaging. In aqueous solutions, as will be shown in detail, non-resonant SHG arises from the non-resonant response of water molecules. I discuss the approach of how to image the weak non-resonant response of water at sub-second time scale in order to follow the spatiotemporal evolution of lipid membranes. Finally, I discuss the open opportunities for non-resonant SH imaging as applied to membrane research.

1.2 State of the art in membrane imaging research

What we know of the structure of lipid membranes started with the fluid mosaic model of Singer and Nicholson [20] which was proposed in 1972. This model viewed the lipid bilayer as

a 2D fluid in which embedded proteins can diffuse freely. In other words, the membrane was viewed solely as a solvent for membrane proteins. In 1997, Simons and Ikonen [21] showed a different aspect of membrane structure that is now known as the lipid raft hypothesis. According to this hypothesis, the plasma membrane is capable of lateral organization in which a liquid-ordered phase, rich in saturated phospholipids and sphingolipids are mixed with cholesterol and form domains that coexist with a liquid-disordered phase rich in unsaturated lipids. It was then proposed that certain proteins have an affinity to these domains, thus suggesting that domains serve as "rafts" for transport of membrane components or as signaling platforms. The driving force to image membranes has been to provide direct visualization of rafts and to prove their existence, both in real cell membranes and model membranes. Owing to the complexity of real cell membranes, several model membranes have been developed to mimic them. The goal has been to study membranes in a simplified manner so that fundamental understanding of their organization, dynamics, and composition can be obtained.

1.2.1 Model membranes

Figure 1.2 shows a variety of model membrane systems and their typical spatial dimensions, classified into curved and planar membranes. The spatial and temporal resolutions of the imaging system limit the type of model membranes that can be studied. For diffraction-limited microscopes, the model membrane must be at least micron-sized. Furthermore, for diffusing membranes such as giant unilamellar vesicle (GUV), the acquisition time of the imaging system must be faster than the diffusion of the GUV. As such, to obtain a proper image, an additional method is needed to slow down the GUVs or to trap them. With these limitations in mind, stationary planar membranes are generally preferred over diffusing curved membranes. Moreover, an image is a planar cross-section of the sample, thus, planar membranes provide a larger cross-section as compared to curved membranes. In what follows, a summary of the advantages and disadvantages of the different model membranes are given.

The simplest model membranes to use are **lipid monolayers** deposited on a water surface (see Fig. 1.2 top right) [22, 23]. These monolayers are formed in a Langmuir trough, a device that can tune the lateral pressure of the monolayers, and thus, can control the packing density [24]. This system allows direct access to the monolayer and the aqueous phase, thus pH and ionic strength are controllable. Owing to their simplicity, it has been used to study phase transitions, alkyl chain conformations, head group features and membrane hydration with a variety of imaging and spectroscopy techniques [25]. Several aspects of molecular level interactions involved in membrane processes, such as charge-charge interactions, hydrogen bonding, and charge-dipole interactions [13, 11, 14, 12] have been investigated in detail using this system. For example, lipid monolayers in combination with vibrational sum-frequency generation (SFG) spectroscopy have been used to study the conformation of the alkyl chains [26, 24, 27, 28, 29], the structure and hydration of the lipid head groups [30, 31] and the effect of cholesterol on the alkyl structure [32]. This system has also been used in combination with epi-fluorescence microscopy [33] and Brewster angle microscopy [34, 35] to study ion-

1.2. State of the art in membrane imaging research

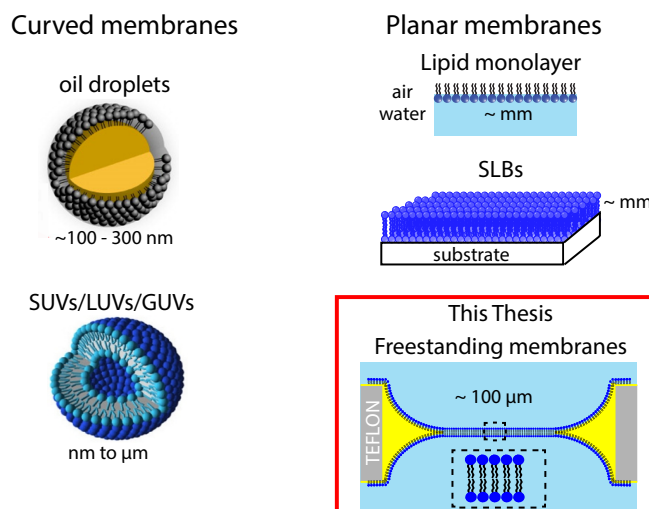


Figure 1.2 – Diverse model membrane systems. Different types of model membranes that are classified into curved or planar membranes. This thesis focuses on freestanding horizontal planar lipid membranes, highlighted in red.

membrane binding and domain formation. Though lipid monolayers are advantageous in many aspects, a number of disadvantages exist including a large sample volume (150 mL) [36], a large amount of deposited monolayer and increased oxidation rate of unsaturated lipids because of direct exposure to air. The biggest disadvantage though is that lipid monolayers are not bilayers, and they reside in an environment that is not typical of a biological membrane interface, that is, water/membrane/water.

Some of the issues in lipid monolayers are addressed by **lipid droplets**. These are nano-sized oil droplets (see Fig. 1.2, top left) coated with lipid monolayers that are dispersed in an aqueous solution [37]. The surface to volume ratio of these droplets is 2-3 orders of magnitude larger than Langmuir monolayers, at a much smaller sample volume (<1 mL). At the same time, they are immersed in water, thus preventing oxidation. Furthermore, oil droplets occur in nature, such as triglycerides and steryl esters and are coated with phospholipid monolayers that function as storage of energy [38, 39, 40]. However, the small size of these droplets makes them unsuitable to be used in microscopy.

Compared to the first two models, **supported lipid bilayers (SLBs)** (see Fig. 1.2, middle right) [41, 42] are more realistic model membranes because they contain a bilayer structure. The presence of a support makes this model membrane ideal for force microscopies and multitudes of surface-sensitive imaging techniques [12]. Several structural parameters with nanometric resolution can be extracted, such as mapping of the bilayer thickness [43] and measurement of the sizes of nanodomains [44]. The presence of a support, however, could introduce support-membrane interactions that have been shown to influence lipid distribution and thus affect the outcomes of the experiment [45].

Giant unilamellar vesicles (GUVs) (see Fig. 1.2, bottom left) are spherical lipid bilayers of

tens of microns in diameter. GUVs are the most accurate model for approximating the cell membrane, capturing both the bilayer structure and the spherical shape of cells. Most of the convincing studies on lipid raft hypothesis have been performed with GUVs [46, 9, 8, 6, 7, 4, 47]. In the past two decades, one of the drawbacks of GUVs has been the limitation to form only symmetric membranes. As the cell membrane is known to be asymmetric, several pieces of research have been conducted to form asymmetric GUVs. In 2011, the work by London et al. made it possible to form asymmetric membranes. This has opened doors for biophysicists to study the coupling between leaflets. For instance, if domain formation in the outer leaflet induces domain formation in the inner leaflet [48, 5]. Perhaps the only disadvantage of GUVs with respect to imaging is that several z-sections are needed to scan the whole membrane. Furthermore, during this sectioning, the GUV must be immobile, requiring some form of trapping mechanism.

Some of the limitations of GUVs can be addressed by **freestanding planar lipid membranes**, the model membrane used in this thesis. Freestanding lipid membranes are suspended bilayers formed by apposition of two lipid monolayers separated by a thin Teflon film [49]. The technique was pioneered by Montal and Mueller in 1972. These membranes do not require a support and the lipid composition can be easily controlled, that is, asymmetric membranes can be formed. Furthermore, the method permits electrical characterization, providing a feedback mechanism that ascertains the state of the membrane. The aqueous phase of each bilayer leaflet is readily accessible and permits modification of pH, ionic strength and incorporation of proteins. Lastly, the planar structure requires a single z-section, and when coupled with surface-selective, wide-field imaging, can lead to high throughput and temporally resolved membrane imaging method.

1.2.2 Approaches to membrane imaging: Advantages and limitations

Obtaining the spatiotemporal evolution of lipid membranes with molecular level information is a challenging task in many aspects. First, the method must be label-free and in-situ, so as not to perturb the molecular structure of the ~5 nm thick membrane bilayer. Second, the membrane is buried in bulk aqueous solution requiring a surface-selective technique that isolates the surface response from the bulk response. Third, the detectable intensity generated from probing molecular interactions at the water/membrane interface is very weak, requiring integration time of minutes [50, 51, 52]. As dynamical processes in biology occur in millisecond timescales, e.g., lipid diffusion, the temporal resolution must be improved. Lastly, in contrast to spectroscopy and electrode-based methods, the method must be imaging-based to obtain spatiotemporal fluctuations. Having considered these challenges, we proceed to describe the different membrane imaging techniques that have been used in the past decades and discuss their advantages and limitations. Figure 1.3 shows a summary of the common membrane imaging methods that are currently used and the pros and cons of each method. The list is not exhaustive.

1.2. State of the art in membrane imaging research

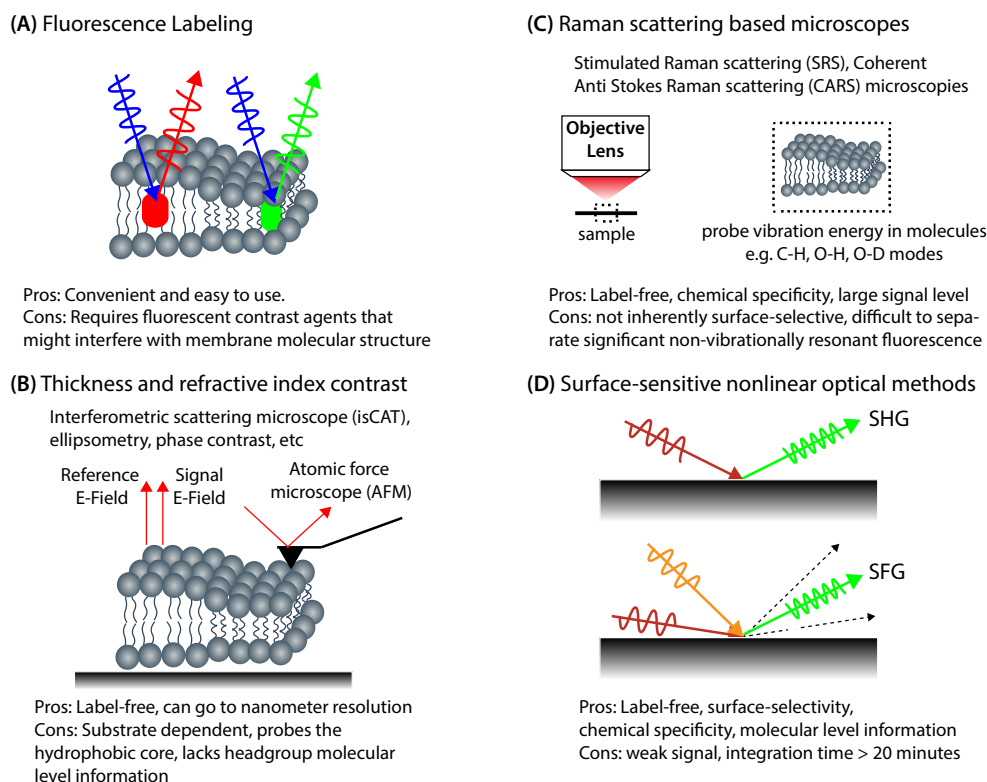


Figure 1.3 – Illustration of the different methods of imaging membranes. (A) Fluorescence labeling (B) thickness and refractive index based contrast methods (C) Raman scattering based imaging methods, (D) surface sensitive, second-order nonlinear optical methods in reflection geometry.

Fluorescence Labeling

Studies of phase separation of membrane components have been successfully visualized with fluorescent probes [21, 46, 53]. Phase diagrams of multicomponent membranes have been constructed to map the different phases of membrane constituents [7, 47]. The simplicity and ease of using fluorophores have pushed the boundaries of membrane imaging in the past decade, coupled with the developments in super-resolution imaging [54, 55], such as stimulated emission depletion microscopy (STED) [56] and photoactivated localization microscopy (PALM) [57, 58], such that nano-sized domains can now be visualized. Though highly successful, fluorescence labeling depends on the partitioning and positioning of the fluorescent labels. To this end, a study was conducted to identify the partitioning of 26 commonly used membrane probes as a function of membrane composition. For instance, the DiI dye partitions into the liquid-ordered phase when mixed with 1,2-dioleoyl-sn-glycero-3-phosphocholine (DOPC), distearoylphosphatidylcholine (DSPC), and cholesterol but partitions into the liquid-disordered phase when mixed with sphingomyelin, DOPC, and cholesterol [59, 60]. This suggests caution when conducting and interpreting experiments with fluorescent labels as they change behavior depending on the composition of the membrane. Furthermore, it also suggests that fluorescent labels interact with membrane constituents and can perturb their

Chapter 1. Introduction

molecular structure. Finally, the membrane is viewed from the perspective of labels that are not native its environment.

Thickness and refractive index contrast

In addition to labeling, label-free methods such as ellipsometry [61], interferometric scattering microscopy (isCAT) [62] and force microscopes [12] have been used to image membranes. These techniques take advantage of the varying refractive-index contrast or bilayer thickness across the membrane. In the raft hypothesis, the liquid-ordered phase imposed a higher degree of conformation on the hydrophobic core compared to the liquid-disordered phase. This results to a thicker bilayer, tighter packing, and varying refractive-index across the membrane. The above-mentioned techniques, though very informative, is focused on the hydrophobic core and cannot probe the chemistry of the lipid headgroups. Furthermore, as the difference in contrast is relative to some reference, they require some form of pre-calibration wherein a substrate or a priori knowledge of the sample is needed.

Raman scattering based microscopes

Imaging of resonant vibrational response using coherent anti-Stokes Raman scattering (CARS) [63, 64, 65, 66] or stimulated Raman scattering (SRS) microscopy [67, 68, 69] can be used to image membranes. Raman microscopy is a powerful tool for membrane imaging primarily because of its chemical specificity. For instance, the CH_2 vibrational modes of lipids can be exploited to provide membrane contrast [67, 64] and isotopic substitution of water can be used to follow hydrodynamics near plasma membranes. Recently, the group of Ji-Xin Cheng demonstrated the first label-free vibrational spectroscopic imaging of neuronal membrane potential using hyperspectral stimulated Raman scattering microscopy [70]. They showed that the magnitude of action potentials are spatially dependent to the location of stimulation. One of the drawbacks of Raman microscopy is that it is not inherently surface selective. It probes not only the membrane but also all biomolecules within the field of view. Furthermore, as the process of Raman scattering is inelastic, the sample is susceptible to photodamage. In some cases, it is also difficult to separate the Raman signal from the intrinsically significant and non-vibrationally resonant fluorescence signal.

1.2.3 State of the art in surface-sensitive nonlinear optical imaging methods

In most of the above methods, the role of hydration, electrostatic interactions and the influence of the electric double layer is difficult to probe. To address the challenges of membrane imaging, the chemical specificity of Raman microscopy is combined with surface selectivity. This can be achieved with second-order nonlinear optical methods, such as second harmonic generation (SHG) and sum-frequency generation (SFG). These methods provide molecular-level information and surface selectivity at the same time label-free. The first attempt to

visualize membrane structure and dynamics with SHG was performed by Ries et. al [52]. They showed that single component symmetric membranes do not emit SH photons with an integration time more than 20 minutes. The first demonstration of label-free SH imaging of membrane was done by the group of Conboy where they used the UV resonant response of an organic and chiral compound binding to supported membranes [50]. It took 30 minutes to record an image. They further extended their work to visualize the binding of tetracaine, a local anesthetic, to supported membranes [51]. It is worth noting that even though the process is resonant to an electronic transition, it took at least 20 minutes to acquire an image [51]. As membrane dynamics occur in much shorter time scale, no dynamic information was obtained.

So far, label-free imaging of lipid membranes at sub-second time scale has not been possible. This thesis (see Chapter 2.1) addresses this challenge by increasing the throughput of nonlinear microscopes achieving 2-3 orders improvement in temporal resolution.

In the next section, we explore the theory of SHG and discuss open opportunities in membrane imaging research.

1.3 Second harmonic generation

In this section, we describe the theory of second harmonic generation and apply it in the context of membrane imaging. Second harmonic generation (SHG) is a second-order nonlinear optical process discovered by Franken and colleagues in 1961 [71]. When an electromagnetic field \mathbf{E} interacts with a molecule, it can induce a molecular dipole \mathbf{p} in the form of [11]:

$$\mathbf{p} = \alpha^{(1)} \cdot \mathbf{E} + \frac{1}{2} \beta^{(2)} : \mathbf{E}\mathbf{E} + \frac{1}{6} \beta^{(3)} : \mathbf{E}\mathbf{E}\mathbf{E} + \dots, \quad (1.1)$$

where α is the first-order polarizability, $\beta^{(2)}$ is the second-order polarizability, and $\beta^{(3)}$ is the third-order polarizability. Each of these terms describes a charge oscillation in the molecule that can act as a source for scattering. The polarization \mathbf{P} is the sum of the induced molecular dipoles per unit volume. The second harmonic light originates from the second-order polarization $\mathbf{P}^{(2)}$ that is:

$$\mathbf{P}^{(2)} = \epsilon_0 \chi^{(2)} : \mathbf{E}\mathbf{E} \sim N \langle \mathbf{p}^{(2)} \rangle \quad (1.2)$$

where $\mathbf{p}^{(2)}$ is the second-order induced molecular dipole and $\langle \rangle$ denotes orientational averaging. The second order susceptibility $\chi^{(2)}$ describes the second-order response of the medium and depends on the second-order polarizability $\beta^{(2)}$, the density of molecules and their orientational distribution. In the electric dipole approximation [72, 73], SHG as a second-order nonlinear optical process is forbidden in a centrosymmetric medium. However, at interfaces between isotropic media, the symmetry is broken along the surface normal of the interface

and second harmonic light can be generated. As a result, SHG is a powerful surface-specific technique to characterize interfaces with molecular level details [74]. The first demonstration of surface SHG was performed by Brown & Matsuoka to probe molecular monolayers at surfaces in 1969 [75]. The Eisenthal group first demonstrated the use of SHG to probe surface chemistry of particles in liquids [76]. Since then, SHG has been used to probe various interfaces [11].

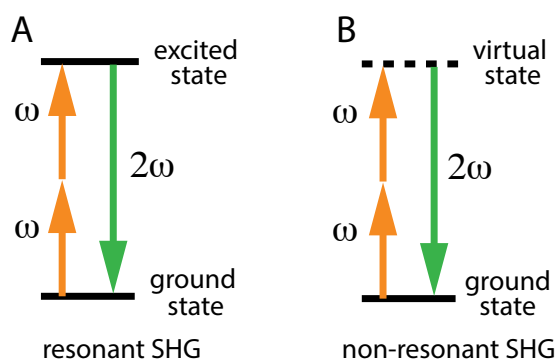


Figure 1.4 – Energy diagram for a resonant and a non-resonant second harmonic generation (SHG). For the resonant process, two incident photons ω (orange) excite the molecule to an excited electronic state, and upon relaxation to ground state, emits a photon at twice the frequency 2ω (green). For the non-resonant process, the molecule is excited to a virtual state, and upon relaxation emits a photon at twice the frequency 2ω (green).

The interaction of light with matter can be a resonant or a non-resonant process. For the resonant second harmonic generation, two incident photons, ω excite a molecule to an excited state, usually an electronic transition, after which the molecule returns to the ground state and emits a photon at twice the frequency, 2ω , see Fig. 1.4A. For the non-resonant SHG, two incident photons excite a molecule to a virtual state after which, the molecule returns to ground state and emits a photon at twice the frequency, see Fig. 1.4B. The process is elastic, i.e., there is no energy loss or absorption of photons, thus ensuring low photo-damage and photo-toxicity. For a non-resonant process, the frequencies of all interacting fields are far away from the closest electronic resonance of the material system, therefore, the response of each molecule is identical. Using the harmonic oscillator model (Boyd Chapter 1.4 [73]) under non-resonant conditions, the second-order susceptibility is:

$$\chi^{(2)} = \frac{e^3}{\epsilon_0 m^2 \omega_0^4 d^4} \quad (1.3)$$

where m and e are fundamental constants, the mass, and charge of the electron, respectively, d is the lattice constant, and ω_0 is the frequency of the illuminating field. For condensed matter, d is relatively the same. Thus, the second order response of molecules is expected to be the same for a non-resonant process, except when the molecule possess inversion symmetry, where it must necessarily vanish. This also means that only non-centrosymmetric molecules can emit SH photons, e.g, water molecules emit SH photons but not Na^+ or K^+ .

Thus in aqueous solutions where there are 55 mole/L of water molecules, the SH response is dominated by water. In the interface, the number density of interfacial water molecules greatly outnumbers the density of surface moieties [77, 78, 79, 80]. Thus, non-resonant SHG in aqueous solution probes the orientational ordering of water along the surface normal.

SHG can also generate coherent or incoherent response depending on the phase relationships of the non-centrosymmetric molecules. For bulk electrolyte solutions, the SH response originate mainly from water molecules [81]. Second harmonic scattering (SHS) that originates from isotropically distributed non-centrosymmetric molecules is known as Hyper-Rayleigh Scattering (HRS). This type of scattering arises from molecules that are not spatially correlated, hence incoherent phase relationship, and the SH intensity scales linearly with number density. In contrast, when the non-centrosymmetric molecules have fixed phase relationship, e.g. being in the same interface, or the presence of molecular correlations such as h-bonding, then the emitted SH intensity is coherent and scales quadratically with the number density.

Second harmonic generation applied to membrane imaging. For SHG at planar interfaces, the second-order polarization is:

$$\mathbf{P}^{(2)}(2\omega) = \epsilon_0 \chi_s^{(2)} : \mathbf{E}(\omega) \mathbf{E}(\omega) \quad (1.4)$$

where $\chi_s^{(2)}$ is the surface second-order susceptibility that depends on the density, the second-order polarizability $\beta^{(2)}$ and orientational distribution of non-centrosymmetric molecules at the interface. For label-free, non-resonant SHG at aqueous interfaces, the SH response is dominated by water molecules.

The ordering of water molecules can also be affected by chemical interactions that are strong enough to distort the orientation of water molecules, for example, the presence of surface charges at interfaces. We define the interface at $z = 0$, and the electric field emitted at the interface, $\mathbf{E}(\omega = 0, z) = \mathbf{E}_{DC} = -\nabla\Phi(z)$. The total nonlinear polarization $\mathbf{P}^{(NL)}$ that emits radiation at twice the frequency is:

$$\mathbf{P}^{(NL)}(2\omega) = \mathbf{P}^{(2)}(2\omega) + \mathbf{P}^{(3)}(2\omega) \quad (1.5)$$

$$\mathbf{P}^{(3)}(2\omega, z) = \epsilon_0 \chi^{(3)'} : \mathbf{E}(\omega) \mathbf{E}(\omega) \mathbf{E}_{DC}(z) \quad (1.6)$$

where $\chi^{(3)'}$ is the effective third-order susceptibility, that includes all contributions that emit photons at twice the frequency and that require interaction with \mathbf{E}_{DC} . These are: (1) \mathbf{E}_{DC} oriented water molecules at the interface, (2) \mathbf{E}_{DC} oriented water molecules in the bulk solution, both of these contributions depend on the second-order polarizability, $\beta^{(2)}$ of water, and (3) \mathbf{E}_{DC} interaction with the isotropic third-order susceptibility of bulk water, $\chi_b^{(3)}$ (which depends on the third-order polarizability, $\beta^{(3)}$). These contributions are illustrated in Fig. 1.5.

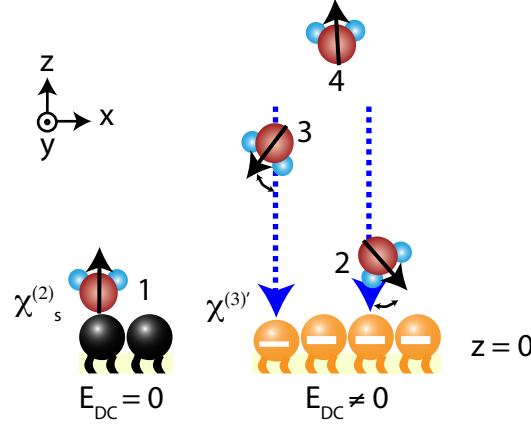


Figure 1.5 – Molecular sources for possible second harmonic scattering: (1) The breaking of centrosymmetry by an interface through the $\chi_s^{(2)}$ coupled contribution and electrostatic field, (E_{DC}) coupled contribution that (2) reorients molecules at the surface, (3) in the bulk and (4) the third-order response of isotropic molecules ($\chi_b^{(3)}$).

Assuming isotropy along the x and y, the total third order polarization is thus:

$$P^{(3)}(2\omega) = \epsilon_0 \chi^{(3)'} E(\omega) E(\omega) \int_0^\infty E_{DC}(z) dz \quad (1.7)$$

$$P^{(3)}(2\omega) = \epsilon_0 \chi^{(3)'} E(\omega) E(\omega) \Phi_0 \quad (1.8)$$

where Φ_0 represents the surface potential. From eq. 1.5, the SH emitted intensity is

$$I(2\omega) \propto |P^{(2)}(2\omega) + P^{(3)}(2\omega)|^2 \quad (1.9)$$

$$I(2\omega) \propto I(\omega)^2 \left| \chi_s^{(2)} + \chi^{(3)'} f_3 \Phi_0 \right|^2 \quad (1.10)$$

where f_3 is an interference term that depends on the geometry of the experiment, for details see [78]. For transmission experiments, $f_3 \rightarrow 1$. Equation 1.10 shows that the SH intensity is proportional to surface potential.

Finally in the context of a lipid bilayer, there are two oppositely oriented membrane interfaces i , that each have a surface potential $\Phi_{0,i}$ and surface susceptibility $\chi_{si}^{(2)}$, resulting to

$$I(2\omega) \propto I(\omega)^2 \left| \chi_{s1}^{(2)} - \chi_{s2}^{(2)} + \chi^{(3)'} f_3 (\Phi_{0,1} - \Phi_{0,2}) \right|^2 \quad (1.11)$$

Equation 1.11 has significant implications to membrane asymmetry, indicating that asymmetry in surface potential could be detected with SHG.

1.4 Open opportunities in membrane imaging research

Label-free and non-resonant SH imaging of membranes is challenging because of the weak non-resonant response of dipolar molecules (e.g. water molecules). We address this by improving the throughput of second harmonic imaging. The challenge is two-fold, namely the development of an optical tool with improved throughput to image the weak non-resonant response of water with the required spatial and temporal resolution and the application of the method to realistic freestanding lipid membranes.

1.4.1 Improving the throughput of SH microscopes

The introduction of two-photon laser scanning fluorescence (2PF) microscopy by Watt and Webb in 1990 [82] led to developments of laser sources that are optimized for fluorescence microscopy. In the year 2000, the development of pulse, near-infrared (near-IR) and high repetition rate titanium sapphire lasers [83] improved the throughput of 2PF microscopy. The high repetition rate (80 MHz) lasers enhanced the generation of two-photon pulses. The time between laser pulses was optimized to the relaxation time of the fluorophores from the excited state to ground state. As soon as the fluorophores reach the ground state, they are immediately induced to an excited state. Historically, most SHG microscopes have been adapted to confocal two-photon microscopes using the same laser source [84, 85, 86]. However, it is important to understand that the generation of photons for SHG is fundamentally different from two-photon fluorescence, and thus using the same light source as two-photon microscopes would not yield the same efficiency for SH microscopes. Dadap et. al provided the guidelines on how to optimize the generation of SH photons as a function of laser parameters [87]. As the generation of SH photons is instantaneous, to optimize the detection of photons, the repetition rate must be as high as possible while delivering as much energy per pulse. However, with high energy pulses and very high repetition rate, the molecules have no time to relax and can lead to phototoxicity. Thus, a balance between imaging efficiency and damage mechanism must be optimized (see Chapter 2.1 for details). Furthermore, as the physics of generating photons for SHG is the same regardless of excitation area, temporal resolution can be improved by shifting to wide-field illumination as opposed to confocal illumination, thus, avoiding the need to scan and allowing for single-shot imaging.

1.4.2 Membrane asymmetry

Water is a ubiquitous solvent in contact with various interfaces. As the non-resonant SH imaging of aqueous interface is dominated by water molecules, the method is applicable not only to membrane imaging but to any aqueous interfaces in general [11, 88]. For membrane imaging, where there are two interfaces that are oppositely oriented, non-resonant SH imaging of membranes is particularly suitable to studies of membrane asymmetry that is known to affect various bilayer properties, including membrane potential, surface charge, permeability, shape, as well as stability [89]. The loss of asymmetry in cells has various functional signif-

Chapter 1. Introduction

icance, most notable of which, is related to cell death by apoptosis [90]. As the intra- and extracellular distribution of lipids, proteins, and ions are asymmetric and cell-type dependent, the proposed imaging method could prove instrumental to study membrane structure (see Chapter 4).

1.4.3 Ion-specific effects

The ability of ions to salt-out (aggregate) proteins was extensively studied in a series of papers between 1887 to 1898 by Franz Hofmeister and colleagues [91, 92, 93]. On the basis of these studies, the ability of ions to salt-out proteins was linked to their "water withdrawing effect" [94]. Figure 1.6 shows a typical Hofmeister series. Since its conceptualization, this series has been invoked in a variety of effects including the folding of proteins [95, 96], the formation of secondary structures, [97, 98] self-assembly and enzyme activities [93].

Molecular level studies of ion-specific effects on air/biomolecule/water interface have been carried out in great detail using vibrational sum frequency scattering and molecular dynamics simulation [99, 100, 101, 102]. The origin of ionic specificity has been intimately linked to ion hydration and the ability of water to form hydrogen bonds. Ions that are weakly hydrated and ions with low charge density are driven to hydrophobic surfaces leading to salting-out effects.

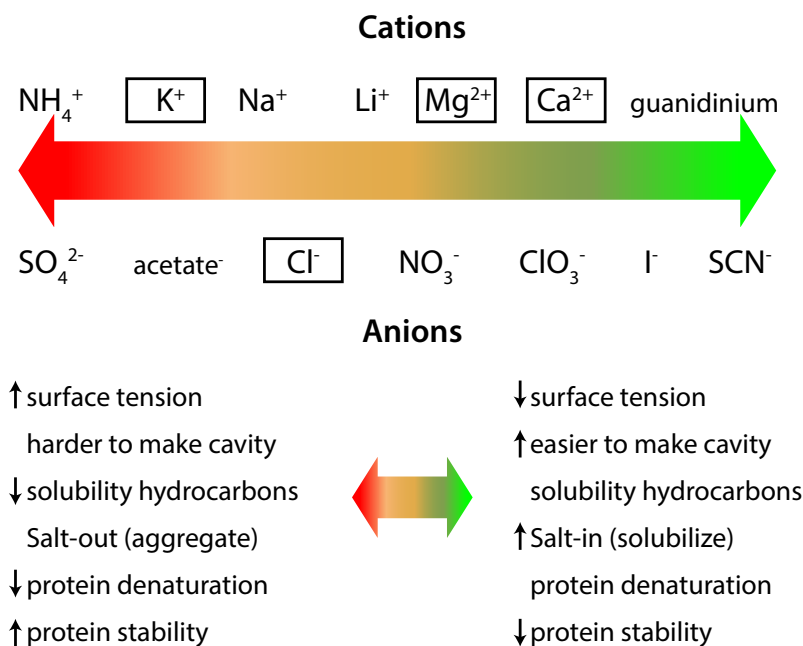


Figure 1.6 – Typical ordering of cations and anions in a Hofmeister series adapted from Ref. [94]. The rectangles indicate the ions studied in this thesis.

In biological membranes, ion-specific effects are important for chemical signaling and signal transduction. For example, divalent cations like calcium serve specific roles in governing neurotransmitter release at the pre-synapse [103], bind to negatively charge interfaces and

1.4. Open opportunities in membrane imaging research

drive a host of events such as fission and fusion of vesicles [104, 105, 106]. Furthermore, ion pumps and ion channels that transport ions across the membrane of cells are ion-specific. For example, K^+ ion channel is permeable to potassium ions but not to sodium ions.

Our current understanding of ion-specific effects in cells is linked to specific-binding sites. In the case of Mg^{2+} and Ca^{2+} , they bind to negatively charged lipid head groups with different binding constants determined by the molecular factors involved in the interaction [13, 101, 107, 99, 108]. Though it is known how ions bind to membranes from spectroscopic binding studies of lipid monolayers [109, 110, 111] and supported by molecular dynamics simulation, it is not clear how ionic specificity in cells lead to diverse cellular functions. We explore this question in Chapter 5, where we link molecular structure to the spatiotemporal fluctuations of membranes by second harmonic imaging of the hydration of freestanding lipid bilayer membranes in contact with electrolyte solutions containing divalent ions. We show that the binding of divalent ions induces ordered domains of water with electric field gradients that are sufficient to induce membrane curvature. This link between molecular structure and microscopic response highlights the multi-scale response of membranes to external stimuli.

1.4.4 Ion channels

Transport of ions across membranes is crucial to the survival of cells and to the whole organism itself. In order to transport ions across the membrane, the cell uses active and passive transport. Ion channels are examples of passive transport that are highly ion selective. Ion channels are responsible for numerous physiological functions, including chemical signaling (e.g. Ca^{2+} as secondary messenger), and transport of ions in and out of the cells to generate membrane potential gradient that forms the basis of neuronal signaling [112, 113, 114], to regulate ionic concentration and pH and to regulate cell volume. The malfunctioning of ion-channels is related to a number of diseases including neuronal disorders such as epilepsy, ataxia [115] and hypertension [116], and secretion related disorders such as cystic fibrosis and hypoglycemia [117]. Table 1.1 lists the most common diseases that are related to ion channels. A number of reviews are available that summarize the defective channels as well as the gene mutations responsible for each disease (see Refs [112, 113, 114, 118]). Although ion channels are mostly known to generate membrane potential gradient for neuronal signaling, table 1.1 shows that the functioning of ion channels extends to many systems of the human body, including endocrine, muscular, skeletal and excretory systems. Understanding the operation of voltage-gated ion channels on a molecular level, without modifying the molecular environment of the membrane, is a formidable challenge that needs to be solved if we are to develop better drugs and treatment to cure ion-channel related diseases.

Although ion channels have been studied in detail (see the introduction of Chapter 6 for details), experimental molecular level information, that includes following the structure of water of operating ion channels has not been acquired so far. Recently, Macias et. al [88] showed that the dynamic movement of confined and electrically stimulated water inside a <1

Chapter 1. Introduction

Table 1.1 – List of commonly known ion channel related diseases based on Ref [113, 118].

Channel Type	Category	Disease	Reference
Potassium channels	Neurological disorder	Episodic ataxia with myokymia	Brown et al. (1994) [115]
	Endocrine disorder	Persistent hyperinsulinemic hypoglycemia of infancy	Inagaki et al. (1995) [119]
Sodium channels	Renal disorder	Liddle syndrome (dominant hypertension)	Chang et al. (1996) [116]
	Cardiac Arrhythmias	Long-QT syndrome,	Wang et al. (1995) [120]
Calcium channels	Disturbances of skeletal muscle excitability	Malignant hyperthermia, central core disease	Quane et al (1993)[121] Zhang et al. (1993)[122]
Chloride channels	Bone diseases	osteopetrosis	Kornak et al. (2001) [123]

micron wide glass pore, can be SH imaged at sub-second time scale. They showed that water aligned with the externally applied field generated a strong SH response, while in the absence of the field no SH response was measured. It can be expected that using the same approach, the operation of ion channels can be imaged at sub-second timescales.

Ion selectivity and voltage gating

The ion selectivity of ion channels has been linked to specific binding sites within the channel. It is proposed that binding sites must compensate for the energetic cost of ion dehydration and that selectivity occurs when the energy balance is more favorable for some types of ions [124]. For example in the case of K^+ and Na^+ ion channels, the number of oxygen binding sites within the channel for K^+ ion channel is larger (eight oxygen atoms) compared to Na^+ ion channel (five or six oxygen atoms) and are significant enough to allow for selectivity.

Passive ion channels are usually activated by the presence of transmembrane potential that induces changes in the conformation of channel proteins to form channels. These channels are called voltage-gated ion channels. A widely used model for voltage-gated ion channel is alamethicin [125, 126, 127, 128]. Alamethicin was discovered by Meyer and Reusser in 1967 [126] from the fungus *trichoderma viride*. It is a 20 amino-acid peptide that can form voltage-gated ion channel. The length of the channel is 30 Angstrom and the channel diameter is 20 Angstrom [129, 130, 131]. The most accepted model for the gating mechanism of alamethicin is known as the "barrel-stave" model. According to this model, alamethicin channels are formed by parallel bundles of 3 to 12 individual alamethicin monomers where the hydrophilic part of the peptides align to form a water-filled channel [125, 128, 132]. Alamethicin is highly surface active [133, 134] and has a dipole moment of 67 D in octanol [135, 136]. It is believed that after adsorption to the membrane, application of a bias pushes the positive end of alamethicin into the bilayer. Although the mechanism of gating and insertion into the membrane is still debatable, it is accepted that alamethicin forms voltage-gated channels as supported by several single-channel electrical measurements [128, 137]. It was shown that conductance states always appear and disappear in the lowest conductance state. It was concluded that

these conductance states are related to channel formation.

1.5 This Thesis

In this thesis, we use high throughput wide-field second harmonic (SH) microscopy to image water-membrane interactions in freestanding lipid membranes at sub-second time scale. We apply the imaging method to study the spatiotemporal fluctuations in membrane structure, membrane potential landscape, membrane hydration free energy landscape, ion-induced and ion-specific effects, oil-lipid interactions and the operation of voltage-gated ion channels. The thesis is structured as follows:

- Chapter 2 contains the description and characterization of the SH microscope. It also contains the theoretical and experimental basis that leads to the improvement of imaging throughput. This is followed by a description of the formation and characterization of freestanding lipid membranes.
- In Chapter 3, we use SH imaging and white-light imaging to investigate the interaction of oil with freestanding lipid membranes. We show that even with equally high capacitance membranes formed from squalene and hexadecane, different interactions can be observed.
- In Chapter 4, we show in a series of experiments with freestanding lipid membranes that water, aligned by charge-dipole and hydrogen bonding interactions with the lipid head groups can be SH imaged on sub-second time scales. We use the orientation of water as a contrast mechanism to image membrane structure and map fluctuations in membrane potential landscape.
- In Chapter 5, we show that Ca^{2+} , Mg^{2+} , and Ba^{2+} interacting with negatively charged lipids induce short-lived micron-sized domains of ordered interfacial water. The hydration free energy of these domains are ion-specific and can deviate up to 4 orders of magnitude from average binding constants. Lastly, the transient structural domains exhibit free energy fluctuations that are sufficient to induce membrane curvature.
- In Chapter 6, we show that the opening and closing of ion channels lead to changes in SH intensity, which we attribute to the orientational distribution of water molecules induced by electric field gradients. We show that ion transport along the membrane is > 1 second and is likely too slow to be directly involved in the propagation of action potentials that occur on a sub-millisecond time scale.
- Chapter 7 contains the summary of the findings of this thesis followed by future applications using non-resonant SH imaging of freestanding lipid membranes.

This thesis is based on various publications by the author. The details of the publications are given at the end of the thesis.

2 Experimental Details & Methodology

This chapter describes the experimental details and methodologies employed throughout the thesis. The first section describes the characterization and improvement of imaging throughput of the second harmonic (SH) microscope. In the second section, we explain the sample preparation for freestanding horizontal planar lipid bilayers and the last section details the electrical and optical methods to characterize them.

For this chapter, the author derived the calculations for the SH throughput and performed the characterization of the SH microscope. Experimental validation of the throughput of the SH microscope (imaging of BaTiO₃ for different imaging systems) was done by Dr. Carlos Macias Romero, then working as postdoc in the Laboratory for Fundamental Biophotonics (LBP).

2.1 SH Microscope: Characterization and Throughput

For this section, I provide detailed descriptions of the second harmonic (SH) microscope. I start with the characterization of the fundamental beam followed by discussions of the point spread function (PSF), the pulse duration and the polarization sensitivity of the SH microscope. Lastly, I present the theoretical and experimental basis for the improvement of imaging throughput.

2.1.1 Optical Setup

Figure 2.1 shows the schematic of the optical setup. The light source is a Yb:KGW femtosecond laser (Light Conversion Ltd.) delivering 190-fs pulses centered at 1028 nm with a 200-kHz repetition rate. The light was passed through a band-pass filter (1,030 nm, Ekspla), and was split equally into two counter-propagating beams that were each incident at 45° with respect to the membrane. Each beam was polarization controlled using a linear polarizer (Glan-Taylor polarizer, GT10-B; Thorlabs) and a zero-order $\lambda/2$ wave plate (WPH05M-1030; Thorlabs), and was focused loosely on the sample with an $f = 20$ cm doublet lens (B coating; Thorlabs), producing a ~ 140 - μm -diameter beam waist. The average power at the sample was set between 100 mW to 240 mW for each arm. The SH photons were imaged by a 50 \times objective lens (Plan Apo NIR HR Infinity-Corrected Objective, 0.65 NA; Mitutoyo) or a 20 \times objective lens (Plan Apo Infinity-Corrected Long WD Objective, 0.42 NA; Mitutoyo) in combination with a tube lens (MT-L; Mitutoyo), a 900-nm short-pass filter (FES0900; Thorlabs), a 515-nm band-pass filter (FL514.5-10), and an intensifier-amplified CCD camera (PiMAX 4; Princeton Instruments). A 400-mm meniscus lens was placed behind the objective lens to remove spherical aberrations induced by the coverslip. In some cases, the change in NA from 0.65 to 0.42 was designed to increase the depth of focus from 0.6 μm to 1.6 μm , ensuring that the membrane stays in focus during the application of an external bias. In both cases, only the phase-matched SH photons are collected by the objectives.

Fluorescence measurements were performed with the same imaging setup as Fig. 2.1. We used either TopFluor Cholesterol or NBD PC (Avanti Polar Lipids, see Fig. 2.8) as two-photon label with emission/excitation peaks at 507/495 nm and 531/464 nm respectively. A 525 ± 25 nm (ET525/50m-2p Chroma) band-pass filter was placed before the detector to detect the outgoing two-photon fluorescence.

2.1.2 Characterization of the Fundamental Beam

We characterized the spectral profile of the fundamental beam using a USB spectrometer (USB4000, Ocean optics, spectral resolution of 0.2 nm, spectral range of 345-1037 nm). Figure 2.2A shows the spectrum of the fundamental beam after passing through a BBO crystal. Black dots are data points and blue lines are fitted Gaussian curves. The spectrum shows a single peak centered at 515.2 nm. The inset shows the spectrum of the fundamental beam centered at 1032.6 nm with full width at half maximum (FWHM) of 9.8 nm corresponding to 2.8×10^{12} Hz in frequency space. The temporal pulse profile of the fundamental beam was measured with an autocorrelator corresponding to pulse duration (FWHM) of 268 fs. The actual pulse duration assuming a Gaussian pulse is 190 fs ($268/\sqrt{2}$). The time-bandwidth product of the fundamental beam is 0.52 (2.8×10^{12} Hz \times 190 fs). The theoretical minimum time-bandwidth of bandwidth-limited Gaussian-shaped pulses is ~ 0.44 . The fundamental beam is thus of good quality.

2.1. SH Microscope: Characterization and Throughput

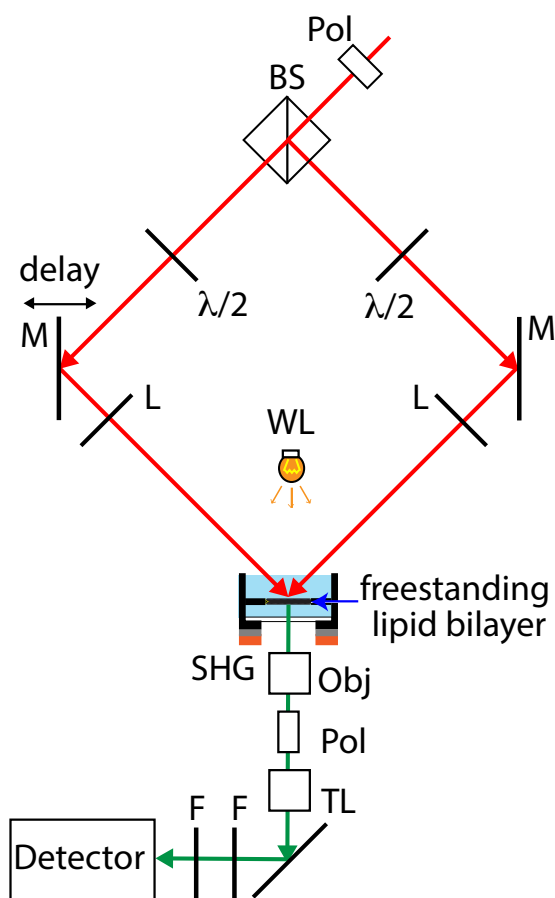


Figure 2.1 – Schematic of the optical setup. Two near-IR 190-fs 200-kHz pulsed laser beams are incident on the lipid membranes. SH photons are detected in the phase-matched direction. The beams are polarized in the plane of incidence (P). The sample chamber is not to scale. BS, beam splitter; F, filter; L, lens; M, mirror; Obj, objective lens; Pol, linear polarizer; TL, tube lens; WL, white-light source; $\lambda/2$, half-wave plate.

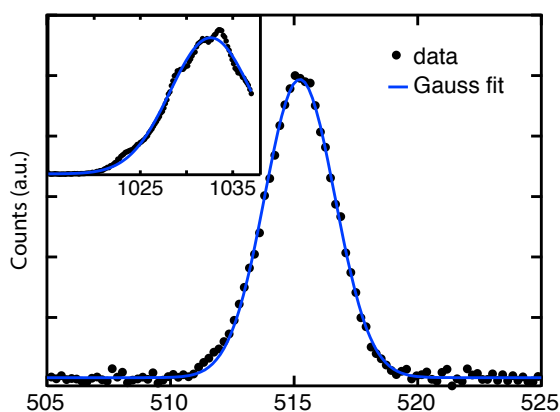


Figure 2.2 – Characterization of the fundamental beam. The spectrum of the fundamental beam after passing through a BBO crystal. The inset shows the spectrum of the fundamental beam.

2.1.3 Characterization of SH Microscope

Point Spread Function (PSF). The response of an imaging system to a point emitter is described by the point spread function. The full width at half maximum of the point spread function describes the spatial resolution of the imaging system. Figure 2.3A shows the response of the SH microscope to a 50 nm BaTiO₃ nanoparticle. The full width at half maximum was measured to be 0.89 μm . The pixel size was measured to be 0.43 μm , the system is at the Nyquist limit.

Spectrum of Pure H₂O. To confirm that the generated SH photons were at twice the frequency of the fundamental beam, the spectrum of pure water was measured by replacing the camera in Figure 2.1 with a spectrometer. Figure 2.3B shows the normalized spectrum of pure water where the maximum wavelength peaked at 515.96 nm which was indeed half of the fundamental beam, 1032.6 nm as shown in Figure 2.2.

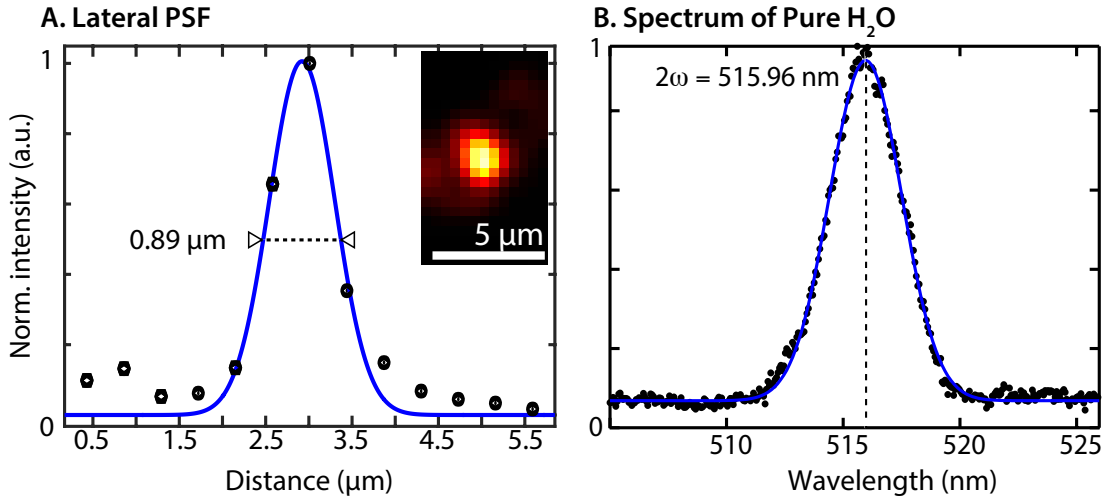


Figure 2.3 – Point Spread Function (PSF) of the SH microscope and spectrum of pure water. (A) Lateral point spread function (PSF) of the SH microscope was obtained by imaging a 50 nm BaTiO₃ nanoparticle. The inset shows the smoothed (Gaussian blur, $\sigma=1$) image of the nanoparticle and the full width at half maximum was 0.89 μm . (B) Normalized SH spectrum of pure H₂O measured using the SH microscope in 2.1 by replacing the camera with a spectrometer.

Pulse duration of the SH microscope. We measured the pulse duration of the fundamental beam at the focus of the SH microscope by recording the cross-correlation SH intensity of a 50 nm BaTiO₃ nanoparticle as a function of temporal delay. The cross-correlation signal $I(\tau)$ between two functions $P(t)$ and $G(t)$ is given by,

$$I(\tau) = \int_{-\infty}^{\infty} P(t)G(t-\tau)dt \quad (2.1)$$

where τ is called the temporal delay. If the signals $P(t)$ and $G(t)$ are obtained from an n-order process e.g., multiphoton process, we get the n-order cross-correlation. For a second harmonic generating particle, e.g. BaTiO₃ nanoparticle, we have the second order cross-correlation signal, $I_A(\tau)$. Assuming a Gaussian pulse, the full width at half maximum (FWHM) of the second-order cross-correlation signal is

2.1. SH Microscope: Characterization and Throughput

related to the FWHM of the fundamental pulse through [138, 139],

$$\tau_A^{FWHM} = \sqrt{2}\tau_p^{FWHM} \quad (2.2)$$

The schematic of the beam path of the SH microscope is shown in Fig. 2.1. After the beam splitter, the fundamental beam was split into two beams that were then reflected by two mirrors M and focused on the sample by two lenses L. We introduced a temporal delay by moving one mirror a distance x as indicated by the arrow in Fig. 2.1. The temporal delay is related to the spatial path length difference, $\delta = \sqrt{2}x$, by $\tau_{delay} = \delta/c$, where c is the speed of light in air. The lenses ensure that the beams were spatially overlapped when one mirror M is moved by a distance x . SH images of 50 nm BaTiO₃ nanoparticles dried on a glass slide were collected as the mirror was scanned resulting to SH intensity as a function of delay. Figure 2.4 shows the normalized cross-correlation intensity as a function of temporal delay (fs). The FWHM based on the Gaussian fit was 278 fs. The pulse duration of the fundamental beam at the focus is thus 197 fs. Considering that the pulse duration before the microscope is ~ 190 fs, there is little change in pulse duration at the focus.

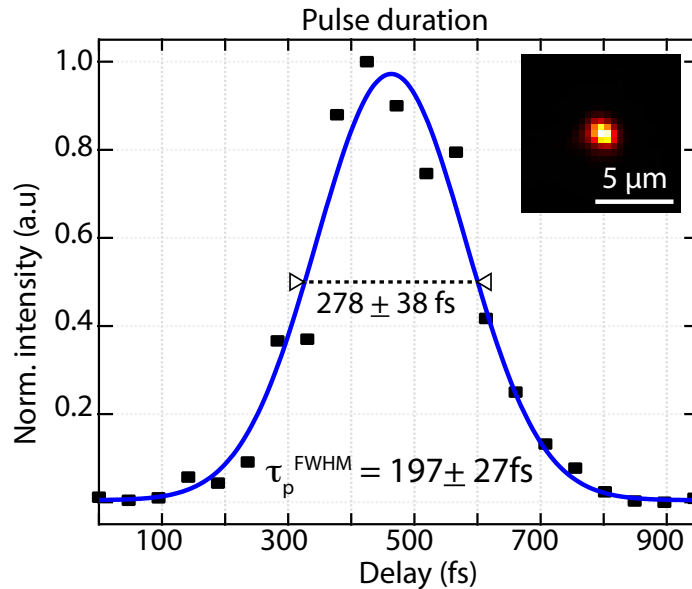


Figure 2.4 – Pulse duration at the focus of the SH microscope. The pulse duration at the focus of the SH microscope was measured using a 50 nm BaTiO₃ nanoparticle. The curve displays the normalized cross-correlation SH intensity as a function of temporal delay. The temporal delay was introduced by moving the mirror as shown in Fig. 2.1. Squares are data points while solid line is a Gaussian fit. The inset shows the image of a single 50 nm BaTiO₃ nanoparticle.

2.1.4 Polarization Sensitivity of the SH microscope

To characterize the polarization sensitivity of the SH microscope, we imaged the two-photon fluorescence (2PF) of a symmetric lipid bilayer composed of 1,2-diphytanoyl-sn-glycero-3-phosphocholine (DPhPC) mixed with 1% NBD-PC fluorophores. The emission of two-photon fluorescence is isotropic hence for the two beam configuration of Figure 2.1, we expect to have the strongest 2PF signal for SSS polarization followed by PPP, PSS, and SPP, where the first index refers to the outgoing (2PF) beam and

the last two refer to the incoming beams. S refers to out-of-plane polarization and P refers to in-plane polarization and the plane of the microscope is defined by the two incoming beams. SSS polarization is strongest because the incoming and outgoing polarizations are aligned. Figure 2.5A shows the 2PF images of a membrane bilayer at different polarization combinations. The strongest 2PF signal is SSS followed by PPP, PSS, and SPP. Figure 2.5B shows the mean intensity of a region of interest defined by the white square in Fig. 2.5A. The error bars report on the standard deviation from 20 images. The inset shows the schematic of the SH microscope showing the P and S polarization and the direction of the k-vectors. Note that PPP is almost half of SSS. This is expected as the incoming P-polarized light is oscillating at 45° with respect to the outgoing polarization and thus only half of the intensity is detected. The PPP intensity is not exactly half of the SSS intensity because the optical elements (mirrors, lenses, and polarizers) do not have exactly the same sensitivity to P and S polarizations. Figure 2.5 shows that the SH microscope is indeed sensitive to changes in polarization.

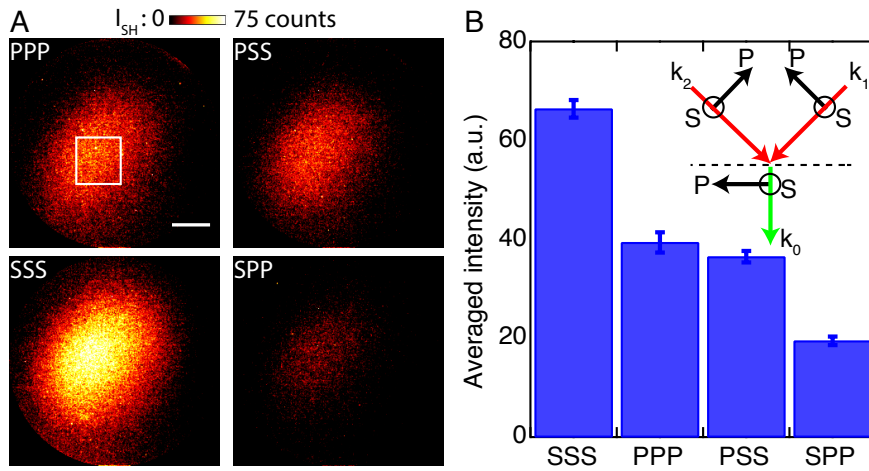


Figure 2.5 – Polarization sensitivity of the SH microscope. (A) Two-photon images of a lipid bilayer composed of DPhPC + 1 % NBD-PC recorded at different polarization combinations. The first letter denotes the outgoing polarization whereas the last two letters denote the incoming polarization. Scale bar is 20 μm . (B) Average intensity for the region of interest defined by the white square in (A). The error bars report on the standard deviation from 20 images. The inset describes the polarization directions (solid black lines) of the SH microscope, see Figure 2.1, and the black dash line indicates the location of the bilayer. Abbreviations: P - in-plane polarization, S - out of plane polarization, $k_{0,1,2}$ are k-vectors of the outgoing (k_0) and incoming ($k_{1,2}$) beams. The plane of the microscope is defined by the incoming beams k_1 and k_2 , here, the plane of the paper.

2.1.5 Improving the Imaging Throughput of Nonlinear Microscopes

In this section, I describe the improvement in imaging throughput of the SH microscope and compare it to conventional confocal microscopes. For second harmonic generation, the number of photons N_i per second per illuminated area is given by [87, 140]:

$$N_i \propto |\Gamma^{(2)}|^2 \frac{E_{p,i}^2}{\tau_i A_i} f_i \quad (2.3)$$

where $\Gamma^{(2)}$ is the effective second-order susceptibility of the probed (curved) surface, $\Gamma^{(2)}$ transforms to

2.1. SH Microscope: Characterization and Throughput

$\chi^{(2)}$ for planar interfaces, $E_{p,i}^2$ is the energy per pulse, τ_i is the pulse duration, A_i is the illumination area and f_i is the repetition rate. The subscript i refers to two different configurations that will be compared here: wide-field (wf) vs scanning (s). We define throughput as the number of detected photons per second per image. For scanning systems, the illumination area is small compared to the size of the image, thus, it takes longer time to acquire an image thereby decreasing the throughput. In contrast for wide-field systems, the illumination area can be enlarged to matched the desired image size. To quantify the increase in throughput, we assume for a scanning system, a scanning rate of one image frame per second. The scanning system requires n scanning points, with $n = A_{wf}/A_s$, assuming each pixel corresponds to one scanning point. Note that one image frame per second is relatively fast for a scanning system. Assuming the same fluence ($F = \frac{E_p}{A}$, i.e., $E_{wf} = n \cdot E_s$), pulse duration ($\tau_{wf} = \tau_s$) and wavelength for wide-field and scanning systems, we can compare the throughput ratio N_{wf}/N_s as:

$$\frac{N_{wf}}{N_s} = n \frac{f_{wf}}{f_s} \quad (2.4)$$

Equation 2.4 shows that for an image with 100 x 100 (or 1000 x 1000) scanning points ($n = 10^4$ or 10^6) and a scanning repetition rate of $f_s = 100$ MHz, a wide-field system detects more photons if $f_{wf} > 10$ (or 0.1) kHz. For a wide-field system with a repetition rate of 100 kHz, this translates to 10 to 1000-fold improvement in imaging throughput. We compare three cases: (i) a scanning system ($f = 80$ MHz, $\tau = 190$ fs, illumination diameter = $0.5 \mu\text{m}$, $\lambda = 800$ nm) similar to [141, 84], (ii) a wide-field double beam configuration ($f = 1$ kHz, $\tau = 120$ fs, illumination diameter = $250 \mu\text{m}$, $\lambda = 800$ nm) similar to [142] and (iii) a wide-field double beam configuration similar to currently used SH microscope ($f = 200$ kHz, $\tau = 190$ fs, illumination diameter = $100 \mu\text{m}$, $\lambda = 1030$ nm). Figure 2.6A shows the calculated imaging throughput for the three different systems described. The relative imaging throughput of the wide-field (blue line) 200 kHz system is larger than the other two. Owing to the improvement in throughput, lower fluences, and lower peak intensity can be used. Figure 2.6B shows the calculated fluences as a function of laser power for the three cases described. The colored area reports on the damage thresholds based on reference [143], when illuminating with 1035 nm wavelength, 393 fs pulses, 100 kHz repetition rate, and $10 \times 50 \mu\text{s}$ dwell time. For comparison, the delivered peak intensities are shown in Fig. 2.6C. Low fluence with high imaging throughput is ideal for non-invasive and long-time imaging suitable for real-time biological imaging.

Note that the physics of generating second harmonic photons is the same for scanning and wide-field systems. The condition of the same fluence requires much more energy per pulse for the wide-field system compared to the scanning system. Equation 2.3 shows that imaging efficiency can be improved by delivering as much energy per pulse at high repetition rates. However, energy transport mechanisms limit the repetition rate because the energy must be dissipated before the next pulse arrives. By choosing a medium repetition rate and wide-field illumination as used in this thesis, Macias et. al, indeed showed that wide-field medium repetition rate reduces the photodamage of living cells [144].

Imaging Throughput Measurements. To compare the throughput for three cases in Fig. 2.6, we imaged the SH response of 50 nm BaTiO₃ nanoparticles deposited on a coverslip with the illumination parameters described in Fig. 2.6. We measured the same spot on the sample with similar wavelength and pulse durations. The following are the conditions used: (i) scanning system, fluence = $2.55 \text{ mJ}/\text{cm}^2$, 88 MHz, (ii) wide-field 1 kHz system, fluence = $10.5 \text{ mJ}/\text{cm}^2$, 1 kHz, (iii) wide-field 200 kHz system, fluence = $2.55 \text{ mJ}/\text{cm}^2$, 200 kHz. The contrast, defined as the amplitude of the signal divided by its spanning range was calculated for each system and plotted as a function of acquisition time. Figure 2.7A shows the measured contrast for each of the systems described. The black data points were taken

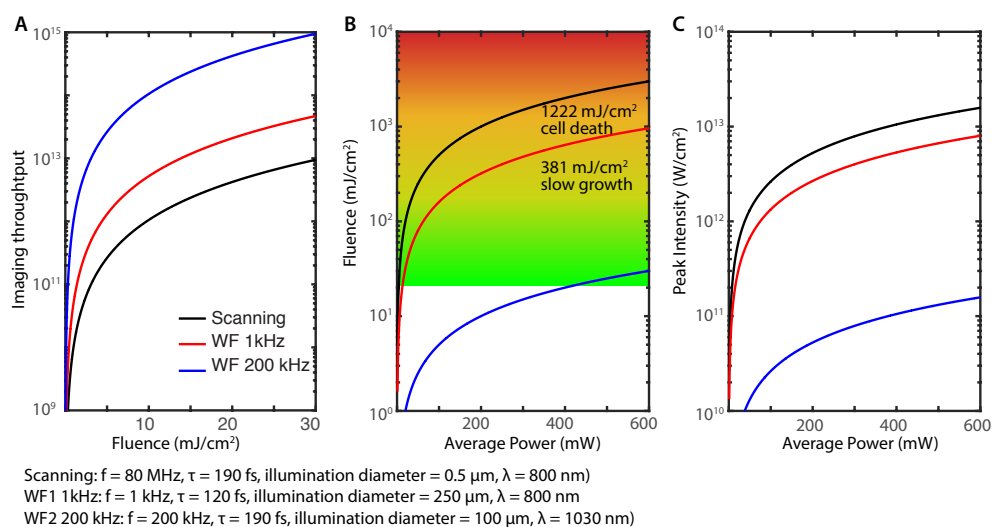


Figure 2.6 – Calculated imaging throughput. (A) The imaging throughput (number of emitted photons per second per image) for a given fluence comparing a scanning imaging system (black line), a wide-field imaging system as used in this thesis (blue line), and a 1 kHz wide-field system (red line). (B) Calculation of the delivered fluence for a given average power for the three different systems. The colored area illustrates for which fluences unstained CHO cells start to be perturbed in growth (yellow) and permanently damaged (red) [143], when illuminating with 1035 nm wavelength, 393 fs pulses, 100 kHz repetition rate, and $10 \times 50 \mu\text{s}$ dwell time. (C) For comparison, the corresponding delivered peak intensities for a given average power are also displayed.

with a Leica TCS SP5 scanning microscope in transmission mode, the blue and the red data points were obtained with the SHG wide-field system of Fig. 2.1 (using different gain settings for the camera), and the green data points were obtained by reducing the repetition rate of our laser to 1 kHz and using a regular CCD camera, i.e. without intensifier or electron multiplier, with a quantum efficiency of 50%. Figure 2.7B shows the line profile as depicted by the blue line in the inset of Fig. 2.7A, obtained for wide-field 200 kHz (red line). Figure 2.7 shows that the same contrast (image quality) can be obtained by wide-field systems (red and blue line) with acquisition times that are 2-3 orders of magnitudes shorter compared to scanning systems.

2.2 Sample Preparation, Formation and Characterization of Free-standing Lipid Bilayers

2.2.1 Lipids.

The lipids were primarily used to form lipid monolayers on an air/water interface. To this end, we dissolved lipids in chloroform at 10 mg/mL (corresponding to ~ 13 mM) concentration, sufficient to form a saturated condensed monolayer as observed with sum frequency generation [24]. To obtain a mixture of lipids, each lipid was prepared at the same molar concentration and was mixed by volume percent. The lipids in powder from (>99%, Avanti Polar Lipids, Alabama, USA) that are used in this study are: 1,2-dioleoyl-sn-glycero-3-phosphocholine (DOPC), 1,2-dipalmitoyl-sn-glycero-3-phosphocholine (DPPC), 1,2-dipalmitoyl-sn-glycero-3-phospho-L-serine (DPPS), 1,2-diphytanoyl-sn-glycero-3-phosphocholine (DPhPC), 1,2-diphytanoyl-sn-glycero-3-phospho-L-serine (DPhPS), 1,2-diphytanoyl-

2.2. Sample Preparation, Formation and Characterization of Freestanding Lipid Bilayers

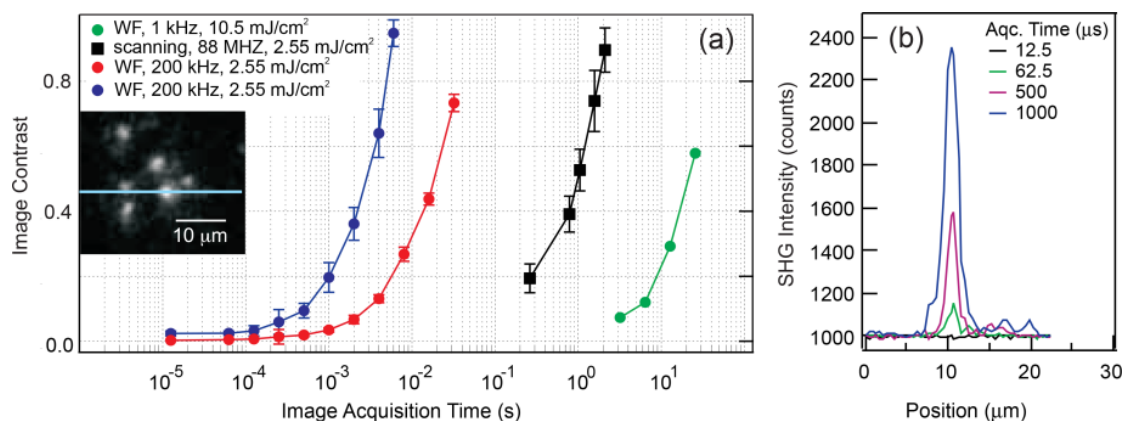


Figure 2.7 – Experimentally measured imaging throughput. (A) Measured contrast of the images recorded from the same position of the same sample in four different systems: wide-field (200 kHz, gated detection as proposed in this thesis, blue and red curves), a scanning microscope (Leica TCS SP5 with 1028 nm, 88 MHz, 190 fs laser pulses illumination, a 1.2 NA 20x water immersion objective, a scanning rate of 1000 Hz/line, image size of 256 x 256 pixels, and collecting NA of 0.9), and a wide-field 1 kHz geometry with a normal CCD camera. The fluence and the repetition rate are given in the legend. The blue data points were recorded with the intensifier and the electronic amplification of the camera both turned on whereas the red data points were recorded with only the intensifier on. The inset shows an image of the nanoparticle sample corresponding to the largest red data point. The horizontal blue line indicates the position for which the intensity cross-sections are displayed in (B). (B) Intensity (raw data) versus position for various acquisition times corresponding to the red data points in (A).

sn-glycero-3-phosphate (DPhPA), 23-(dipyrrometheneboron difluoride)-24-norcholesterol (TopFlour cholesterol), 1-palmitoyl-2-12-[(7-nitro-2-1,3-benzoxadiazol-4-yl)am-ino]dodecanoyl-sn-glycero-3-phosphocholine (NBD PC) and cholesterol (ovine wool > 98%). The chemical structures of the lipids are shown in Fig. 2.8. For most of the experiments, we used methylated lipids, DPhPC, DPhPCS, and DPhPA because they form electrically and mechanically stable lipid bilayers [145]. Furthermore, they exist in liquid-disordered phase at a wide range of temperatures (-120 to 120 °C).

2.2.2 Preparing ~100-μm-aperture in a 25-μm-thick Teflon Film.

The ~100 μm aperture was punched in the 25-μm-thick Teflon film by means of dielectric breakdown using a high-voltage discharge (BD10A High-Frequency Generator, Electro-Technic Products, USA) [146]. The Teflon film was sandwiched between the BD10A and a 127-μm tapered tip tungsten microelectrode (Science Products GmbH). The discharge melts the Teflon film and punctures a circular hole. Figure 2.9 shows the actual photograph of the punching device. The inset shows the Teflon film (25-μm-thick) sandwiched in a Teflon film holder made of thick plastic sheets with a hole in the middle.

After puncturing the Teflon film, the diameter of the hole was measured using a table-top white-light microscope. To obtain a ~100-μm-aperture, the distance between the high-voltage discharge and the tungsten microelectrode was adjusted empirically until the device can reproducibly form ~100-μm-aperture. Lastly, the punctured Teflon films were cleaned using chloroform, methanol, and ethanol, each applied three times.

Chapter 2. Experimental Details & Methodology

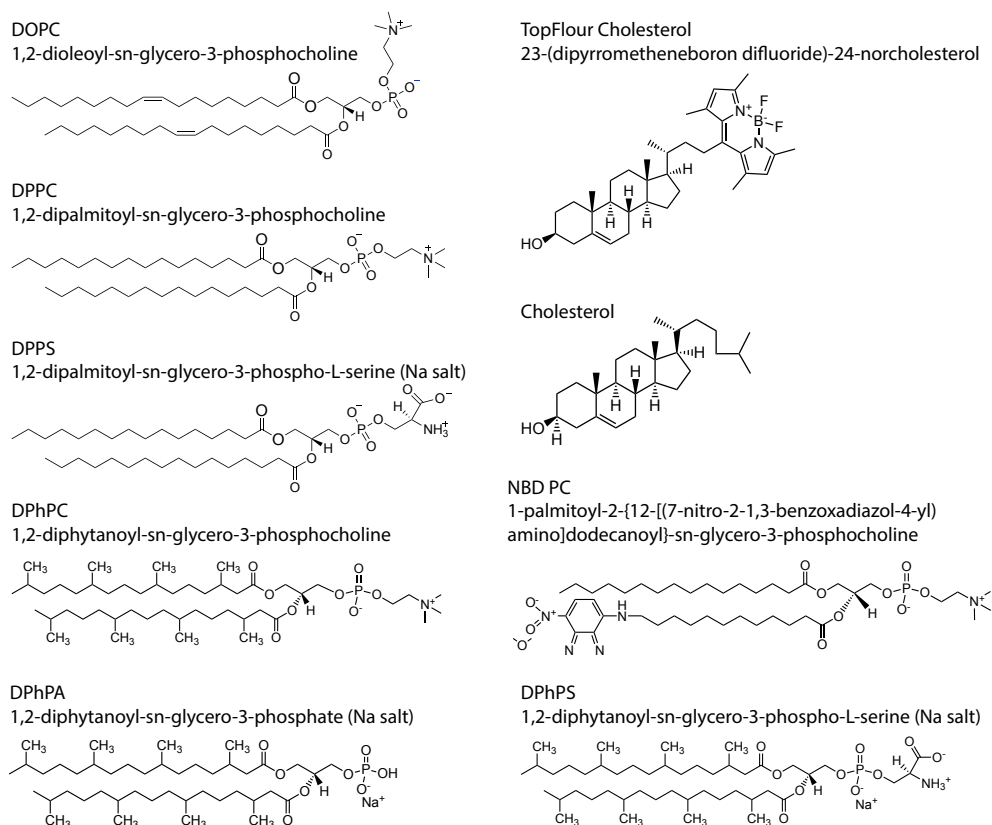


Figure 2.8 – Chemical structures of the lipids used in this study.

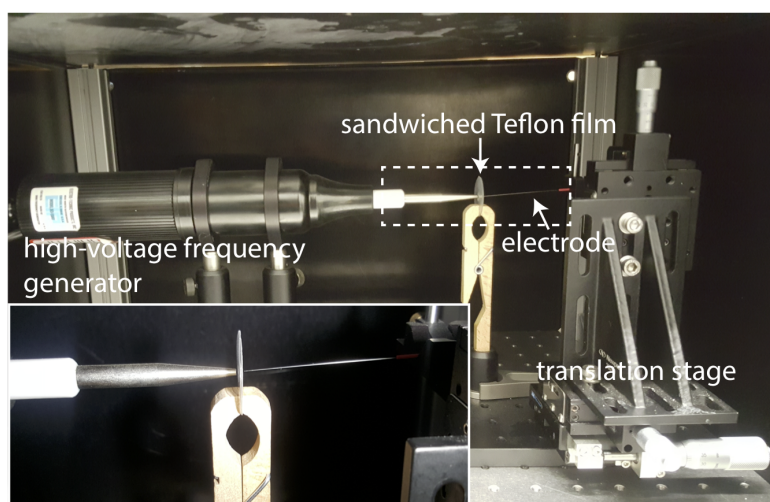


Figure 2.9 – Image of the punching device. The punching device is composed of a high-voltage discharged (BD10A high-frequency generator), a tapered tip tungsten microelectrode attached to a translation stage and a Teflon film holder that is sandwiched between the high-frequency generator and microelectrode. The inset shows a zoomed image of a Teflon film holder in between the high-voltage discharge and microelectrode.

2.2. Sample Preparation, Formation and Characterization of Freestanding Lipid Bilayers

2.2.3 Chamber design and assembly.

The Teflon chamber used to form freestanding lipid bilayer is shown in Fig. 2.10. The chamber was composed of separable top and bottom cells. Figure 2.10A shows the assembled chamber that is composed of separable top and bottom cells. The laser beams (orange color labeled beam 1 and beam 2 in Fig. 2.10A) enter the top cell through custom made holes that were directed toward the 100- μm aperture where the membrane is formed. Figure 2.10B shows the schematic of the top cell shown in different views (top - top view and bottom - bottom view). The top cell looks like a round etched bowl from the top view. A cleaned Teflon film with a 100- μm aperture was glued to the top cell using a high-vacuum silicon grease (Dow Corning). Figure 2.10C shows the schematic of the bottom cell (left - top view and right - bottom view). The coverslip is attached to the bottom cell using a medium viscous silicon glue (GE Bayer Silicones).

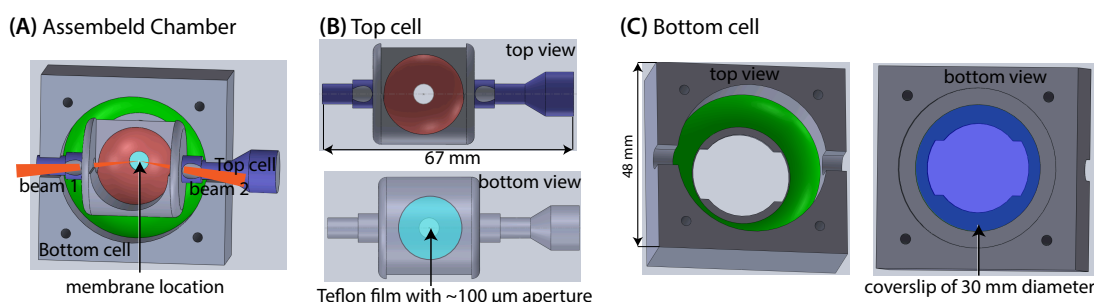


Figure 2.10 – The freestanding lipid bilayer chamber. (A) The assembled chamber is composed of top and bottom cells. The laser beams enter the top cell through openings that were directed toward the 100- μm aperture, the location of the membrane. The top and bottom cells are separable and are shown in (B) and (C) respectively. The circular light-blue structure in B (right side) shows the 25- μm thick Teflon film with a 100- μm aperture that was glued to the top cell. The circular blue structure in C (right side) shows the coverslip that was glued to the bottom cell.

The assembled bilayer chamber was mounted to the microscope by means of a custom-made microscope mount. Figure 2.11 shows the assembled bilayer chamber attached to an aluminum metal plate. The metal plate was attached to an L-shaped polyoxymethylene (POM) plastic that is mounted to the microscope by means of M4 mounting screws. The POM was chosen because of its thermal and mechanical stability. It thermally isolates the microscope from the bilayer chamber. The aluminum metal plate was chosen to facilitate heating of the bilayer chamber. Figure 2.12 shows a modified microscope mount with Peltier elements and water bath for temperature experiments. Alternatively, a copper metal plate (though heavier) can be used instead of aluminum for faster heating. A calibration curve describing time as a function of chamber temperature was performed prior to experiments involving temperature.

2.2.4 Formation of horizontal freestanding lipid bilayers

Freestanding horizontal planar lipid bilayers were formed following the Montal-Mueller technique [49, 147, 148, 149]. In this approach, two aqueous solutions were separated by a 25- μm -thick polytetrafluoroethylene (Teflon) film (Goodfellow) that contains an aperture with a 80- to 120- μm -wide diameter that was initially in contact with air. To obtain a membrane by monolayer apposition (2.13), the Teflon film with \sim 80- to 120- μm -wide diameter aperture was treated with a 99.5:0.5 vol % mixture of hexane and hexadecane. When the membrane is formed, a torus of hexadecane (the hexane evap-

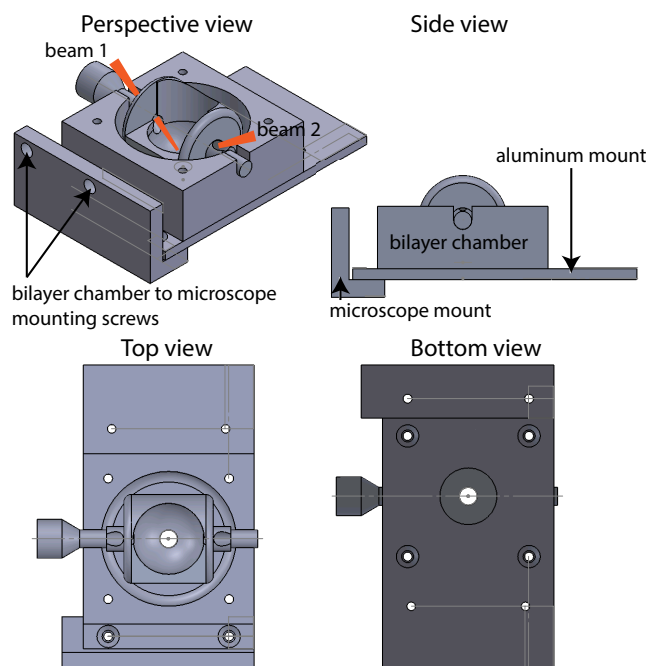


Figure 2.11 – Microscope mount. The microscope mount for the bilayer chamber facilitates the mounting of the bilayer chamber to the second harmonic microscope. The bilayer chamber was attached to an aluminum metal plate (side view) and the metal plate was mounted to the microscope by means of an L-shaped polyoxymethylene (POM) plastic. POM was chosen because of its thermal and mechanical stability. It thermally isolates the microscope from the bilayer chamber.

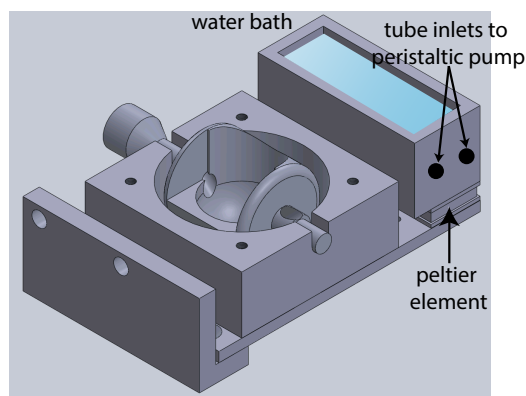


Figure 2.12 – Modified microscope mount for temperature measurements. The modified microscope mount includes a water bath and two Peltier elements for heating.

orates) forms near the periphery of the aperture and can be seen as Newton rings with white-light imaging. On each air/aqueous solution interface, a lipid monolayer was deposited by pipetting a chloroform solution that contains 10 mg/mL of the dissolved desired lipids. The treated Teflon film was moved through both interfaces such that, on each side, a membrane monolayer is formed. In the middle of the aperture, a bilayer will spontaneously form. The lipid membranes were formed between aqueous solutions. Lipid membranes composed of lipids with transition temperature above room

2.3. Methods to characterize horizontal freestanding lipid bilayers

temperature were prepared by heating the sample chamber (using Peltier elements; see Fig. 2.12) to just above the phase transition temperature. The membranes were positioned in the horizontal plane, and illuminated from above. Membranes were stable for at least 2 hours. Figure 2.13 shows an illustration of the formation of horizontal freestanding lipid bilayers and the placement of the membrane with respect to the electrodes and laser light. A representative white-light image of the bilayer and schematic of the cross-section of a freestanding lipid bilayer showing a wide oil annulus at the periphery of the membrane is also shown.

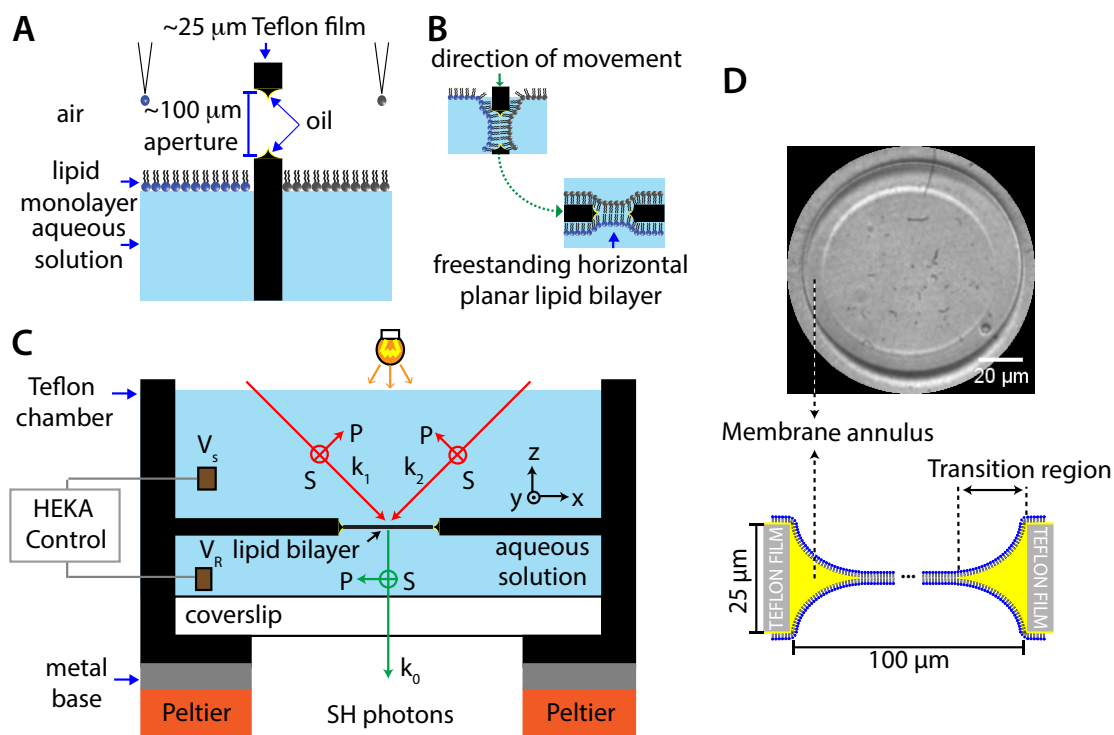


Figure 2.13 – Illustration of the formation of freestanding horizontal planar lipid bilayer. (A) Two lipid monolayers are created on an air/water interface separated by a pretreated Teflon film. (B) When the Teflon film is moved through the interface with the two different lipid monolayers, a lipid bilayer is spontaneously formed. The green dashed arrow indicates the direction of movement of the Teflon film. (C) Schematic of the sample chamber and imaging configuration. The size of the lipid membrane is not to scale. (D) Representative white-light image (top) and schematic (bottom, not drawn to scale) of a freestanding lipid bilayer (x - z plane in C) with a wide oil annulus at the periphery of the membrane.

2.3 Methods to characterize horizontal freestanding lipid bilayers

There are two complementary methods to characterize freestanding lipid bilayers: Electrical measurements of membrane capacitance and resistance and optical white-light imaging of membranes. We first describe the electrical methods followed by an example of how we characterize a freestanding lipid bilayer.

2.3.1 Electrical Measurements

Electrical measurements were performed using Ag/AgCl pellet electrodes (World Precision Instruments, Germany) that were placed on both sides of the bilayer. The current traces and applied potentials were recorded and controlled with a HEKA patch clamp amplifier (EPC 10; HEKA Elektronik, Germany) with a built-in software-based lock-in amplifier [150]. The sampling rate was set to 200 kHz. The membrane capacitance was measured using a sinusoidal voltage stimulus. The resulting sinusoidal current trace is processed using a phase-sensitive lock-in amplifier [151, 150]. All measurements were performed with the HEKA Patchmaster software (HEKA Elektronik) using the following filter settings of the EPC10 amplifier: filter 1 = 2.9 KHz and filter 2 = 10 KHz; both are Bessel filters. The sensitivity of the instrument was benchmarked with a BB914 variable capacitor (Infineon). The capacitance values can be recorded with an error of 0.02%.

To minimize the noise, every metallic component (HEKA controller, bilayer chamber, optical elements) were grounded to the optical table. The noise of the system without a Faraday cage was around $\pm \sim 5$ pA. With a Faraday cage, the noise improves to $\pm \sim 1$ pA.

Measurements of specific resistance, R_m

To measure membrane resistance, the direct current (DC) response of the membrane to a DC voltage stimulus (duration = 2 seconds, sampling rate = 200 kHz) was recorded. The voltage was scanned from -100 mV to 100 mV in steps of 10 mV. The current was plotted as a function of voltage to obtain an I-V curve and the resistance was derived from the slope of the I-V curve. The specific resistance (R_m in units of $\Omega \cdot \text{cm}^2$) was calculated by multiplying the membrane resistance (Ω) to the membrane area (cm^2). Typical acceptable values for specific resistance is, $R_m \sim 10^8 \Omega \cdot \text{cm}^2$.

Measurements of specific capacitance, C_m

HEKA Patchmaster has a built-in software lock-in amplifier that allows precise measurements of membrane capacitance. We used a sine wave stimulus, $U = U_1 \sin(2\pi f t)$ where U_1 is the amplitude of the sine wave, and f , the frequency and t , the duration of the stimulus. Depending on experimental conditions, U_1 is between 10 - 50 mV, $f = 500$ Hz and t between 10 - 500 ms corresponding to 2000 - 10000 sine wave cycles. The HEKA software models the cell membrane as a resistor (R_m) in parallel with a capacitor (C_m). The electrolyte solution on either side of the membrane introduces additional resistance in series (R_s) with the cell membrane. To measure capacitance, the HEKA uses phase sensitive admittance measurements using a built-in software-based lock-in amplifier. For the interested reader, ref. [152] describes the algorithm for software-based lock-in amplifiers. The specific capacitance (C_m in units of $\mu\text{F}/\text{cm}^2$) was calculated by dividing the membrane capacitance (μF) by the membrane area (cm^2). Typical acceptable values for specific capacitance is, $C_m > 0.7 \mu\text{F}/\text{cm}^2$.

Capacitance measurement with an applied DC bias

To determine if a bilayer is symmetric or asymmetric with respect to surface charge, capacitance minimization measurements are used. For these measurements, we used a stimulus (U) with an AC

2.3. Methods to characterize horizontal freestanding lipid bilayers

excitation U_1 and a DC bias U_0 ,

$$U = U_0 + U_1 \sin 2\pi f t \quad (2.5)$$

U_0 was varied in steps of 2mV from -125 mV to 125 mV, $U_1 = 50$ mV, $f = 50$ Hz. The recording time for one data point was 500 ms. The voltage-dependent membrane capacitance was derived from

$$C(U_0) = C_0(1 + \alpha(\Delta\Phi_0 + U_0))^2 \quad (2.6)$$

where C_0 is the membrane capacitance with $U_0 = 0$, $\Delta\Phi_0$ is the difference in surface potential, and α is a constant of proportionality [16, 153, 154]. Equation 2.6 was used to determine whether the bilayer leaflets were identical (symmetric) or different (asymmetric), as the capacitance of the membrane depends on the effective potential difference ($\Delta\Phi_0 + U_0$). For identical leaflets ($\Phi_{0,1} = \Phi_{0,2}$), the minimum of the capacitance vs. U_0 trace, $dC[U_0]/dU_0 = 0$ occurs at $U_0 = 0$, while, for nonidentical leaflets ($\Phi_{0,1} \neq \Phi_{0,2}$), it occurs at $U_0 \neq 0$.

Equation 2.5 can also be used to measure the capacitance of active channels. For this measurement, U_0 was set to the voltage required to open the channel.

2.3.2 Characterization of freestanding lipid bilayers

The presence of the lipid bilayer was ascertained by the appearance of Newton rings in the white-light image, a specific capacitance $C_m > 0.7 \mu\text{F}/\text{cm}^2$, and a specific resistance of $R_m \sim 10^8 \Omega.\text{cm}^2$ as reported in the literature [49]. Figure 2.14A shows a white-light image of the Teflon film with the aperture placed in the center of the field of view immersed in an aqueous solution. The same aperture appears with diffraction rings after the formation of a membrane as shown in Fig. 2.14B. The ring looks slightly distorted as the white-light source is placed off center. The rings arise from the interference pattern of the photons originating from the monolayer leaflets as they transition to form a bilayer (see Fig. 3.1). Figure 2.14C shows a capacitive current trace (green) in response to an applied stimulus (blue). The specific resistance and specific capacitance are $R_m = 4.5 \pm 1.9 \times 10^7 \Omega.\text{cm}^2$ and $C_m = 0.81 \pm 0.08 \mu\text{F}/\text{cm}^2$, respectively, indicating that a membrane bilayer was indeed formed [49].

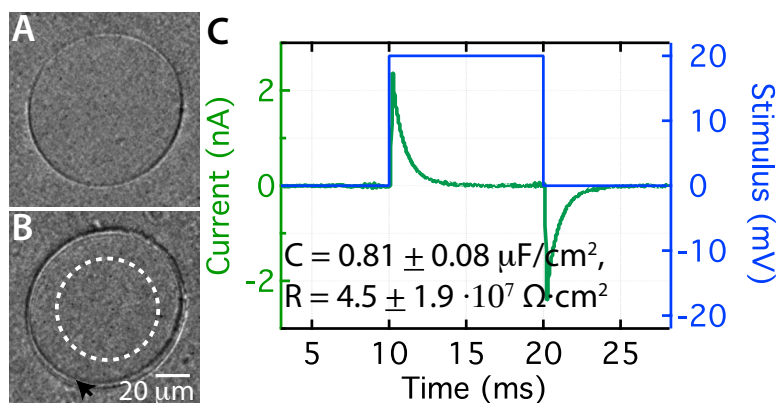


Figure 2.14 – Characterization of the freestanding horizontal planar lipid bilayers. (A and B) Wide-field image of the aperture (A) without a lipid bilayer and (B) with a lipid bilayer. The black arrow points to the presence of interference fringes, “Newton rings.” The scale bar is the same for A and B. (C) Capacitive current trace (green) of a typical freestanding planar lipid membrane using a 20-mV stimulus (blue). The measured specific capacity of the membrane is greater than $\mu\text{F}/\text{cm}^2$ with membrane-specific resistance on the order of $10^8 \Omega \cdot \text{cm}^2$ ($R_m = 4.5 \pm 1.9 \times 10^7 \Omega \cdot \text{cm}^2$, $C_m = 0.81 \pm 0.08 \mu\text{F}/\text{cm}^2$, $n = 7$ membranes).

3 The interaction of oil and lipids in freestanding lipid bilayer membranes

The interaction of oils and lipids is relevant for membrane biochemistry since the cell uses bilayer membranes, lipid droplets, and oily substances in its metabolic cycle. In addition, a variety of model lipid membrane systems, such as freestanding horizontal membranes and droplet interface bilayers, are made using oil to facilitate membrane monolayer apposition. We characterize the behavior of excess oil inside horizontal freestanding lipid bilayers using different oils, focusing on hexadecane and squalene. Using a combination of second-harmonic (SH) and white-light imaging, we measure how oil redistributes within the membrane bilayer after formation. SH imaging shows that squalene forms a wider annulus compared with hexadecane, suggesting that there is a higher quantity of squalene remaining in the bilayer compared with hexadecane. Excess oil droplets that appear right after membrane formation are tracked with white-light microscopy. Hexadecane droplets move directionally to the edge of the membrane with diffusion constants similar to those of single lipids, whereas squalene oil droplets move randomly with lower diffusion speeds similar to lipid condensed domains and remain trapped in the center of the bilayer for ~1-3 h. We discuss the observed differences in terms of different coupling mechanisms between the oil and lipid molecules induced by the different chemical structures of the oils.

This chapter is based on the author's journal article: **O. B. Tarun**, M. Yu Eremchev, S. Roke. *Langmuir*, 34, 11305-11310 (2018).

3.1 Introduction

The lipid bilayer membrane that surrounds cells and organelles performs a wide variety of functions ranging from regulating transport to signaling and providing a protective barrier. As such, membranes come in contact with many substances, for example, with lipid droplets. Lipid droplets are composed of an oil-based core covered with a monolayer of lipids and proteins, which serve for energy storage and play a fundamental role in cell metabolism [40]. These lipid droplets can merge with cell membranes and deposit their oily core within the bilayer [39]. It can therefore be expected that lipid membranes can at times contain hydrophobic molecules. In addition, oily substances within the bilayer are relevant for a variety of membrane processes. For example, some proteins require a thicker hydrophobic core (such as perlipins or alcoholdehydrogenases) to function optimally; [155, 38, 156, 157], trans-membrane motion (flip-flop), membrane diffusion, and raft formation require membrane reorganization [158, 4] that is influenced by oil. Thus, the interactions of oily substances with lipids are relevant for biological processes. However, there is no molecular level information about the interactions of oil and lipids in real cells or even in freestanding model membrane systems that are recognized to capture essential membrane biophysics/chemistry [16]. Although many model membrane studies [79, 159, 160, 42, 161, 149, 49] focus on the phase behavior of lipids [4, 5, 6] or lipids and steroids, [7, 8, 9] not much work has been dedicated to the interaction of hydrophobic oils and lipids. In addition, oils are needed to prepare the membrane system, such as in the case of freestanding lipid bilayers [149, 49] and droplet interface bilayers [162]. From this point of view, it is of interest to understand better how oils and lipids interact and what this interaction means for the properties of the membrane.

Here, we study the interaction of oil with freestanding lipid bilayer membranes using white-light and label-free non-resonant second-harmonic (SH) imaging. The freestanding bilayers are formed in a $\sim 100\ \mu\text{m}$ wide and $\sim 25\ \mu\text{m}$ thick aperture in a Teflon film that is pre-painted with an oil mixture. This oil serves as a transition material between the Teflon edge ($25\ \mu\text{m}$ thick) and the lipid membrane ($\sim 6\ \text{nm}$ thick) [49]. Figure 3.1A shows a top view image of the Teflon ring with a membrane in the center of the aperture. At the perimeter of the bilayer region, there is a transition region that contains oil. This region can be seen as an annulus in the wide field image of Figure 3.1A and contains a volume of oil that is located between the edge of the aperture and the lipid bilayer, sketched as a side view in Figure 3.1A. We determine how oil redistributes within the bilayer after membrane formation and assess whether oil remains between or within opposing leaflets or leaves the bilayer region after equilibration. We vary the structure of the oil studying saturated alkanes (hexadecane and heptadecane) and a branched oil structure (squalene); see Figure 3.1B. We observe differences in the interaction of both types of oils with the membrane system. Hexadecane droplets are seen to move directionally to the edge of the membrane with diffusion constants similar to those of single lipids. Squalene oil droplets move randomly with lower diffusion speeds similar to lipid condensed domains and remain trapped in the center of the bilayer for $\sim 1\text{-}3\ \text{h}$. We discuss the observed differences in terms of different coupling mechanisms between the oil and lipid molecules induced by the different chemical structures of the oils.

3.2 Materials and Methods

3.2.1 Chemicals and lipids

DOPC, hexadecane ($\text{C}_{16}\text{H}_{34}$, 99.8%, Sigma-Aldrich), squalene ($\text{C}_{30}\text{H}_{50}$, >98%, Sigma-Aldrich), heptadecane ($\text{C}_{17}\text{H}_{36}$, 99.5%, Sigma-Aldrich), hexane (C_6H_{14} , Sigma-Aldrich, >99%), chloroform (Merck,

>99.8%), hydrogen peroxide (30%, Reactolab SA), sulfuric acid (95-97%, ISO, Merck), KCl (99.999%, Aros), HEPES (ACS Reagent, Sigma-Aldrich) were used as received. All aqueous solutions were made with ultra-pure water (H₂O, Milli-Q UF plus, Millipore, Inc., electrical resistance of 18.2 MΩ cm). All aqueous solutions were filtered with 0.1 μm Millex filters. The coverslips used in the imaging were pre-cleaned with piranha solution (1:3 - 30% H₂O₂: 95-97% H₂SO₄) and thoroughly rinsed with ultrapure water.

3.2.2 Freestanding horizontal planar lipid bilayers

Freestanding horizontal planar lipid bilayers were formed by monolayer apposition that is initially in contact with air and separated by a Teflon film, following the Montal-Mueller technique (see Chapter 2.2 for details). Prior to membrane formation, the aperture was treated with a pre-painting solution of 99.5:0.5 vol% mixture of hexane and a pre-painting solvent (hexadecane, heptadecane or squalene) depending on the experiment. Electrical measurements for all membranes tested yielded specific capacitance (C_m) > 0.7 μF/cm² and specific resistance (R_m) > 10⁷ Ω.cm² indicating a “thin” membrane bilayer was formed. The presence of trapped oil droplets do not significantly change the measured capacitance.

3.2.3 Imaging experiments

The same optical setup (see Chapter 2.1 for details) was used for SH imaging and two-photon fluorescence imaging. All images were recorded with a 50× objective lens (Mitutoyo Plan Apo NIR HR Infinity-Corrected Objective), with the beams polarized parallel to the plane of incidence (P). For fluorescence measurements, a 550 nm long pass filter (FEL0550, Thorlabs) was placed before the detector to detect the outgoing two-photon fluorescence. The Teflon edge emits a weak fluorescence.

3.2.4 White light imaging and tracking

White-light imaging was performed using a white-light lamp that illuminates the membrane from the top (see Chapter 2.1 for details). Tracking of oil droplets was done using the ImageJ TrackMate plugin. Prior to tracking, the images were filtered with a Gaussian blur, $\sigma = 2$ pixels along the time axis. The following parameters from the ImageJ plugin were used for tracking: LoG (Laplacian of Gaussian) detector, estimated blob size: 5 μm, minimum blob diameter: 3 μm, nearest neighbor tracker, linking max distance: 3 μm. The TrackMate plugin of ImageJ outputs the trajectories of the tracked oil droplets and allows calculation of the mean square displacement (MSD). To obtain the diffusion coefficient, the mean square displacement (MSD) vs delay curves were fitted with a linear fit. The MSD curve used for linear fitting is less than 20% of the total number of steps.

3.3 Results & Discussions

SH and White-Light Imaging of Freestanding Horizontal Bilayers. Capacitance measurements of freestanding membranes [163, 164, 165] have been performed for bilayers prepared with various oils. These studies suggest that the apposition of two lipid monolayers drives the oil to the edges of the bilayer (into the transition region that we term the annulus) [10]. Since capacitance is inversely proportional to thickness, high-capacitance membranes are interpreted as thin membranes and the

Chapter 3. The interaction of oil and lipids in freestanding lipid bilayer membranes

calculated thickness that is measured matches the thickness of the hydrophobic core of a bilayer, thus suggesting that freestanding bilayers are solvent free for squalene and hexadecane [49, 163]. Later studies performed with oils that have varying alkane chain lengths showed that bilayers prepared with short chain alkanes have a lower capacitance, suggesting that shorter chain alkanes have the tendency to stay in the middle of the bilayer [160, 149, 164, 165]. In this study, we investigate these findings more deeply and focus on the behavior of hexadecane and squalene. Figure 3.1D shows a SH image (SHG, green) and two-photon fluorescence (2PF, red) of a symmetric neutral membrane composed of 1,2-dioleoyl-sn-glycero-3-phosphocholine (DOPC). The images are collected with all beams polarized in the P direction (with the electric field oscillating in the plane of the wave vectors of the beams). The line profiles (10 pixels wide) marked by the dashed lines in Figure 3.1D are shown in Figure 3.1E. The 2PF intensity decreases from the edge (red), whereas the SH signal vanishes in the center and increases toward the edge while displaying oscillations. The 2PF arises from the Teflon film and decays smoothly. This decay arises from the shape of the aperture, as the opening in the

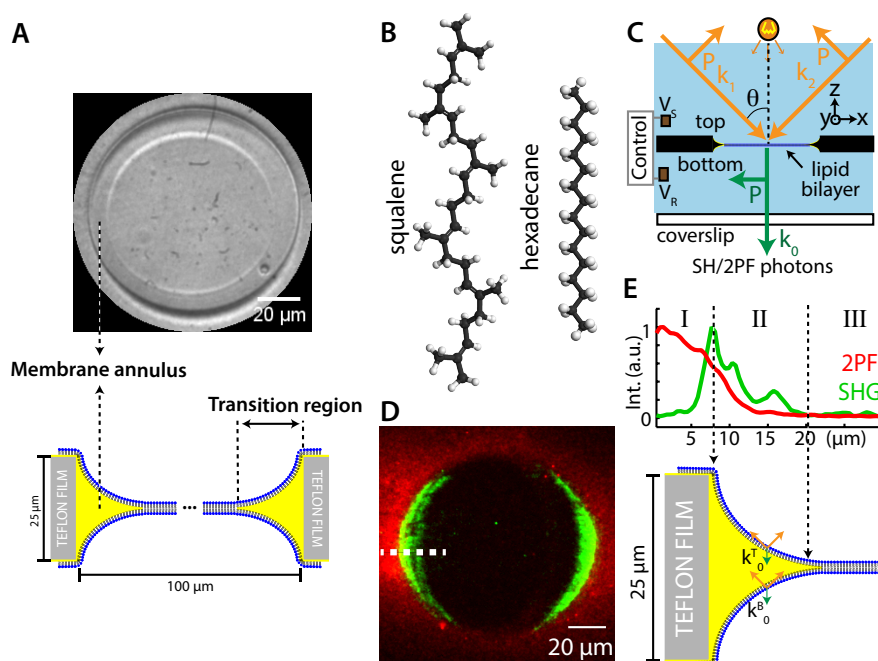


Figure 3.1 – Second-harmonic (SH) imaging of freestanding lipid bilayers. (A) White-light image (top) and schematic (bottom, not drawn to scale) of a freestanding 1,2-dioleoyl-sn-glycero-3-phosphocholine (DOPC) lipid bilayer with a wide oil (squalene) annulus at the periphery of the membrane. (B) Illustrations of the alkanes used in this study. (C) Schematic of the imaging setup with counterpropagating pulsed beams that overlap in space and time to illuminate the membrane (blue). The second-harmonic (SH) and two-photon fluorescence (2PF) photons are collected in the phase-matched direction. Abbreviations: P, polarization direction in the plane of incidence; $k_{1/2}$, wave vector of the excitation beams; k_0 , wave vector of the emitted beam; V_S , signal electrode; and V_R , reference electrode. (D) SH (green) and two-photon fluorescence (red) images of a symmetric neutral membrane composed of DOPC. (E) Line profiles (10 pixels wide) of the dashed lines in (D) with the vertical cross section (x - z plane in (C)) of the sample showing the structure of the Teflon film (gray, region I), oil (yellow), and monolayer leaflets (blue) (region II) thinning to form a lipid bilayer in the aperture center (region III). k_0^T and k_0^B correspond to the second-harmonic photons generated from the top and bottom bilayer leaflets, respectively.

Teflon film is tapered and not cylindrical. In terms of structure, going from the edge (region I) of the Teflon film toward the center, there is a transition region composed of an oil phase bordered by a lipid/water interface. This transition region (region II) thins toward the center of the lipid film (region III). The central part of the symmetric bilayer (region III) generates no SH photons (green line profile) because within the dipole approximation [73], oppositely oriented polar molecules in and around the symmetric bilayer interfere destructively (emitting SH light with a phase difference of π) and do not emit SH photons. This also suggests that there are no oil molecules detected from the center since as little as a monolayer of oil would lead to breaking of centrosymmetry. However, the transition region at the edge (region II) generates SH photons. The intensity increases toward the edge, coinciding with an increasing distance between the monolayer leaflets. The reason for the SH generation is that the symmetry of the (symmetric) bilayer is gradually broken, as the SH photons (k_0^T and k_0^B from the top and bottom leaflets) are emitted with phases that deviate from π such that the interference becomes more constructive toward the edge of the film. The coherence length is defined as $l_c = \pi \Delta k_z^{-1}$, where Δk_z the wave vector mismatch is given by $\Delta k_z = |\mathbf{k}_{1z} + \mathbf{k}_{2z} - \mathbf{k}_{0z}| = k_{1z} + k_{2z} - k_{0z}$, $\mathbf{k}_{1/2}$ as the incoming wave vectors and \mathbf{k}_0 as the outgoing wave vector. In our experiment, the phase matching distance is 386.5 nm and the corresponding coherence length l_c is 1.2 μm . As the leaflets curve toward the Teflon edge, the SH intensity displays minima and maxima that arise from phase changes dependent on the distance between leaflets. In addition to this beating, as the monolayer leaflets curve, the orientation of the interface changes relative to the polarization direction of the incoming electric fields such that the interface and the polarization become more parallel. This process ensures that the SH intensity displays an overall increase. The combined effect results in the pattern displayed by the green curve in Figure 3.1E.

The intensity distribution of the SH images is thus sensitive to the distance between the leaflets, and the SH intensity distribution of a symmetric bilayer can be used to estimate the presence of oil in the bilayer. The width of region II in Figure 3.1D quantifies the width of the annulus and the amount oil in the bilayer. We can thus use this property to investigate the interaction of squalene and hexadecane with the lipid bilayer. If the annulus is wide, it means the oil mixes more easily with the lipids in the bilayer region. If the annulus is narrow, it means that there is less interaction between the lipids in the bilayer and the oil molecules.

Figure 3.2A,B shows the SH response at the edge of the Teflon film comparing hexadecane (A, green) and squalene (B, red). The width of the annulus of the bilayer is defined as the width of region II in Figure 3.1E. Figure 3.2C shows the width of the annulus for hexadecane and squalene, summarizing the results of several membranes (6 and 12 different bilayers, respectively). It can be seen that squalene laterally extends further into the bilayer compared with hexadecane.

When bilayers are formed, they are typically left to equilibrate for several minutes [149, 49] while the capacitance increases until it levels off. This is interpreted as thinning of the bilayer. In what follows, we investigate this equilibration process for hexadecane and squalene using white-light imaging. Directly after formation of the bilayer, the white-light images display spherical structures or microlenses (see inset in Figure 3.2D), which also appear in SH images. In the time span of minutes, these structures redistribute across the images. We follow these structures and obtain tracks shown in Figure 3.2D. The black arrows point to the direction to which the microlenses move. It can be seen that hexadecane (green) moves directionally to the edge of the membrane (see the arrows) whereas squalene (red) stays in the center and moves randomly. Figure 3.2E displays the calculated diffusion coefficients for several tracks ($N = 31$ for squalene and $N = 15$ for hexadecane, see Appendix, section 3.5.2 for mean square displacement curves). The mean diffusion coefficient for hexadecane is 1.8

Chapter 3. The interaction of oil and lipids in freestanding lipid bilayer membranes

$\pm 1.0 \mu\text{m}^2/\text{s}$ and for squalene is $0.16 \pm 0.24 \mu\text{m}^2/\text{s}$. Thus, hexadecane droplets diffuse an order of magnitude faster than squalene. These numbers suggest that for a $100 \mu\text{m}$ diameter membrane, a hexadecane droplet needs $\sim 10^2$ s to leave the center of the bilayer and move to the reservoir at the edge (assuming directional movement). In contrast with the random movement of squalene, $\sim 10^4$ s are required for squalene droplets to cover the whole membrane area and accidentally meet the edge. Therefore, squalene could be trapped within the bilayer for the duration of a typical experiment (1-3 h) whereas hexadecane has a higher propensity to move to the edge on the timescale of a few minutes.

Concerning the observed difference in the diffusion coefficients of the oil droplets, the propensity of squalene to diffuse slowly is likely linked to its structure. There are two possible extremes for the average main orientation of the oil: (i) parallel to the membrane, i.e., the oil molecules are primarily situated between the bilayer leaflets, as shown in Figure 3.3A, or (ii) perpendicular to the membrane, i.e., the oil molecules are oriented parallel with respect to the lipids acyl chains and are either localized within a single leaflet or in both leaflets, as shown in Figure 3.3B. There are several important structural differences between squalene and hexadecane. Squalene, with 30 C atoms, is larger than hexadecane, with 16 C atoms. Squalene is thus also larger than the lipid acyl chains, whereas hexadecane has the same size. Furthermore, the presence of double bonds in squalene leads to a stiff comblike molecular conformation. Such a structure facilitates anchoring of squalene to the hydrophobic core. In contrast, the cylindrical structure of hexadecane does not provide this kind of molecular friction and can be more easily expelled to the oil reservoir at the edges. Both differences will ensure larger molecular friction with the acyl tails for squalene than for hexadecane.

To gain more insight into the oil/lipid interactions, we can compare our diffusion values to the diffusion of single lipids and lipid domains that have been measured by fluorescence imaging. Single-lipid diffusion was measured using fluorescence correlation spectroscopy [148] and fluorescence

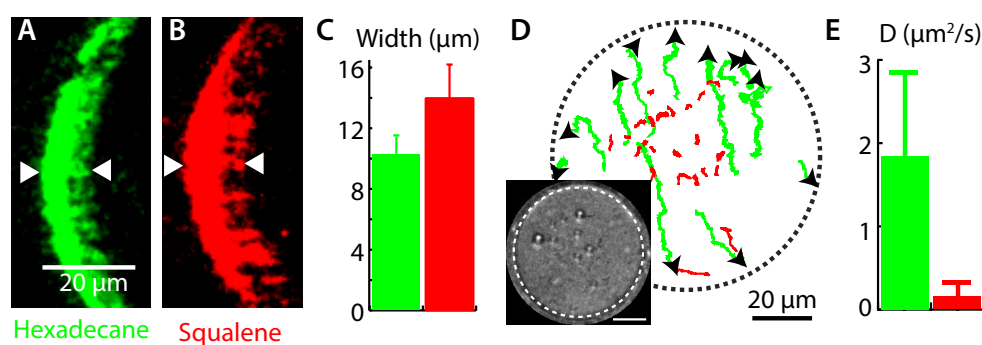


Figure 3.2 – Second-harmonic (SH) and white-light imaging of oil and lipid interactions comparing hexadecane and squalene. SH images of bilayers at the edge of the Teflon film (region II in Figure 3.1E) for a symmetric neutral membrane composed of DOPC prepared with (A) hexadecane and (B) squalene. (C) The width of the annulus is quantified by the distance between the white arrows, as shown in (A) and (B). Squalene has a wider width and thus laterally extends further to the bilayer (see Appendix, section 3.5.1). (D) Selected white-light tracks of trapped oil microlenses showing the directional diffusion of hexadecane (green) and random diffusion of squalene (red). The black arrows indicate the direction of movement. The inset shows a typical white-light image of trapped oil microlenses that appear as bright spots. The scale bar is $20 \mu\text{m}$, and the dashed circles indicate the Teflon edge. (E) Calculated diffusion coefficients from the mean square displacement curves (see Appendix, section 3.5.2) comparing squalene and hexadecane. Squalene diffuses an order of magnitude slower than hexadecane.

recovery after photobleaching [166] and is in the order of 10^0 - $10^1 \mu\text{m}^2/\text{s}$. Diffusion of liquid-ordered domains in a bilayer, on the other hand, is in the order of 10^{-3} - $10^{-1} \mu\text{m}^2/\text{s}$ [4]. The diffusion coefficients found for hexadecane ($1.8 \pm 1.0 \mu\text{m}^2/\text{s}$), agree with those found for single-lipid diffusion, whereas the diffusion coefficients found for squalene ($0.16 \pm 0.24 \mu\text{m}^2/\text{s}$) fall in the range of lipid domain diffusion. This agreement suggests that hexadecane diffuses in a similar manner as lipids in a single leaflet, which would mean that hexadecane is oriented perpendicular to the membrane and located primarily within a single leaflet, parallel to the acyl chains as shown in Figure 3.3B. On the contrary, squalene moves much slower, which, agrees with a squalene induced coupling between the leaflets which could come about either by being oriented perpendicular to the acyl chains of the lipids (Figure 3.3A) or by being oriented parallel to the lipid acyl chains but spanning over both leaflets as shown in Figure 3.3B. Since the capacitance values allow a range of thicknesses they are inconclusive regarding the orientation of the oil molecules. Therefore, further investigations are required to confirm these mechanisms (for example by polarized total internal reflection Raman (TIR-Raman) spectroscopy [167] or sum frequency generation [168]).

Experiments in ref [163] showed that freestanding membranes formed with heptadecane have the highest specific capacitance compared with bilayers formed with other alkanes. Similar conclusions were drawn from experiments on droplet interface bilayers in refs [162], [169], suggesting that longer alkyl chains due to their cylindrical structure (but still fitting within one leaflet) should generate more ideal bilayers. To test this hypothesis, we formed freestanding membranes using heptadecane and obtained white-light images immediately after membrane formation (thus, before the equilibrated stage investigated in Figures 5.1 and 3.2A,B). Figure 3.3C shows the white-light image for a bilayer prepared with heptadecane ~ 5 s after membrane formation. In comparison, Figure 3.3D shows the white-light image for a bilayer prepared with hexadecane ~ 5 s after membrane formation. We observe that the thickness of oil at the edge of the Teflon film is markedly wider for heptadecane directly after membrane formation than for hexadecane, suggesting that immediately after membrane formation, most of the oil is already squeezed out. Waiting longer, ~ 15 min after membrane formation, Figure 3.3E,F shows the corresponding white-light image for heptadecane and hexadecane. We observe in Figure 3.3E,F that the thickness of the oil at the edge increases for hexadecane but not for heptadecane.

The above findings suggest that to use a freestanding bilayer system that is completely free of oil, the best chance to reach such a state is by using heptadecane as oil. The disadvantage of using heptadecane is the melting point, $T_m = 23$ °C, thus requiring temperature control. The practical approach is to use hexadecane ($T_m = 18$ °C) and wait long enough for oil to be squeezed out. In addition, from a biochemical-interaction perspective, every living cell contains lipid droplets that are composed of an oily interior (with cholesterol, triglycerides, cholesterol esters, and unsaturated fatty acids) covered with a lipid monolayer [40, 39, 38, 170, 171]. These droplets move freely through the cytoplasm and can merge with the various membranes in the cell. They can be formed by budding-off from a membrane. Although cell membranes are far more complex than the freestanding membrane model studied here and the oil structures are only comparable but not identical, the information found about the interaction of oil and lipids provides insight into the state of oil inside lipid bilayers, which is useful for understanding the same type of interactions in biological systems.

3.4 Summary and Conclusions

In summary, we investigated the interaction of oil with freestanding lipid bilayers in aqueous solution using second harmonic and white-light imaging. We find that even on equally high-capacitance lipid

Chapter 3. The interaction of oil and lipids in freestanding lipid bilayer membranes

membranes that are prepared with squalene and hexadecane, there are differences in the membrane structure. From the SH intensity profile and the white-light temporal image stacks, we conclude that the curvature of monolayers at the edge of the Teflon film of freestanding bilayers prepared with hexadecane is higher compared with squalene, indicating that less hexadecane is present within the bilayer. Conversely, it seems there is a higher quantity of squalene remaining in the bilayer since squalene forms a wider annulus. The diffusion tracks show directed diffusion of hexadecane droplets after membrane formation, with a diffusion coefficient of $1.8 \mu\text{m}^2/\text{s}$ (i. e., around 10^2 s, the oil droplets have been expelled to the Teflon edge), whereas squalene shows no directed motion, with a diffusion coefficient of $0.16 \mu\text{m}^2/\text{s}$. There is a similarity with single-lipid diffusion (hexadecane) and lipid domain diffusion (squalene). This difference is caused by the difference in structure: hexadecane can stay within a single leaflet and diffuse through the liquid phase of the lipids. Squalene on the other hand is bigger than a single leaflet and also more branched, so it will couple to both leaflets and move slower. These differences and the related interaction mechanisms are important when considering what type of bilayer system needs to be used. They may also influence membrane properties in biological systems.

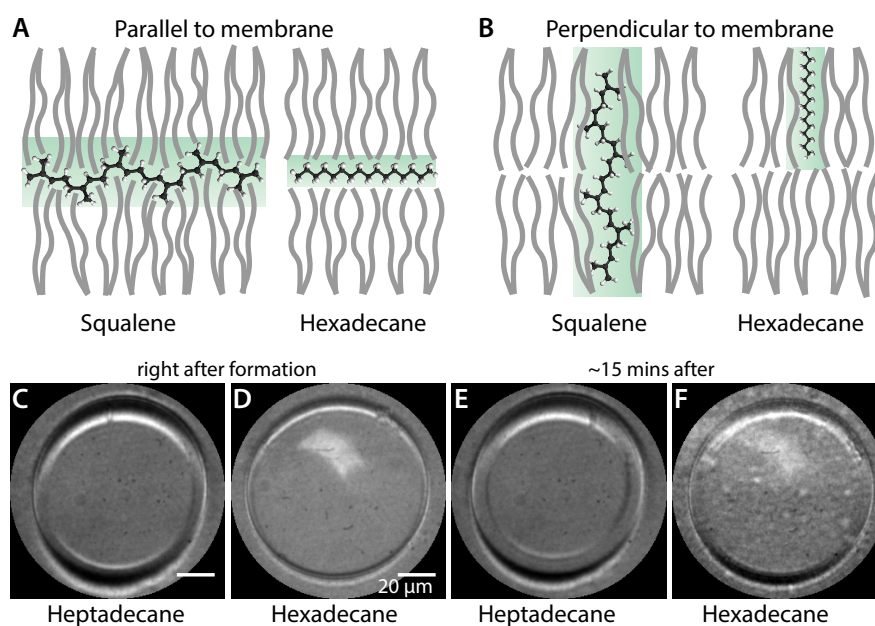


Figure 3.3 – Possible mechanisms for the interaction of oil inside a lipid bilayer. Illustration of the proposed mechanism that explains the observed difference in diffusion when oil is oriented parallel to the membrane plane (A) and oil is oriented perpendicular to the membrane (B). Interdigitating oil with acyl chains is easier for squalene (A, left) than for hexadecane (A, right). The larger size of squalene can span both bilayer leaflets (B, left) compared with hexadecane. The molecular friction for squalene is larger compared to that of hexadecane, thus retarding its diffusion. White-light images of freestanding membranes immediately after formation (C, D) and ~ 15 min after formation (E, F) for membranes prepared with hexadecane and heptadecane. The thickness of oil near the Teflon edge immediately after formation for membranes prepared with heptadecane is wider compared to that for membranes prepared with hexadecane. The scale bar is the same for all images. The Teflon edge is visible, and the white-light is positioned obliquely coming from the top. The bright shape in the bilayer center in (D, F) is the reflection from the lamp.

3.5 Appendix

3.5.1 Measurement of the width of the annulus

The width of the annulus was measured using a Matlab code. Figure 3.4 shows the SH images of symmetric neutral DOPC bilayers at the edge of the Teflon film prepared with hexadecane (Fig. 3.4A) and squalene (Fig. 3.4B). The width is defined as shown in Fig. 3.4C. The threshold intensity (dashed red line in Fig. 3.4C) at which the bilayer leaflets is considered to interfere destructively is defined as the $I_{TH} = \mu_{center} + \sigma_{center}$, where μ_{center} is the mean SH intensity and σ_{center} the standard deviation of a $10 \mu\text{m} \times 10 \mu\text{m}$ region of interest in the bilayer center, where a symmetric bilayer exists. Squalene has wider annulus as it thins towards the bilayer center.

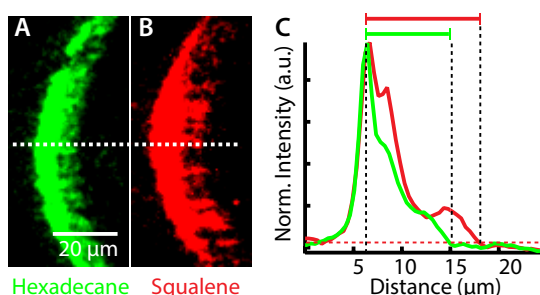


Figure 3.4 – Measurement of the width of the annulus of freestanding membranes. SH images of bilayers at the edge of the Teflon film for a symmetric neutral DOPC bilayer prepared with (A) hexadecane (green) and (B) squalene (red) and the corresponding line profiles in (C). The width of the annulus is defined as the width of the line profile from the maxima to the point where it crossed the threshold red dashed line in Fig. S1C. The magnitude of the threshold is defined as the mean + standard deviation of a $10 \mu\text{m} \times 10 \mu\text{m}$ region of interest in the center of the bilayer.

3.5.2 Diffusion of oil droplets for bilayers prepared with hexadecane and squalene

White light movies (acquisition time of 42 ms or 62 ms with at least 1000 frames) were tracked with ImageJ Trackmate plugin. Figure 3.5 shows the corresponding mean square displacement curves of oil droplets in bilayers prepared with hexadecane and squalene. It can be seen that hexadecane covers a bigger mean square displacement compared to squalene at each temporal delay.

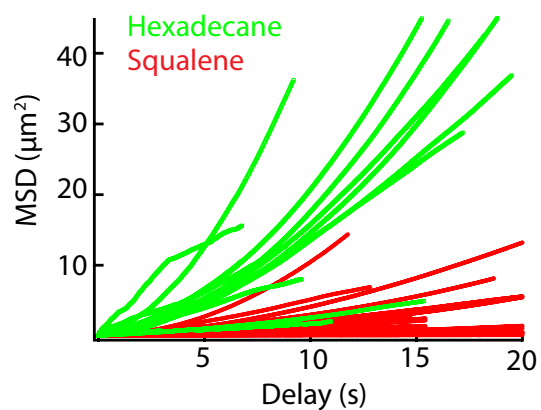


Figure 3.5 – Diffusion of oil droplets. Mean square displacement curves (MSD, μm^2) vs delay (τ , s) of oil droplets for bilayers prepared with hexadecane (N=15) and squalene (N=31).

4 Label-free and charge-sensitive dynamic imaging of lipid membrane hydration on millisecond time scales

Biological membranes are highly dynamic and complex lipid bilayers, responsible for the fate of living cells. To achieve this function, the hydrating environment is crucial. However, membrane imaging typically neglects water, focusing on the insertion of probes, resonant responses of lipids or the hydrophobic core. Owing to a recent improvement of second harmonic (SH) imaging throughput by three orders of magnitude, we show here that we can use second harmonic imaging to follow membrane hydration of freestanding lipid bilayers on millisecond time scales. Instead of using the UV/VIS resonant response of specific membrane-inserted fluorophores to record static SH images over time scales of >1000 seconds, we SH imaged symmetric and asymmetric lipid membranes, while varying the ionic strength and pH of the adjacent solutions. We show that the non-resonant second harmonic response of water that is aligned by charge-dipole interactions with charged lipids can be used as a label-free probe of membrane structure and dynamics. Lipid domain diffusion is imaged label-free by means of the hydration of charged domains. The orientational ordering of water is used to construct electrostatic membrane potential maps. The average membrane potential depends quadratically on an applied external bias, which is modeled by nonlinear optical theory. Spatiotemporal fluctuations are seen on the order of 100 mV changes in the membrane potential. These changes imply that membranes are very dynamic, not only in their structure but also in their membrane potential landscape. This may have important consequences for membrane function, mechanical stability and protein / pore distributions.

This chapter is based on the author's journal article: **O. B. Tarun**, C. Hanneschläger, P. Pohl, S. Roke. Proceedings of the National Academy of Sciences, 115(16), 4081 (2018).

4.1 Introduction

The properties of membranes around cells and organelles are critically determined by the structural and dynamical properties of lipid membranes [53, 172]. The distribution of charge, chemical composition, and presence or absence of domains at membranes determine the traffic in and out of cells, the structural integrity, and the response of cells to their environment, even leading to cell death [173]. In addition, the hydration of lipid membranes is key to their structural integrity: Without water, lipids will not self-assemble into a membrane structure or remain stable. Imaging membrane hydration, the dynamics of charge, lipid domain formation, and diffusion is a formidable challenge relevant for understanding membrane properties and utilizing them for treating related diseases, such as neurodegenerative disorders [174]. Owing to the importance of membranes, a wide variety of imaging methods are used that are either geared toward measuring the fate of membrane-inserted probes and their relation with the membrane, such as confocal fluorescence microscopy [7, 175], stimulated emission depletion far-field fluorescence nanoscopy [56], and superresolution fluorescence imaging [176], or to probe the resonant response, using coherent anti-Stokes Raman scattering microscopy [63, 64, 65], or stimulated Raman scattering microscopy [69]. Refractive index contrast or the height difference of the hydrophobic core of the membrane that are substrate-dependent are also employed in methods such as interferometric scattering microscopy [62], ellipsometry [61], and atomic force microscopy [55, 12]. Second-harmonic (SH) and sum frequency (SF) generation have been recognized as powerful probes of membrane function: The intrinsic symmetry selection rule that applies to both methods ensures that centrosymmetric structures such as ideal single-component lipid bilayers do not emit SH or SF photons. With this in mind, the vibrational response of lipids in supported lipid membranes was used to spectroscopically probe transmembrane lipid motion [177] and lipid acyl chain conformation in monolayers on air/water interfaces [24]. SH imaging studies have been performed on lipid bilayers deposited on a substrate in which the UV resonance of specific drugs or chiral molecules was employed to record static structural maps [51, 50]. Another study employed static SH imaging to confirm single-component membrane symmetry and relate it to the stability of black lipid membranes formed with different substrates [52]. Due to the weak nonlinear optical response in these experiments, recording times are more than 20 min per image. Since structural changes occur on much shorter time scales, no dynamic information has been obtained.

The above methods have greatly advanced membrane research, but have so far ignored the hydrating water, without which membranes cannot exist [178]. Recently, we demonstrated high-throughput wide-field SH imaging [140, 88] where we improved throughput of an SH microscope by a factor of $\sim 5,000$ compared with a confocal scanning microscope [88] enabling the measurement of interfacial water that was oriented by the presence of surface charges inside a glass microcapillary. If high-throughput wide-field SH imaging were to be applied to lipid membrane research, it would be possible to image the molecular structure of membrane-interacting water that is interrelated with hydration, the presence of local charges, ionization states, and membrane potentials. Such information, if obtained on a subsecond time scale, would provide a new pathway to image the dynamic molecular response of membranes and relate molecular structure to macroscopic function.

Here, we show that wide-field high-throughput SH imaging can indeed be used to label-free image the water molecules in the hydration shells of charged membranes. As hydrating water molecules are oriented by the ionic groups in the lipid head-groups of charged lipids through charge-dipole interactions, they can emit SH photons. We use a series of experiments based on changing the membrane composition, changing the ionic content of the aqueous phase adjacent to both membrane leaflets, and the pH of the solution to demonstrate that the hydrating water can be used to image membrane

structure. We then SH image domain diffusion on millisecond time scales in cholesterol (Chol)-rich freestanding lipid membranes by means of the water contrast and show that the diffusion times of whole domains compare well to time scales measured with fluorescence microscopy. Finally, we use the second-order optical response of water to measure the membrane potential and changes therein as a function of an external bias. While the average potential follows the quadratic dependence on an external bias, extractable from nonlinear optical theory, individual images show dynamic spatiotemporal fluctuations on the order of 100 mV.

4.2 Materials and Methods

4.2.1 Chemicals and lipids

DOPC, DPPC, DPPS, DPhPC, DPhPS, cholesterol, TopFlour cholesterol, hexadecane ($C_{16}H_{34}$, 99.8%, Sigma-Aldrich), hexane (C_6H_{14} , Sigma-Aldrich, >99%), chloroform (Merck, >99.8%), hydrogen peroxide (30%, Reactolab SA), sulfuric acid (95-97%, ISO, Merck), KCl (99.999%, Aros), HEPES (ACS Reagent, Sigma-Aldrich) were used as received. The chemical structures of the lipids are shown in Fig. 2.8. All aqueous solutions were made with ultra-pure water (H_2O , Milli-Q UF plus, Millipore, Inc., electrical resistance of 18.2 M Ω cm). All aqueous solutions were filtered with 0.1 μ M Millex filters. The coverslips used in the imaging were pre-cleaned with piranha solution (1:3 - 30% H_2O_2 : 95-97% H_2SO_4) and thoroughly rinsed with ultrapure water.

4.2.2 Freestanding horizontal planar lipid bilayers

Freestanding horizontal planar lipid bilayers were formed by monolayer apposition, following the Montal-Mueller technique (see Chapter 2.2 for details).

4.2.3 Imaging conditions and data analysis

The optical setup was characterized in detail in Chapter 2.1. The average power at the sample was set to 100 mW to 120 mW (Fig. 4.1 and Fig. 4.2) and 200 mW to 240 mW (Fig. 4.3D) for each arm. The SH photons were imaged with a 50 \times objective lens (Plan Apo NIR HR Infinity-Corrected Objective, 0.65 NA; Mitutoyo) (Fig. 4.1 and Fig. 4.2 and Fig. 4.3D, dark red curve) and a 20 \times objective (Plan Apo Infinity-Corrected Long WD Objective, 0.42 NA; Mitutoyo) (Fig. 4.3D, black curve). The acquisition times of the images were 560 ms (Fig. 4.1), 110 ms (Fig. 4.2A), 180 ms (Fig. 4.2B), and 2 s (Fig. 4.3D). The setup is illustrated in Fig. Fig. 2.1. The background hyper-Rayleigh scattering from the aqueous solution was subtracted from the data.

Domain tracking in Fig. 2C was done using the ImageJ TrackMate plugin. The images were first thresholded using the mean and standard deviation of the stack histogram of the sequence of images. The following parameters from the ImageJ plugin were used for tracking: LoG (Laplacian of Gaussian) detector; estimated blob size: 5 μ m; minimum blob diameter: 2.5 μ m; simple linear assignment problem tracker; linking max distance: 7.5 μ m; gap-closing maximum distance: 7.5 μ m; and gap-closing maximum frame gap: 3. Trajectories with the most number of steps were selected for calculation of MSD curves. The MSD curve used for linear fitting is less than 20% of the total number of steps.

4.3 Results & Discussions

4.3.1 SH Imaging of Membrane Hydration

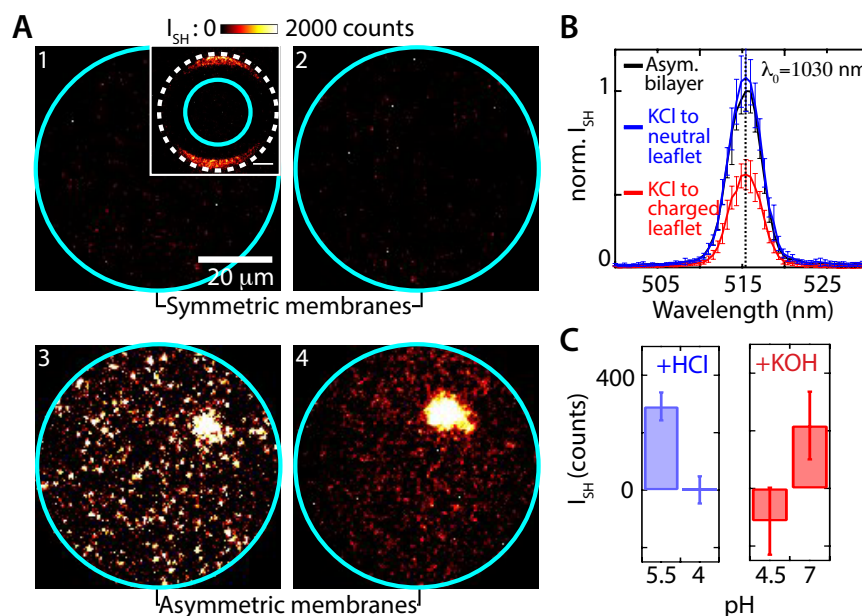


Figure 4.1 – SH imaging of membrane hydration. (A) SH images (20 frames, 560 ms each; magnification: 50 \times , NA = 0.65) of a symmetric membrane composed of (1) 75:25 mol % DOPC:Chol, and (2) 37.5:37.5:25 mol % DPPC:DOPC:Chol, and an asymmetric membrane composed of 37.5:37.5:25 mol % DPPS; DOPC:Chol (top leaflet) and 37.5:37.5:25 mol % DPPC:DOPC:Chol (bottom leaflet) (3) single frame, and (4) average of 20 frames. Inset in A shows the SH response of the Teflon film where the aperture that contains the bilayer is indicated by the white dashed circle. Analyses are performed only on the central part of the bilayer (cyan circle) as shown in 1–4. The images are collected with all beams P-polarized. (B) SH spectra of an asymmetric membrane composed of 70:30 mol % DPhPC:DPhPS (top leaflet) and DPhPC (bottom leaflet), black trace, and after addition of 0.5 mM of KCl to the bottom chamber containing the neutral leaflet [DPhPC + (KCl) $_{aq}$, blue], or the top chamber containing the charged leaflet [DPhPC:DPhPS + (KCl) $_{aq}$, red]. (C) Average SH intensity of an asymmetric DPhPS (top leaflet)/DPhPC (bottom leaflet) membrane before (pH = 5.5) and after (pH \approx 4) addition of (HCl) $_{aq}$ (blue) to the top compartment. Starting at pH = 4.5 and adding (KOH) $_{aq}$ to reach a pH-neutral solution increases the intensity. SH scattering images of a 100- μM KCl solution were subtracted from the raw images. The error bars represent the SDs from 20 spectra (B) or images (C).

Freestanding horizontal planar lipid bilayers are formed in an aperture of a thin Teflon film by the apposition of lipid monolayers formed on two different air/water interfaces [148, 146, 16]. The presence of a bilayer inside a \sim 80- to 120- μm -sized circular aperture in a 25- μm -thick Teflon film is confirmed with white-light imaging and electrical recordings (Fig. 4.1A and Fig. 2.13). The appearance of Newton diffraction rings and the measured specific capacitance (C_m) and specific resistance (R_m) of the membrane ($C_m > 0.7 \mu\text{F}/\text{cm}^2$, $R_m \approx 10^8 \Omega\cdot\text{cm}^2$, Fig. 1A) agree well with literature values [49, 16, 146]. Compositional transleaflet asymmetry is confirmed by capacitance minimization measurements [16, 18], that are sensitive to differences in surface charge density between the leaflets, see Fig. 4.4, Appendix, section 4.5.1 and Chapter 2.3.1 for details.

The horizontally mounted membranes are sandwiched between pH-neutral aqueous 0.1-mM KCl

solutions and are imaged with a medium repetition rate wide-field SH microscope [140] that employs a counterpropagating double-beam geometry (Fig. 2.1). Images are recorded with a numerical aperture (NA) of 0.65 or 0.42, and the SH photons are detected in the phase-matched direction, perpendicular to the membrane position. The polarization combination of the two incoming 1,030-nm, 190-fs, 200-kHz pulses and the emitted 515-nm intensity is controllable. The transverse resolution is 430 nm. For more information on the imaging throughput of the setup, see ref. [140] and Chapter 2.1.5 for details. Figure 4.1A shows SH images of the central part of several membranes: Fig. 4.1A, 1 shows a symmetric membrane composed of 75:25 mol % DOPC and Chol, Fig. 4.1A, 2 shows a symmetric membrane composed of 37.5:37.5:25 mol % DPPC, DOPC, and Chol in which domains of a more ordered phase composed of primarily saturated acyl chain lipids are formed within a more liquid phase consisting of primarily unsaturated lipids, and 4.1A, 3 and 4 shows an asymmetric membrane composed of 37.5:37.5:25 mol % DPPS, DOPC, and Chol (top leaflet) and 37.5:37.5:25 mol % DPPC, DOPC, and Chol (bottom leaflet) that also displays domain formation. The acquisition time for each image was 560 ms, and Fig. 4.1A, 4 represents an average of 20 frames. The images were collected with all beams P-polarized. Figure 4.1A, 1, *Inset* displays an SH image recorded from the Teflon film, where the aperture that contains the bilayer is indicated by the white dashed circle. It can be seen that SH photons appear from the edge of the Teflon aperture but not from the center of the membrane. The absence of SH photons from the center of a symmetric bilayer arises from the fact that oppositely oriented polar molecules do not emit SH photons [within the dipole approximation [73]]. This result agrees with the images obtained by Ries et al. [52]. As the membrane is ~ 5 nm thick in the center of the aperture, while the Teflon film is 25 μm thick, there is only a bilayer membrane inside the cyan circle. Outside the cyan circle, but still inside the white dashed circle (the aperture), there is a mixture of hexadecane oil covered with lipids. This curved membrane around the edges of the Teflon film emits SH photons, because, with increasing distance between opposing curved leaflets, there is not anymore destructive interference between the emitted SH photons. This interference process is comparable to observing the emission of SH photons from nanoscopic particles in solution [11]. The SH emission from the curved water/lipid/oil edges of the film becomes brighter for larger distances between the opposing leaflets. The Teflon ring itself emits a weak two-photon fluorescence.

Comparing the center of symmetric and asymmetric membranes, Fig. 4.1A shows that only the asymmetric membrane generates a clear SH bilayer contrast. Note that the only difference in composition between Fig. 4.1A, 2 and Fig. 4.1A, 3 and 4 is that the charge-neutral DPPC in one leaflet is replaced with charged DPPS. This results in the appearance of μm size domains rich in DPPS lipids. The polarization and symmetry selection rules [73, 11] for nonresonant SH generation dictate that centrosymmetric systems (such as an isotropic liquid) will not generate coherent SH photons. Orientational ordering of asymmetric molecules along the surface normal are responsible for the contrast, and will be most pronounced in the PPP polarization combination [73]. This is essentially what we observe in Fig. 4.1A: only the asymmetric bilayer generates a SH image, while the symmetric bilayers do not, in agreement with literature [50, 159]. Figure 4.5 (see Appendix, section 4.5.2) shows that the nonzero polarization combinations are PPP and SSP, with the first (second and third) letter describing the outgoing (incoming) beam(s). These combinations are to be expected for an azimuthally isotropic interface in contact with centrosymmetric media [73]. This behavior is distinctly different from fluorescence.

Figure 4.1B displays the SH spectrum (black) obtained from an asymmetric membrane composed of DPhPS (top leaflet) and DPhPC (bottom leaflet), which confirms that, indeed, SH light is detected. Candidates for the emission of SH photons are all noncentrosymmetrically structured molecular groups [73, 179], that is, lipids or water. Taking into account the number density difference between water

Chapter 4. Label-free and charge-sensitive dynamic imaging of lipid membrane hydration on millisecond time scales

and lipids and previous nonresonant SH scattering studies of liposomes [78, 79], it is likely that the dominant contribution to the SH intensity will be from water. To test this hypothesis, we added 0.5 mM KCl to the solution. Adding KCl changes the ion distribution inside the interfacial electric double layer and modifies the surface potential [19]. This modification alters the number of noncentrosymmetrically distributed water molecules that generate SH light [77], but not the number of noncentrosymmetrically distributed lipids. Figure 4.1B shows that adding KCl to the neutral side of the membrane leads to a negligible difference within error of the measurement in the SH intensity (blue spectrum) [180]. Increasing the KCl concentration on the side with the charged leaflet, however, reduces the SH intensity (red spectrum). Thus, the SH response originates primarily from the hydrating water in the electric double layer that is associated with the charged lipid head groups. This interpretation is further confirmed by protonating/deprotonating the asymmetrically distributed DPhPS lipids ($pK_a \approx 5.5$ to 6, at low ionic strength) [173, 181] as shown in Fig. 4.1C. Starting with a bilayer in contact with a pH = 5.5 solution, the ionic strength (I) is 100 μM , which has ~ 20 to 50% of the PS groups charge neutral and the other part negatively charged; adding $(\text{HCl})_{aq}$ ($I \approx 130 \mu\text{M}$) leads to a removal of the surface charges and results in a vanishing SH intensity. On the other hand, starting with a membrane in contact with an acidic solution (pH = 4.5, $I = 100 \mu\text{M}$, all PS groups charge neutral) increasing the pH to ~ 7 ($I \approx 130 \mu\text{M}$) by adding $(\text{KOH})_{aq}$ ionizes most of the PS groups and results in a sharp increase in the SH intensity, which is indeed the case.

Having determined that the hydrating water associated with charged lipids is responsible for the SH emission of asymmetric lipid bilayers, we proceed to use the orientational order of water around charged head groups as a label-free and in situ probe of membrane dynamics.

4.3.2 SH Imaging of Membrane Structure and Dynamics

To image membrane dynamics in real time, an asymmetric membrane of the same composition as used in Fig. 4.1A, 3 is formed at elevated temperatures ($>60 \text{ }^\circ\text{C}$) which is then cooled down to room temperature. Ternary mixtures of lipids with different transition temperature, degree of saturation, and chain length (e.g., DPPS vs. DOPC), mixed with Chol, phase separate into liquid-ordered (rich in DPPS with Chol) and liquid-disordered (rich in DOPC) phases [8, 4, 5]. To verify phase separation, we labeled the charged leaflet (DPPS/ DOPC/Chol) with TopFluor Chol that is known to partition into the Chol-rich hydrophobic phase [182, 183] and imaged the membrane two-photon excited fluorescence with 110-ms acquisition time. Figure 4.2A shows $\sim 3\text{-}\mu\text{m}$ -diameter domains (Fig. 4.2C, orange) of a liquid-ordered DPPS-rich phase. Mean square displacement (MSD) traces (orange) are shown in Fig. 4.2D, with a diffusion constant of $D = 0.19 \pm 0.01 \mu\text{m}^2/\text{s}$, in agreement with literature [4]. Figure 4.2B shows an SH image recorded with 180-ms acquisition time of a membrane with the same composition, but now following the hydrating water around the charged head groups of DPPS, label-free. Domains with a similar size (Fig. 4.2C) and diffusion speed (Fig. 4.2D, green, $D = 0.23 \pm 0.06 \mu\text{m}^2/\text{s}$) are observed. Corresponding movies are shown online in PNAS website (<http://www.pnas.org/content/early/2018/03/27/1719347115/tab-figures-data>). Although both imaging modalities measure a different observable, the presence of fluorophores attached to modified Chol inserted in the condensed phase vs. the hydrating water in contact with the head groups of charged DPPS lipids in the condensed phase, the similarity between the fluorescently labeled membrane images and the nonlabeled membrane SH images suggests that it is indeed possible to probe membrane dynamics by means of the hydration shells of the charged lipids.

Having shown that membrane hydration can be tracked dynamically and label-free, we proceed

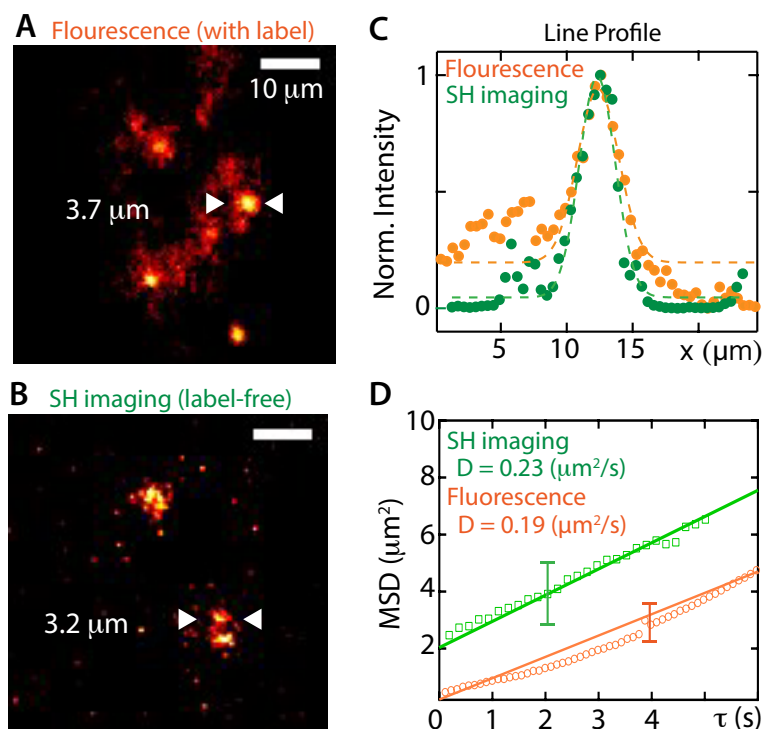


Figure 4.2 – SH imaging of water around liquid-ordered domains of charged lipids. (A) Fluorescence image of an asymmetric membrane composed of 37.5:37.5:25 mol % DPPS/DOPC/Chol + TopFluor (top) and 37.5:37.5:25 mol % DPPC/DOPC/Chol (bottom). (B) SH image of a membrane made with the same composition and asymmetry but now label-free. (Scale bar, 10 μm .) The arrows in A and B point to the positions where the line profiles were obtained to extract the domain size. Both images show phase separation, leading to DPPS and Chol-rich domains of similar size. (C) MSD as a function of delay time (τ) comparing label-free SH imaging with TopFluor labeled imaging. The calculated diffusion coefficients are comparable. SH scattering images of a 100- μM KCl solution were subtracted from the raw SH images. Symbols are experimental data and lines are linear fits.

to use the charge-induced orientational order of water molecules to derive membrane potentials. Changes in the membrane potential are induced by external stimuli.

4.3.3 SH Imaging of Membrane Potential

The electrical activity in membranes underlies a wide variety of chemical and physical processes in cells: the contraction of muscle cells, the communication of neurons, and transport functions all depend on membrane potentials [3]. To date, lipid bilayer membrane potentials cannot be imaged directly and noninvasively, and the method below provides a proof of the possibility to do this label-free and in real time. SH measurements and theoretical considerations have shown that the SH intensity of an interface depends on the surface potential (Φ_0) via $I(2\omega) \approx |\chi_s^{(2)} + \chi^{(3)'} \Phi_0|^2$ [77, 184], where $\chi_s^{(2)}$ is the surface second-order susceptibility and $\chi^{(3)'}$ is an effective third-order susceptibility of the aqueous phase (see refs. [78] and [185] for more details). For our imaging experiment, there are two oppositely

Chapter 4. Label-free and charge-sensitive dynamic imaging of lipid membrane hydration on millisecond time scales

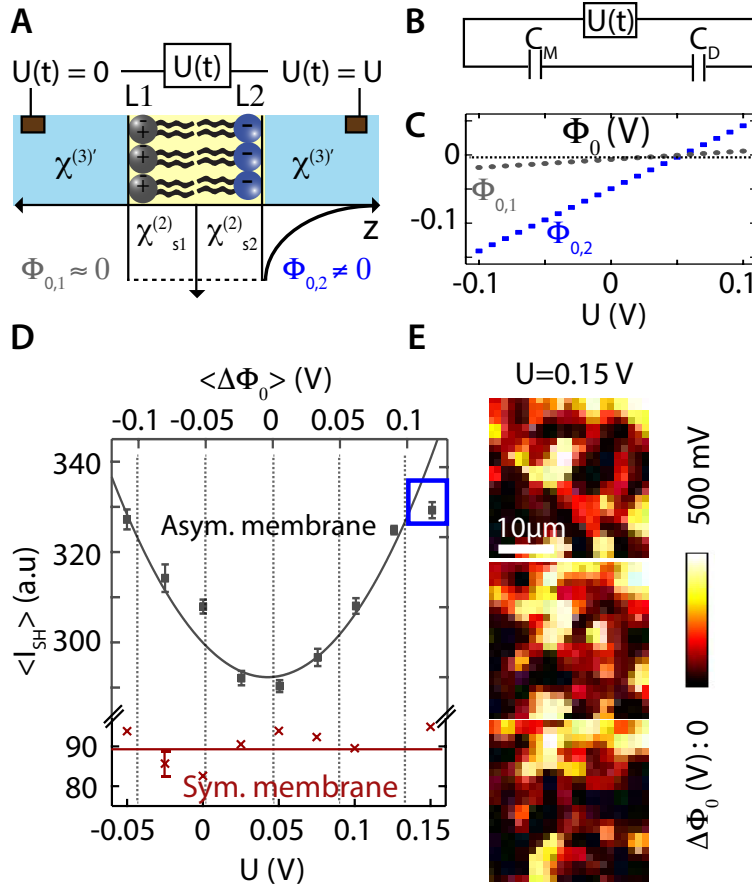


Figure 4.3 – Voltage-sensitive SH imaging of the changes in membrane surface potential. (A) Illustration of the membrane with one neutral (L1) and one charged (L2) leaflet, the susceptibility ($\chi_s^{(2)}$ and $\chi_s^{(3)}$), and surface potential Φ_0 . (B) Simplified model of a membrane with capacitance C_M in series with a double layer of capacitance C_D . (C) One-dimensional COMSOL simulation of the shift in surface potential as a function of an applied bias for an asymmetric membrane (Numerical Computations for details, 4.6, Materials and Methods); $\Phi_{0,1}/\Phi_{0,2}$ shows the linear response of the surface potential of the neutral and charged leaflet as a function of external bias (U). (D) Spatially averaged SH intensities per pixel as a function of an applied bias (U) for an asymmetric membrane composed of 70:30 mol % of DPhPC:DPhPS (top leaflet) and DPhPC (bottom leaflet) (black data), and a symmetric membrane composed of DPhPC (dark red data). The top axis shows the average surface potential changes for the corresponding applied bias, with the coloring corresponding to the average surface potential changes. The average intensity values were computed over a 25- μm -diameter aperture. SH scattering images of a 100- μM KCl solution were subtracted from the raw images. The error bars represent the SD of the mean from 20 images. (E) Surface potential maps for three subsequent frames, 2-s acquisition time, with an external bias of 150 mV. The maps are taken from the central part of the membrane 23 $\mu\text{m} \times 23 \mu\text{m}$ in size.

oriented membrane interfaces i , that each have a surface potential $\Phi_0(x, y)$ (Fig. 4.3A, top) resulting in

$$I(2\omega, x, y) \approx I(\omega, x, y)^2 |\chi_{s1}^{(2)}(x, y) - \chi_{s2}^{(2)}(x, y) + \chi^{(3)'} f_3(\Phi_{0,1}(x, y) - \Phi_{0,2}(x, y))|^2 \quad (4.1)$$

where f_3 is an interference term which has the form factor $f_3 = \kappa/\kappa - i\Delta k_z$, containing Δk_z as the wave vector mismatch ($\Delta k_z = |k_{1z} + k_{2z} - k_{0z}| = k_{1z} + k_{2z} - k_{0z}$, and $k_{1,2}$ as the incoming wave vectors and k_0 as the outgoing wave vector), and κ as the inverse Debye length. This term describes interference effects within the electric double layer. For the transmission experiment employed here, $f_3 \rightarrow 1$ [185]. Figure 4.3A shows a schematic of an asymmetric membrane subject to an external bias U . The effect of an external bias U can be simplified by treating the membrane as a capacitor (C_m) in series with the electric double layer approximated as a capacitor (C_D) with a plate spacing equal to the Debye length ($1/\kappa$) as shown in Fig. 4.3B. The specific capacitance ($C_D = \epsilon_0\epsilon_r\kappa$) of the double layer is then $\approx 2.3 \mu\text{F}/\text{cm}^2$ using $\epsilon_r = 80$, and $1/\kappa = 30.3 \text{ nm}$ (corresponding to $I = 100 \mu\text{M}$). Applying an external bias U to the membrane ($C_m = 0.7 \mu\text{F}/\text{cm}^2$) in series with the double layer (Fig. 4.3B), 23% of the potential drop occurs in the double layer. This modifies the ion concentration near the membrane, and changes the surface potential (Fig. 4.3C), such that $\Delta\Phi_0(U) = \Delta\Phi_{0,ini} + \beta U$ with β a constant of proportionality and $\Delta\Phi_{0,ini}$ the initial surface potential difference at zero external bias ($U = 0$). Figure 4.3C shows an estimate of the proportionality relation between Φ_0 and U derived from a COMSOL simulation (COMSOL Multiphysics software) for an asymmetric bilayer (see 4.6, Appendix, section 4.5.3). The surface potential of each leaflet changes as a function of bias, with the majority of the change occurring in the charged leaflet. For a symmetric zwitterionic membrane, from 4.1, we have $\chi_{s1}^{(2)} = \chi_{s2}^{(2)}$ and $\Phi_{0,1} = \Phi_{0,2} = 0$, resulting in a vanishing response (Fig. 4.1B, 1 and Fig. 4.3D, dark red). For an asymmetric membrane with charge neutral leaflet (L1, $\Phi_{0,1} \approx 0$) and charged leaflet (L2, $\Phi_{0,2} \neq 0$) (Fig. 4.3D, black), we expect a quadratic dependence of the SH intensity on $\Delta\Phi_0 = \Phi_{0,1} - \Phi_{0,2}$ and thus also on U . When the bias (U) compensates the initial surface potential difference, i.e., $\Delta\Phi_{0,ini} \approx -\beta U$, $\Delta\Phi_0 \approx 0$, we expect a minimum in the induced surface potential difference and thus a minimum in the recorded SH intensity. Figure 4.3D shows the average recorded SH intensity per pixel as a function of bias for a charge-neutral DPhPC symmetric bilayer (dark red), and an asymmetric charged bilayer composed of a 70:30 mol % mixture of DPhPC:DPhPS lipids on the top leaflet and DPhPC on the bottom leaflet (Fig. 4.3D, black). A quadratic dependence of the SH intensity on the applied bias U is observed for the asymmetric membrane but not for the symmetric membrane, consistent with 4.1. To obtain the surface potential changes induced by the bias, the data were fitted using 4.1 with $\chi^{(3)'} = -10.3 \times 10^{-22} \text{ m}^2/\text{V}^2$ as for DOPS and DOPC liposomes from ref. [78], $\chi_{s1}^{(2)} - \chi_{s2}^{(2)} = 5 \times 10 \text{ m/V}$ corresponding to 3% of the value of $\chi_s^{(2)}$ from a monolayer membrane [78], and the average surface potential difference $\langle\Delta\Phi_0(x, y)\rangle$ as a variable. The retrieved values for $\langle\Delta\Phi_0(x, y)\rangle$ are plotted on the top axis, with the initial surface potential difference $\Delta\Phi_0$ around -50 mV. This value corresponds to 0.6% of ionized lipids (Numerical Computations) and is consistent with the theory of charge condensation [79, 186]. Figure 3E shows snapshots of the membrane potential recorded for three subsequent frames, 2 s in acquisition time, with an external bias of 150 mV. It can be seen that fluctuations across the membrane occur that change from frame to frame. Although the average membrane potential of the 20-frame data stack is 115 mV, fluctuations as large as $\sim 100 \text{ mV}$ are observed. The fluctuations suggest a variable degree of ionization from 0 to $\sim 6\%$ in the images of Fig. 4.3E (using the values from the COMSOL simulation).

It is thus possible to optically determine the membrane surface potential label-free and to track spatiotemporal changes in it as a function of an external bias. The fluctuations imply that membranes are very dynamic, not only in their structure but also in their membrane potential landscape. The fluctuations observed in the membrane potential can arise from the association/dissociation dynamics of surface charges similar to the observed heterogeneous association rates on the surface of silica glass [88]. This spatial and temporal heterogeneity could have important consequences for membrane function, mechanical stability, and protein/pore distributions.

4.4 Summary and Conclusions

In summary, we have shown, in a series of experiments on freestanding lipid membranes involving symmetric and asymmetric lipid membranes, and changes in the ionic and pH content of adjacent solutions, that hydrating water can be SH imaged on subsecond time scales. This hydrating water has a nonrandom orientation, as it is oriented by the charge-dipole interactions between charged lipid head groups and water dipoles. We demonstrate that this contrast mechanism can be used to probe domain diffusion of DPPS-rich domains. In addition, we used the water response to compute the electrostatic membrane potential, and map its dependence on an externally applied field. Although the average membrane potential follows the quadratic dependence on external bias that is modeled by nonlinear optical theory, individual images show dynamic spatiotemporal fluctuations on the order of ~ 100 mV. These fluctuations illustrate the dynamic link between the aqueous environment and the lipid membrane that is often forgotten.

This contrast mechanism for label-free SH imaging of membranes can be used to acquire molecular-level understanding of membranes that are due to a number of important processes such as specific ion interactions, membrane (interleaflet) structuring and dynamics, membrane fusion, charge-dependent protein activity, ion pumps/ pore structure and activity, surface acid/base reactions, and dynamics of membrane potentials. The imaging method is directly applicable to live neurons, without the need to physically patch the cells, thus possibly providing a future noninvasive and clinically viable method of mapping membrane potentials. The connection between the molecular response of the hydrating water and the structural features present in the images provides a unique connection between molecular-level processes involving water and macroscopic observables.

4.5 Appendix

4.5.1 Verification of Transmembrane Asymmetry by Capacitance Minimization

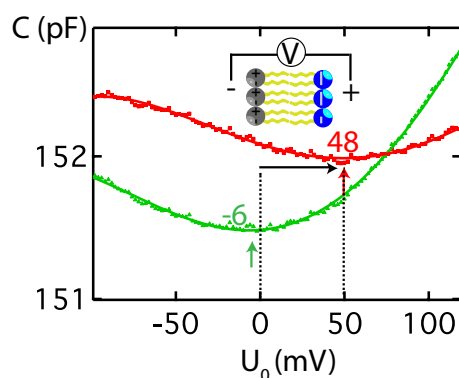


Figure 4.4 – Capacitance as a function of applied bias U_0 . The minimum of the capacitance for a symmetric membrane (green) composed of 75:25 mol % DOPC: chol and an anionic asymmetric membrane (red) composed of 37.5:37.5:25 mol % DPPS:DOPC:Chol (top leaflet) and 37.5:37.5:25 mol % DPPC:DOPC:Chol (bottom leaflet) shifts from $U_0 = -6$ mV to $U_0 = 48$ mV.

To confirm the compositional transleaflet asymmetry of the membrane, we measured the membrane capacitance as a function of applied U_0 potential and obtained the U_0 value where the capacitance has a minimum, as described in Chapter 2.2.3. This electrical approach was used to estimate

the surface charge density difference between adjacent lipid leaflets [16, 187, 188, 17, 18]. Figure 4.4 displays the measured capacitance as function of applied dc bias (U_0) for two different membranes, one zwitterionic, symmetric membrane (green) composed of 75:35 mol % DOPC: chol and an anionic asymmetric membrane (red) composed of 37.5:37.5:25 mol % DPPS:DOPC:Chol (top leaflet) and 37.5:37.5:25 mol % DPPC:DOPC:Chol (bottom leaflet). It can be seen that the green curve has a minimum in the capacitance at $U_0 = -6$ mV. The red curve displays a minimum at $U_0 = 48$ mV. This is in agreement with expectations, as the symmetric bilayer should not display any charge difference between the leaflets. The other bilayer, being asymmetric, will have some charge difference and therefore will require a compensating bias potential to achieve a minimum in the capacitance [16]. The reason is that a charged bilayer experiences an electrostatic force in the normal direction, resulting in a thinner bilayer with a bigger capacitance (since $C = \epsilon\epsilon_0 A/d$ with A as the area and d as the leaflet separation). When the bias equals the membrane potential difference between the leaflets, this force will vanish, leading to a thicker membrane and a smaller (minimum) capacitance [187, 17, 189, 163].

4.5.2 Nonvanishing Polarization Combinations

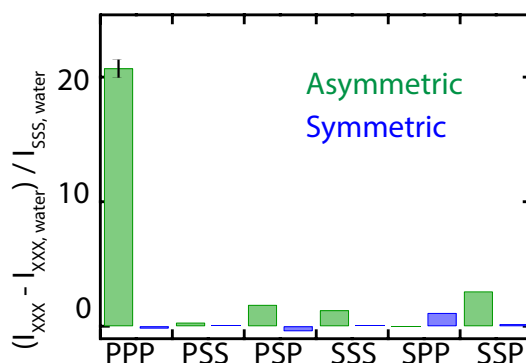


Figure 4.5 – Non-vanishing polarization combinations. Normalized integrated intensity of an asymmetric membrane (green) composed of 50:50 mol % DPhPC: DPhPS (top) and DPhPC (bottom) and a symmetric membrane (blue) composed of DPhPC for different polarization combinations. Error bars consider the standard of 20 images from both the membrane and the solution.

SH generation arises from both oppositely oriented leaflets (Fig. 4.3). The emitted SH field is the superposition of the SH field emitted from both interfaces (Eq. 4.1). Because of the opposite orientation, the emitted SH electromagnetic waves are 180° phase shifted, leading to a near cancellation of the $\chi_s^{(2)}$ term in Eq. 4.1. The emitted response is therefore dominated by the $\chi^{(3)'}$ contribution [78]. A charge-neutral symmetric membrane that has $\Phi_{0,1} = \Phi_{0,2} \approx 0$ is therefore expected to have a vanishing SH response in all polarization directions. A membrane with an asymmetric charge-neutral leaflet (1, $\Phi_{0,1} \approx 0$) and charged leaflet (2, $\Phi_{0,2} \neq 0$) will have a response in polarization combinations that are dominated by the nonvanishing elements of $\chi^{(3)'}$, which are PPPP, SPSP, SSPP, and PSSP. The last index refers to the interfacial electrostatic field (directed in the z direction, leading to a P-polarized contribution). We thus have PPP, SPS, SSP, and PSS as nonzero polarization combinations for the optical fields, with the first index referring to the SH beam and the last two referring to the incoming beams. The vanishing polarization combinations for the optical beams are SSS, SPP, PSP, and PPS [73]. To confirm that these selection rules are indeed met, we recorded SH images in different polarization combinations of a symmetric membrane composed of DPhPC and an asymmetric membrane composed of a DPhPS:DPhPC mixture in a 1:1 ratio (top leaflet) and DPhPC (bottom leaflet). Fig. 4.5 shows

Chapter 4. Label-free and charge-sensitive dynamic imaging of lipid membrane hydration on millisecond time scales

the integrated intensity over a 50- μm -diameter circular area of the symmetric (blue) and asymmetric (green) membrane. The intensity is normalized relative to the SH scattering of a 100- μM KCl solution at the same polarization combination, and divided by the SH response recorded in the SSS polarization combination, as in nonlinear light scattering [78]. It can be seen that only the asymmetric membrane yields SH responses above the noise level of our system. The nonvanishing polarization combinations are PPP and SSP, with PPP having a much higher intensity. That the SSP combination does not generate any detectable SH response indicates that $\chi_{zxzx}^{(3)'} + \chi_{zxxz}^{(3)'} > \chi_{zyyz}^{(3)'}$, that is, the dominant contribution here is $\chi_{zxzx}^{(3)'}$. The PSS combination vanishes because the outgoing field can only be detected along the x-y plane (Fig. 2.1). For the same reason, we cannot probe the elements $\chi_{zzzz}^{(3)'}$ and $\chi_{zxxz}^{(3)'}$. It can also be seen that the SSS, SPP, and PSP polarization combinations vanish, in agreement with expectations.

4.5.3 Numerical Computations.

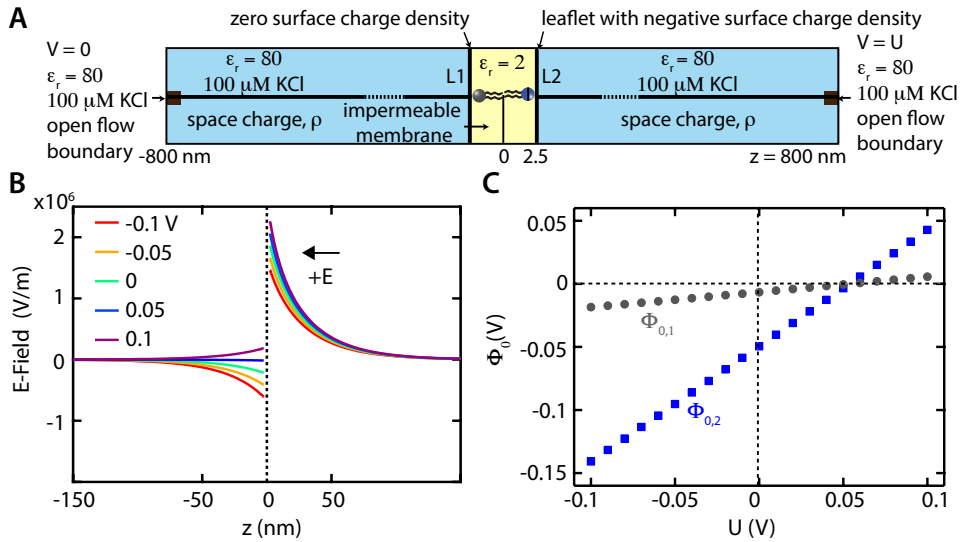


Figure 4.6 – COMSOL simulation of an asymmetric membrane. (A) One-dimensional geometry and boundary conditions of the simulation with the membrane located at $z = 0$ nm, the leaflets at $z = \pm 2.5$ nm, and the ground and signal electrodes located 800 nm away from the membrane. The membrane (with relative permeability of $\epsilon_r = 2$) was immersed in a KCl solution with $\epsilon_r = 80$. (B) Electrostatic field as a function of distance from the membrane for different external biases. The arrow points to the direction of positive electric field. The dashed line refers to the location of the membrane. (C) Surface potential shift induced by an external bias derived from B. The dashed lines are guide to the eye.

To estimate the dependence of the surface potentials $\Phi_{0,1}$ and $\Phi_{0,2}$ on the external bias U , we performed a numerical computation using the COMSOL 5.2 package. The membrane was represented by a 5-nm-thick impermeable slab, centered at $z = 0$ with a dielectric constant of $\epsilon_r = 2$ and an asymmetric charge density on each leaflet. Leaflets L1 and L2 are located at $z = 2.5$ nm and $z = -2.5$ nm, respectively, and the reservoir (including the electrodes) is placed 800 nm away from the membrane. The reservoir represents the boundary condition where the electric potential and the concentration of ions are nearly constant. Figure 4.6A shows an illustration of the 1D geometry of the system. The surface charge density of the charge-neutral leaflet (L1) was set to zero, and the surface charge density of the charged leaflet (L2) was set to -1.47 mC/m², corresponding to $\sim 0.6\%$ of the lipids being ionized and 99.4% having a counterion in close proximity [79]. The electrode facing L1 was

grounded ($V = 0$ V), and the electrostatic potential of the electrode facing L2 ($V = U_0$) was varied from -100 mV to 100 mV in steps of 10 mV. The membrane is immersed in a 100- μ M KCl solution $\epsilon_r = 80$. The COMSOL package numerically solves the steady state Poisson and Nernst–Planck (PNP) equations. The PNP equations are:

$$J_i = -D_i \nabla c_i - \frac{D_i}{RT} z_i F c_i \nabla \phi(z) \quad (4.2)$$

$$\nabla^2 \phi(z) = -\frac{\rho(z)}{\epsilon_0 \epsilon_r} \quad (4.3)$$

$$\rho(z) = F \sum_i z_i c_i(z) \quad (4.4)$$

Eq. 4.2 relates the ion flux of species i (J_i) to the electric potential $\phi(z)$, that contains also the external bias as defined in the boundary conditions. The electrostatic potential $\phi(z)$ and charge density $\rho(z)$ are defined in Eqs. 4.3 and 4.4, respectively. F is the Faraday constant, R is the gas constant, T is the temperature, D_i is the diffusivity, c_i is the concentration, z_i is the valency of the i -th species, ϵ_0 is the vacuum permittivity and ϵ_r is the relative permittivity. The membrane is assumed to be impermeable to ions, and the boundary conditions are summarized in Fig. 4.6A. The electric potential, the electric field, the distribution of each charged species i , and, consequently, the charge density everywhere in the system are computed. Eqs. 4.2–4.4 were solved using a mesh with a normal size: The maximum element size was set to 5 nm, with a growth rate of 5%, except near the vicinity of the membrane where it is further refined. Here, the maximum element size was set to 0.005 nm with a growth rate of 10%. Figure 4.6B shows the simulated electrostatic field as a function of distance in the vicinity of the membrane for several external bias values. As the SH response is related quadratically to the number of oriented water molecules [77] and the number of oriented water molecules depends on the electrostatic field via a Boltzmann distribution [79], the SH response originates for ~ 90 to 99.4% from the charged leaflet. Note that this is a lower limit, as we have not explicitly included the presence of a Stern layer, which will increase the magnitude of electrostatic interfacial field dramatically. The change in surface potential (defined as the potential at the location of the leaflets, $z = \pm 2.5$ nm) can be obtained by fitting a double exponential to the electric field profile in Fig. 4.6B and integrating the result from $z = 2.5$ nm to $z \rightarrow \infty$, as $\Phi = -\int_{2.5}^{\infty} E \cdot dz = -\Phi(z = \infty) + \Phi_0$. The potential at the 2.5 surface (Φ_0) is then equal to the area under the curve of the E- field profile in Fig. 4.6B relative to the applied bias, $\Phi(z = \infty)$. The resulting values for the surface potential of each leaflet are plotted in Fig. 4.6C. It can be seen that the surface potential varies linearly with the external bias, as expected.

5 Divalent ions induce transient domains of interfacial ordered water in lipid membranes

Cell membranes are highly complex and diverse. However, the molecular level foundations of lipid membranes are currently understood on a mean-field level. Here, we demonstrate the importance of spatiotemporal fluctuations. We probed the interactions of divalent cations with water and negatively charged freestanding lipid bilayers using high throughput wide-field second harmonic microscopy. We found that divalent cation-membrane interactions result in the formation of short-lived micron-sized domains of orientationally ordered water. The SH intensity was converted into membrane potential, surface charge, free energy, and ion binding dissociation constant (K_D) maps. The ion-induced changes follow the order $Ca^{2+} > Ba^{2+} > Mg^{2+}$, for all four quantities and reach domain values of -368 mV, -1.7 mC/m², 28.6 kT and $2.7 \cdot 10^{-12}$ M, with K_D up to 4 orders of magnitude higher than expected. The transient electric field gradients across the membrane induce transient curvature, resulting in temporal and spatial surface tension variations.

This chapter is based on the author's journal article: **O. B. Tarun**, H. I. Okur, P. Rangamani, S. Roke. Submitted (2018).

5.1 Introduction

Cell membranes are in a constant state of structural flux [53, 46]. Lipid bilayer membranes provide a rich environment for the formation of diverse structures and environments. Membrane structuring is commonly described in terms of lipid segregation, and measured by probing the hydrophobic core of a membrane [62, 190, 191], or tagged lipids [4, 59, 5, 7, 6]. While this provides information about lipid-lipid interactions it largely ignores hydration, electrostatic and hydrogen bonding interactions and the influence of the electric double layer. These interactions play an important role in membrane function [192, 193] but have not been quantified in living cells, nor in realistic bilayer systems such as liposomes or freestanding lipid bilayers. As an example, ion-specific effects that involve the complex interaction between cations, surface charges, polar and hydrophobic groups are important in signaling through ion-specific channels in synapses [194, 195, 103, 196], the folding of proteins [95, 96], the formation of secondary structures [97, 98], and the induction of cell death by the presence of charged phosphatidylserine (PS) lipids [90]. How these processes work on a molecular level is presently not fully understood. Although molecular level experiments on model planar air/lipid/water monolayer systems [111, 110, 14, 197], and supported bilayer – protein systems [97, 12] have revealed ingredients of the already complex molecular behavior that consists of different types of interactions between ion, lipids, proteins, and water molecules, they do not take into account spatial and temporal dynamic behavior that is clearly important for the bilayer membranes of cells. An important question, therefore, is whether the behavior of membranes can be captured by averaging spatial and temporal fluctuations in the system (assumptions that are necessarily made by technical limitations and result in the application of mean-field model descriptions).

Here, we probed the interactions of divalent cations (Ca^{2+} , Mg^{2+} , Ba^{2+} , at physiologically relevant concentrations), with water and negatively charged freestanding lipid bilayers using high throughput wide-field second harmonic microscopy. We found that divalent cation- membrane interactions result in the formation of short-lived (<500 ms) and micron-sized ($\sim 1.5 \mu\text{m}$) domains of orientationally ordered water. The SH intensity was converted into membrane potential, surface charge density, membrane hydration free energy, and ion binding dissociation constant (K_D) maps. The ion-induced changes follow the order $\text{Ca}^{2+} > \text{Ba}^{2+} > \text{Mg}^{2+}$, for all four quantities and reach domain values of -368 mV, -1.7 mC/m², 28.6 kT, and $2.7 \cdot 10^{-12}$ M, with K_D deviating up to 4 orders of magnitude from current values based on a mean-field interpretation. Additionally, the transient electric field gradients across the membrane lead to transient curvature, resulting in temporal and spatial variations in the mechanical properties for the membrane.

5.2 Materials and Methods

5.2.1 Chemicals and lipids

DPhPC, DPhPA in power form (>99%), hexadecane ($\text{C}_{16}\text{H}_{34}$, 99.8%, Sigma-Aldrich), hexane (C_6H_{14} , Sigma-Aldrich, >99%), chloroform (Merck, >99.8%), hydrogen peroxide (30%, Reactolab SA), sulfuric acid (95-97%, ISO, Merck), KCl (99.999%, Aros), CaCl_2 (99.999%), MgCl_2 (99.99%) and BaCl_2 (99.999%) (Sigma-Aldrich) were used as received. All aqueous solutions were made with ultra-pure water (H_2O , Milli-Q UF plus, Millipore, Inc., electrical resistance of 18.2 M Ω cm). All aqueous solutions were filtered with 0.1 μm Millex filters. The coverslips used in the imaging were pre-cleaned with piranha solution (1:3 - 30% H_2O_2 : 95-97% H_2SO_4) and thoroughly rinsed with ultrapure water.

5.2.2 Second harmonic (SH) imaging.

The optical setup was characterized in detail in Chapter 2.1. The images were collected with a 50x objective lens (Mitutoyo Plan Apo NIR HR Infinity-Corrected Objective, 0.65 NA). All images were recorded with the beams polarized parallel to the plane of incidence (P). The acquisition time of the images was 560 ms.

5.3 Results & Discussions

5.3.1 Spatiotemporal ion-specific effects

Freestanding horizontal planar lipid membranes were formed following the Montal-Mueller method [49, 149]. Two separate lipid monolayers at the air/water interface were apposed in an 80-120- μm -sized circular aperture in a 25- μm thick Teflon film. The horizontally mounted membrane was imaged with a medium repetition rate, wide field nonlinear SH microscope. Two counter-propagating 190 fs, 1032 nm, 200 kHz pulsed beams with an opening angle of 45deg illuminate the membrane interface, such that phase matched SH photons are emitted and recorded along the membrane surface normal (Fig. 5.1A, see Refs. [140, 80] and Chapter 2.1 for details). Figure 5.1B shows a SH image recorded of a symmetric lipid bilayer of identical leaflets composed of 70:30 mol % 1,2-diphytanoyl-sn-glycero-3-phosphocholine (DPhPC) and 1,2-diphytanoyl-sn-glycero-3-phosphate (DPhPA). Figure 5.1C shows a SH image recorded of an asymmetric lipid bilayer composed of a DPhPC leaflet (bottom leaflet) and a 70:30 mole % mixture of DPhPC:DPhPA (top leaflet). No coherent SH photons are generated by the symmetric bilayer while the asymmetric bilayer does generate a SH response. As we showed in Ref. [80], the SH response arises from the charge-dipole interaction between the charged head groups and the dipolar water molecules, which creates a non-random orientational distribution of water dipoles along the surface normal. Figures 5.1D-5.1F show SH images of the same symmetric DPhPC:DPhPA bilayer system as in Fig. 5.1B, but instead of using an aqueous KCl solution in contact with both leaflets, we replaced the solution adjacent to the top leaflet with $(\text{CaCl}_2)_{aq}$, $(\text{BaCl}_2)_{aq}$ and $(\text{MgCl}_2)_{aq}$ solutions of the same ionic strength.

Adding Ca^{2+} , Ba^{2+} or Mg^{2+} to the aqueous phase results in a spatially fragmented SH response. Ca^{2+} , Ba^{2+} , and Mg^{2+} are known to interact specifically with negatively charged lipid head groups [111, 110, 198, 199, 107] forming lipid-cation complexes. The water in contact with such neutral cation-lipid clusters has a negligible orientational ordering along the interfacial normal [159]. Membrane water in contact with free head group charges, on the other hand, does exhibit an orientational order along the interfacial normal. When both structures are present on opposite sides of the membrane, centrosymmetry is broken, resulting in domains of bright SH intensity. Fig. 5.1 shows that the number of domains and the relative intensity decreases in the order $\text{Ca}^{2+} > \text{Ba}^{2+} > \text{Mg}^{2+}$.

To analyze the properties of these domains in more detail we turn to single frame analysis (560 ms/frame) and analyze the spatial (Fig. 5.2A,B) and temporal (Fig. 5.2C) correlations between the domains in a single leaflet, and the coupling between domains in both leaflets (Fig. 5.2D). The spatiotemporal evolution of the domains on a single leaflet is shown in Fig. 5.2A where three consecutive time frames are shown (raw data), each recorded with a 560 ms integration time. Figure 5.2B shows the normalized spatial autocorrelation function (SACF) for the consecutive time frames of Fig. 5.2A. The grey curves are SACFs of the individual frames, the black data points are the average SACFs of the 20 frames fitted with a Gaussian curve. The average radius of the domains, derived from the

Chapter 5. Divalent ions induce transient domains of interfacial ordered water in lipid membranes

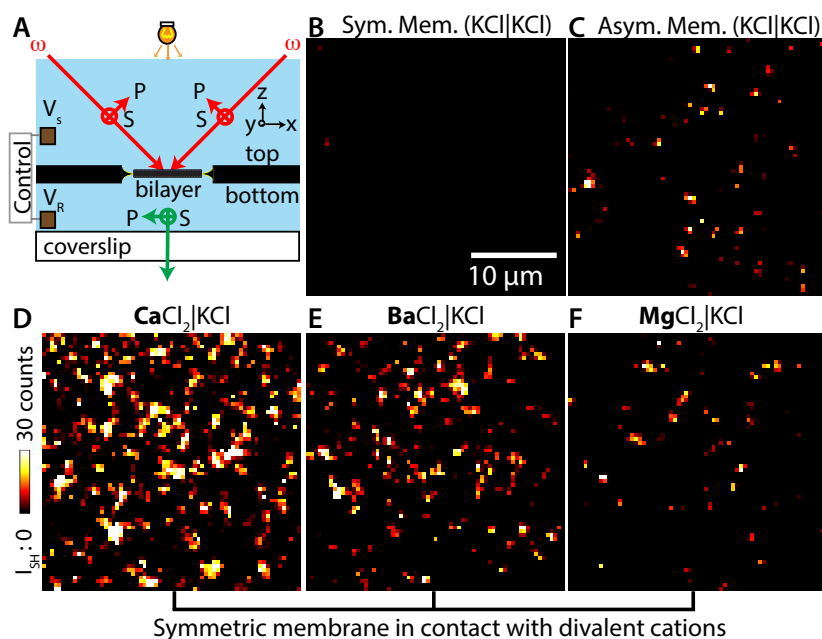


Figure 5.1 – Divalent cations induce transient domains of ordered interfacial water. (A) Two counter-propagating beams (190-fs, 1030 nm, ω , red arrows) overlap in space and time to illuminate the lipid bilayer membrane. SH photons (2ω , green arrow) are collected (magnification: 50x, NA = 0.65) in the phase-matched direction. SH images of (B) a symmetric membrane composed of 70:30 mol % DPhPC:DPhPA and (C) an asymmetric membrane composed of 70:30 mol % DPhPC:DPhPA (top leaflet) and DPhPC (bottom leaflet) in contact with a 150 μM pH neutral KCl solution. (D-F) SH images of a symmetric membrane composed of 70:30 mol % DPhPC:DPhPA in contact with a 150 μM pH neutral KCl solution (bottom leaflet), and a pH neutral CaCl_2 (D), BaCl_2 (E) and MgCl_2 (F). The images were collected with all beams P-polarized, and represent 20 x 560 ms frame averages. The scale bar is the same for all images. The SH image of a 150- μM KCl solution was subtracted from the images to remove the hyper-Rayleigh scattering (HRS) contribution.

full-width-at-half-maximum (FWHM) of Fig. 5.2B is 1.5 μm . Figure 5.2C shows the normalized temporal autocorrelation function (TACF) for the consecutive time frames of Fig. 5.2A. Applying the same analysis to a series of single frame images of Ba^{2+} and Mg^{2+} , we obtained the same average radius and temporal decay of their spatiotemporal correlations (see Appendix, 5.5.1, Fig. 5.5). Thus, there is no correlation between the domains on the time scale of acquisition. The characteristic time of each domain is, therefore, shorter than the recording time. To understand the coupling between the SH domains on each leaflet, we recorded SH images of a 70:30 mole % DPhPC:DPhPA symmetric bilayer with 150 μM CaCl_2 added to both leaflets. The 20 frame (10.4 s) average result is shown in Fig. 5.2D. The image shows a SH contrast that has a comparable intensity to the response of the asymmetric lipid bilayer in Fig. 5.1C but less intensity compared to the response of a symmetric bilayer in Fig. 5.1D where only one leaflet is in contact with CaCl_2 . This means that there is no strong coupling between the hydration shells of opposing leaflets.

5.3.2 Quantifying membrane potential and free energy changes.

Figures 5.1 and 5.2 show that divalent cations induce transient structural heterogeneities of ordered water in freestanding lipid bilayer membranes. The hydration shells of both leaflets are only partially

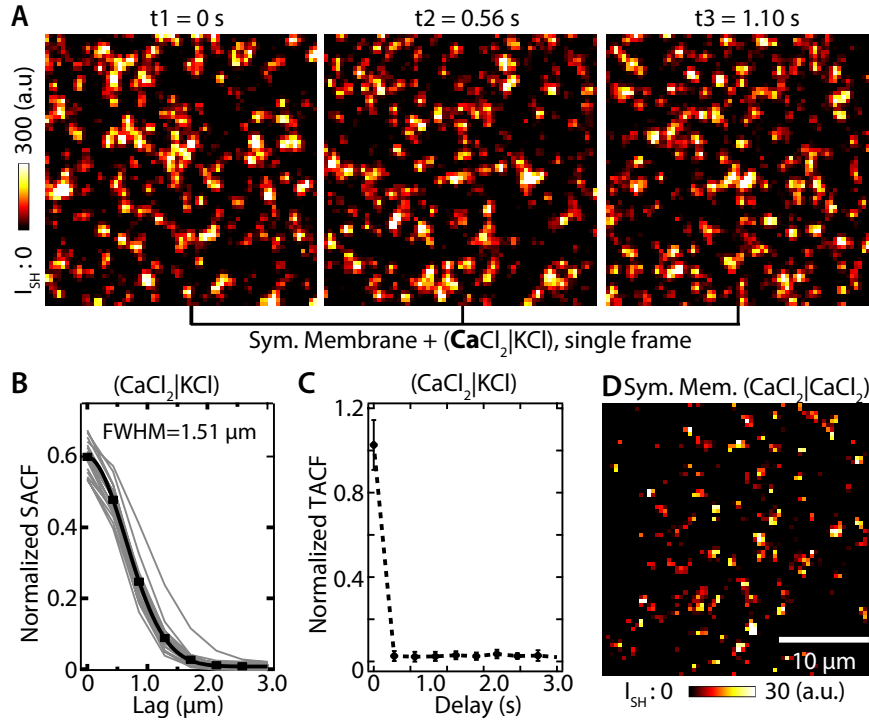


Figure 5.2 – Spatiotemporal dynamics of ion-induced ordered water domains. (A) Time series of SH images (560 ms each) of a symmetric membrane composed of 70:30 mol % DPhPC:DPhPA with the top leaflet in contact with $(\text{CaCl}_2)_{aq}$ and the bottom leaflet in contact with $(\text{KCl})_{aq}$. (B) Normalized spatial autocorrelation function (SACF) of the single frame images in (A). The gray curves represent the SACF of the individual frames (20 frames total) and the black data points are the average SACF values of all the gray curves fitted with a Gaussian curve. (C) Normalized temporal autocorrelation function (TACF) of the images in (A) showing no temporal correlation between frames. The scale bar is the same for all images. (D) SH image (average of 20 frames, 560 ms) of a symmetric membrane composed of 70:30 mol % DPhPC:DPhPA where both leaflets are in contact with $(\text{CaCl}_2)_{aq}$. This SH image was corrected for hyper-Rayleigh scattering by subtracting a 150- μM KCl solution SH image. All images were collected with all beams P-polarized. The scale bar is the same for all images.

correlated, and specific ion effects are important. These are clearly surprising findings and to obtain more insight into the physicochemical behavior we next quantify the spatiotemporal membrane potential, surface charge distribution, and free energy landscape. Theory and experiments [184, 77] have shown that the SH intensity of an interface depends quadratically on the surface potential (Φ_0) and for lipid bilayers with two oppositely oriented membrane interfaces we have [80]:

$$I(2\omega, x, y) \approx I(\omega, x, y)^2 \left| \chi_{s1}^{(2)}(x, y) - \chi_{s2}^{(2)}(x, y) + \chi^{(3)'} f_3 (\Phi_{0,1}(x, y) - \Phi_{0,2}(x, y)) \right|^2 \quad (5.1)$$

where $\chi_{s1}^{(2)}/\chi_{s2}^{(2)}$ and $\Phi_{0,1}/\Phi_{0,2}$ are the surface-second order susceptibilities and the surface potentials of each leaflet, respectively, and $\chi^{(3)'}$ is an effective third-order susceptibility of the aqueous phase [185]. The subscripts 1,2 refer to the top/bottom leaflets of the bilayer, x, y are the spatial coordinates, ω is the frequency of the fundamental beam, and $f_3 \rightarrow 1$ for transmission experiments [78]. For symmetric bilayers, $\chi_{s1}^{(2)} = \chi_{s2}^{(2)}$, equation 5.1 is reduced to $I(2\omega, x, y) \propto \left| \chi^{(3)' (\Phi_{0,1}(x, y) - \Phi_{0,2}(x, y)) \right|^2$.

Chapter 5. Divalent ions induce transient domains of interfacial ordered water in lipid membranes

With identical surface potentials the coherent SH intensity vanishes altogether (Fig. 5.1B). By recording SH images of an asymmetric charged leaflet as a function of external electric bias we showed that it is possible to convert the SH intensity scale into a membrane potential $\Delta\Phi_0 = \Phi_{0,1}(x, y) - \Phi_{0,1}(x, y)$ scale (see the Appendix, 5.5.4 for details). From $\Delta\Phi_0$ the change in electrostatic free energy (ΔG) is found as $\Delta G = 2e\Delta\Phi_0$, and the ion-lipid dissociation constant (K_D) is given by $\Delta G = -RT\ln(K_D)$ where T is the temperature and R the gas constant [19]. Furthermore, the surface charge density ($\Delta\sigma_0$) was modeled with the parallel plate capacitor model [200], appropriate for divalent ion – negatively charged interface interactions [111, 107], where $\Delta\sigma_0 = C \cdot \Delta\Phi_0$, with $C = \epsilon_0\epsilon/d$, $\epsilon = 2.1$ and $d = 4$ nm, the dielectric constant and thickness of the hydrophobic core respectively [149].

Table 5.1 – Image averaged and single domain values of $\Delta\Phi_0$, $\Delta\sigma_0$, ΔG and K_D taking as the range of the domain values as domain average ± 1 standard deviation.

		$\Delta\Phi_0$ (mV)	$\Delta\sigma_0$ (mC/m ²)	ΔG (kT)	K_D (M)*
Ca ²⁺	average	-217	-1.02	17	$2.1 \cdot 10^{-7}$
	domain	$245 < \Delta\Phi_0 < 329$	$1.15 < \Delta\sigma_0 < 1.55$	$19 < \Delta G < 26$	$1.9 \cdot 10^{-8} < K_D < 1.3 \cdot 10^{-11}$
Ba ²⁺	average	-154	-0.72	12	$1.6 \cdot 10^{-5}$
	domain	$130 < \Delta\Phi_0 < 209$	$0.61 < \Delta\sigma_0 < 0.98$	$10 < \Delta G < 16$	$2.4 \cdot 10^{-4} < K_D < 1.15 \cdot 10^{-7}$
Mg ²⁺	average	-70	-0.33	5.4	$2.3 \cdot 10^{-2}$
	domain	$68 < \Delta\Phi_0 < 108$	$0.32 < \Delta\sigma_0 < 0.51$	$5.3 < \Delta G < 8.4$	$2.0 \cdot 10^{-2} < K_D < 4.51 \cdot 10^{-3}$

*The following are found in the literature: Ba²⁺ with DMPA, $K = 10^{-6}$ M [201], Ca²⁺ induces fusion of PA containing vesicles at ~ 100 μ M [105, 106, 104].

Figure 5.3 shows the measured intensity values (Fig. 5.3A) (corrected for HRS by image subtraction), extracted values for the membrane potential and the surface charge density ($\Delta\Phi_0$; $\Delta\sigma_0$, 5.3B), the electrostatic free energy change and the ion binding dissociation constant (ΔG ; K_D , 5.3C) for the different divalent cations SH imaged in Fig. 5.1D-5.1F. The average quantities are displayed on each panel. Table 5.1 lists the image stack averaged values of $\Delta\Phi_0$, $\Delta\sigma_0$, ΔG and K_D and the values for the domains (corrected for HRS, see Appendix 5.5.2, 5.5.3 and Fig. 5.6, Fig. 5.7). Our average values are in good agreement with (the limited) literature on binding constants [201, 105, 106, 104]. However, Figs. 5.1-5.3 and Table 5.1 show a very interesting unexpected aspect: Instead of a uniformly distributed divalent cation-lipid binding, there are transient structures. Examining these domains, much larger values are found for $\Delta\Phi_0$, $\Delta\sigma_0$, ΔG , and K_D , resulting in actual binding dissociation constants that are up to 4 orders of magnitude larger than the total spatially averaged value. In addition, there are places on the image where virtually no binding occurs, and the chemical structures where binding occurs are short-lived and continuously redistribute across the membrane.

5.3.3 From transient membrane structure to curvature.

The transient structural domains (Fig. 5.3) exhibit membrane potential fluctuations of up to -386 mV (with $\Delta G = 28.6$ kT). Although the molecular level interactions are complex, our findings can be rationalized qualitatively as follows (Fig. 5.4): The addition of divalent ions leads to an electrostatic field gradient (Fig. 5.4B) that induces strain in the membrane via a surface pressure gradient across the membrane and steric pressure along the membrane [202, 157]. A homogeneous distribution of ions results in high local strain due to the electromechanical coupling with membrane fluctuations. However, the local clustering of ions can potentially relax high strains when these clusters are spread out over larger distances [203, 204] (Fig. 5.4C). Using a mean-field liquid crystal membrane approximation to calculate the curvature as a function of an applied electric field [205, 206], and using again the

approximation of an electric capacitor, we estimated the curvature H for the three cations. The total curvature of the membrane in response to an applied electric field is given by $H = \frac{fE}{2\kappa} = \frac{f\Delta\Phi_0}{2\kappa d}$ with f the flexocoefficient of the membrane, and κ the bending modulus. Using $10 \text{ kT} < \kappa < 20 \text{ kT}$ and $10^{-21} < f < 10^{-18} \text{ C}$ [192], we find $3.6 \cdot 10^{-4} < H < 0.98 \text{ nm}^{-1}$. The small value of curvature corresponds to a membrane with a large bending modulus and with a low flexoelastic coefficient while the large curvature values correspond to a membrane with a small bending modulus and a large flexoelastic coefficient. Although this model ignores both thermal fluctuations and other electromechanical effects, it shows that the measured transient fluctuations in Fig. 5.3 can lead to transient curvature fluctuations. This, in turn, will result in surface tension fluctuations [207, 208]. Fig. 5.4D shows topographic maps of membrane deformation generated from the images of Fig. 5.3B, showing that different electric fields can induce different extents of transient curvatures for Ca^{2+} , Mg^{2+} and Ba^{2+} ions, following the trend of the Hofmeister series. The large and dense potential fluctuations induced by Ca^{2+} should thus result in a larger variation in the height profile of the membrane. The smaller and more spread out fluctuations for Mg^{2+} (and Ba^{2+}) result in smaller curvature deviations and thus in smaller height profile fluctuations.

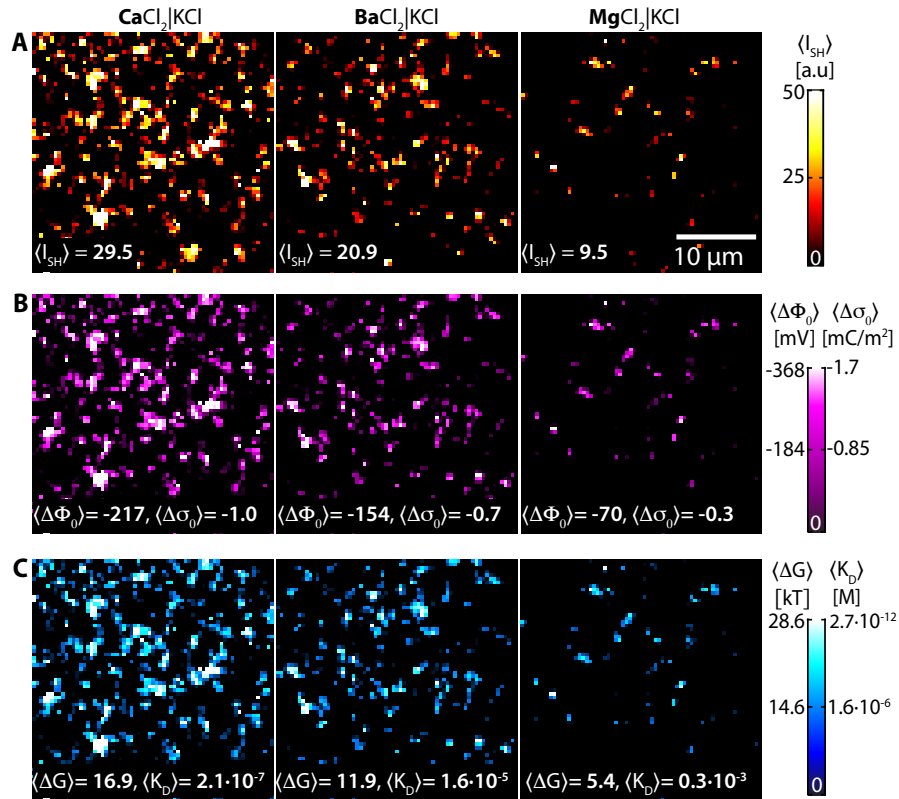


Figure 5.3 – Quantifying the free energy landscape of membranes. (A) Average SH intensity $\langle I_{SH} \rangle$, (B) the change in membrane potential $\langle \Delta\Phi_0 \rangle$ and surface charge density $\langle \Delta\sigma_0 \rangle$ (assuming a parallel plate capacitor model), (C) free energy of binding $\langle \Delta G \rangle$ and ion binding dissociation constant $\langle K_D \rangle$ for symmetric membranes composed of 70:30 mol % DPhPC:DPhPA where the top leaflet is in contact with divalent cations: Ca^{2+} , Ba^{2+} , and Mg^{2+} and the bottom leaflet is in contact with KCl ions with the same ionic strength ($150 \mu\text{M}$). The scale bar is the same for all images. Units of the quantities mapped are provided with the color scale bar.

Chapter 5. Divalent ions induce transient domains of interfacial ordered water in lipid membranes

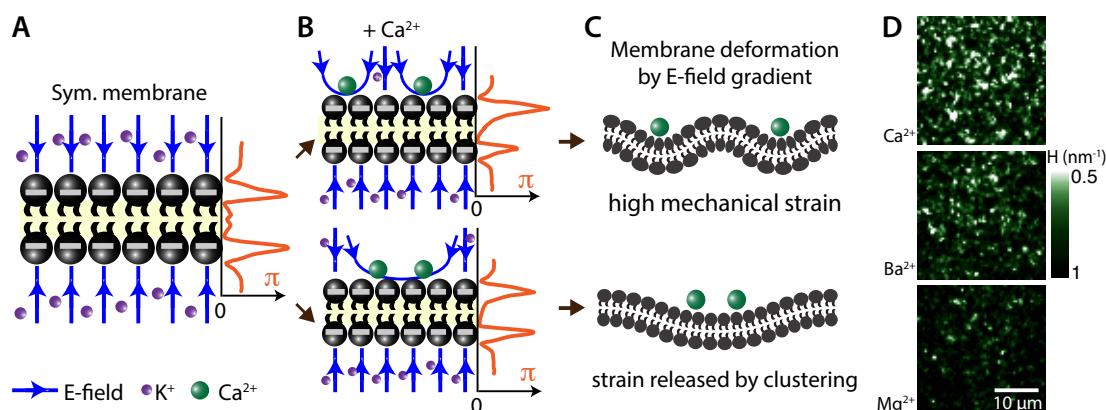


Figure 5.4 – Specific ion induced transient curvature. (A) Schematic of a symmetric negatively charged membrane in solution. (B) The binding of Ca^{2+} to a symmetric negatively charged membrane induces an asymmetric electric field gradient, which is different for a homogeneous (top) or clustered (bottom) distribution of cations, leading to different pressure profiles, and (C) consequently different membrane curvature. (D) Topographic maps of membrane deformation of the membranes of Fig 3, showing more pronounced transient curvature fluctuations for $\text{Ca}^{2+} > \text{Ba}^{2+} > \text{Mg}^{2+}$ (using $f = 5 \cdot 10^{-19}$ C, $\kappa = 15$ kT and $d = 4$ nm).

5.4 Summary and Conclusions

Summarizing, at physiological concentrations Ca^{2+} , Mg^{2+} , and Ba^{2+} induce short-lived (<500 ms) 1.5 micron-sized domains of ordered interfacial water. Converting the SH intensity into membrane potential, surface charge density, membrane hydration free energy, and binding dissociation constant maps, we obtain trends in the order $\text{Ca}^{2+} > \text{Mg}^{2+} > \text{Ba}^{2+}$, for all four quantities and reach domain values of -368 mV, -1.7 mC/m², 28.6 kT, and $2.7 \cdot 10^{-12}$ M that deviate up to 4 orders of magnitude from current reaction constant values that are based on a mean-field interpretation. Additionally, the transient electric field gradients across the membrane lead to transient curvature, resulting in temporal and spatial variations in the mechanical properties for the membrane. Thus, aside from having a local specific interaction with lipids as has been previously known [111, 110, 14, 197], divalent ions also influence the spatiotemporal chemical, electric and mechanical membrane properties, leading to a diversification of membrane environments and a new mechanism for coupling local chemical interactions with macroscopic behavior. Such an effect potentially plays an important role in membrane protein interactions, important for structuring, signaling, and transport.

5.5 Appendix

5.5.1 Spatiotemporal autocorrelation of ion-induced domains

To obtain spatiotemporal dynamics between domains, we applied image correlation spectroscopy originally developed by Petersen et. al [209, 210, 211, 212, 213, 214] for laser-scanning systems and extended by Gaborski et. al [215] for uniform illumination. We calculated the normalized spatial autocorrelation function (SACF) and temporal autocorrelation function (TACF) from single frame images (acquisition time of 560 ms, 20 frames total) for each divalent cation in Fig. 5.1D-E. The full width at half maximum (FWHM) of the SACF reports on the characteristic radius of the domains

whereas the FWHM of the TACF reports on the characteristic lifetime of the domains. Figure 5.5A shows the normalized spatial autocorrelation function (SACF). Each data point is the average of 20 frames and solid lines represent fitted Gaussian curves. It can be seen that the average radius of the domains for all three ions is 1.5 microns. The spatial autocorrelation function $g(\xi)$ at $\xi = 0 \mu\text{m}$, $g(0)$, reports on the density of emitters in the focal volume via $g(0) \sim 1/N$ and N is the density of emitting domains. Figure 5.5A shows that the density of domains is in the order of $\text{Ca}^{2+} > \text{Ba}^{2+} > \text{Mg}^{2+}$. Figure 5.5B shows the normalized temporal autocorrelation function (TACF) for the three divalent cations. On the time scale of our recording, there is no temporal correlation between the domains. The characteristic time of each domain is, therefore, shorter than the recording time.

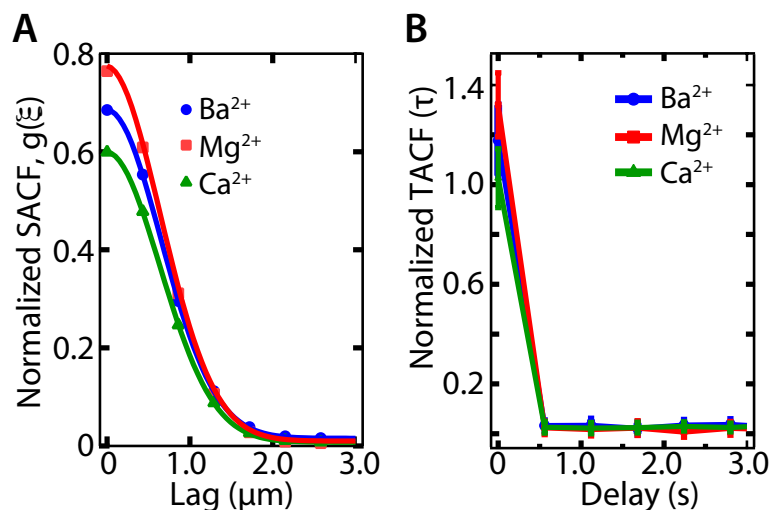


Figure 5.5 – Spatiotemporal autocorrelation of ion-induced domains for different divalent cations. (A) Normalized spatial autocorrelation function (SACF) where each data point represent the average of 20 frames (560 ms each) and solid lines are fitted Gaussian curves. (B) Normalized temporal autocorrelation function (TACF).

5.5.2 The intensity distribution of the ion-induced domains

The average intensity distribution of domains in a single frame (560 ms/frame) at different electrolyte conditions is shown in Fig. 5.6. The intensity distributions were obtained from $N > 1200$ domains (distributed over 20 frames). These domains were defined as follows. We used the GDSC ImageJ plugin developed by Alex Herbert [216]. We set threshold intensity (I_{th}) defined as the maximum read-noise plus the maximum dark current noise. This value determines the upper limit of the noise of the system. To determine I_{th} in counts, we calibrated the camera with the gain settings used during acquisition and obtained the number of counts/photo-electron [217]. The average domain size was determined from the SACF of Fig. S1, and a region of interest represented by a square that has 2 times the FWHM of the SACF as length was used to compute the average domain intensity. The following parameters from the GDSC ImageJ plugin were used: smoothing = 0, box_size = 1, background = 550 (dark current noise), min_height = 305 (read noise upper limit) fraction_above_background = 0, min_width = 0 top_n = 0, neighbour_check border = 2, fit_function=[Free circular], fit_criteria=[Least-squared error] max_iterations = 20, significant_digits = 4, coord_delta = 0.0100, single_fit single_region_size = 5, initial_stddev = 0.000.

Figure 5.6 shows that changing electrolytes increases the average SH response per domain (μ)

Chapter 5. Divalent ions induce transient domains of interfacial ordered water in lipid membranes

and spread of values per domain (σ) between the ions in the order $\text{Ca}^{2+} > \text{Ba}^{2+} > \text{Mg}^{2+}$. Comparing the relative increase between the three ions and removing the SH contribution from the aqueous solution, Ca^{2+} increases the intensity by 163 % compared to Ba^{2+} and 325 % to Mg^{2+} . The spread of the values per domain change by 106 % and 211 %, respectively.

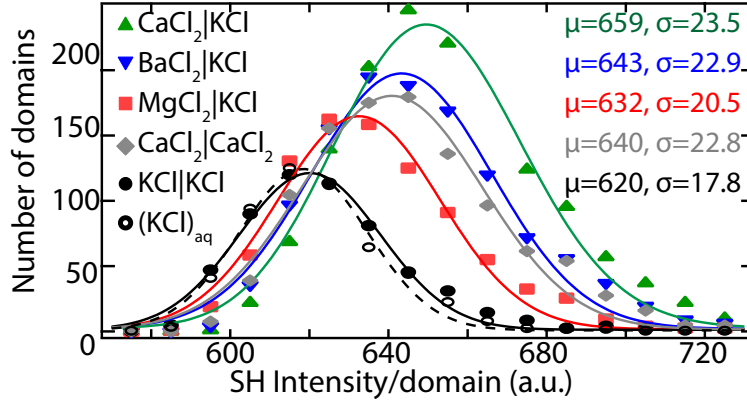


Figure 5.6 – Average intensity distribution of domains at different electrolyte conditions. The legend denotes the aqueous solution ($I = 150 \mu\text{M}$ and pH neutral) in contact with a symmetric membrane composed of 70:30 mol % DPhPC:DPhPA. Data points are fitted with a Gaussian distribution and the mean (μ) and spread of values per domain (σ) are shown.

5.5.3 Single frame correction for hyper-Rayleigh scattering

Figure 5.7 shows single frame images for Ca^{2+} , Ba^{2+} , and Mg^{2+} interaction membranes. Note that the top row is identical to that of Fig. 5.2A. These single frame images still contain sparse incoherent SH scattering intensity from the adjacent solution (also known as hyper-Rayleigh scattering, examples of such contribution are indicated in Fig. 5.7 with green circles). Fig. 5.6 (black curve, open circles) shows the intensity distribution of an electrolyte solution, which arises just from HRS. Since the HRS response is distributed over the image in a random way and since the occurrences are sparse, it is not possible to simply subtract an image (as can be done for longer acquisition times). Therefore, we scaled the intensity distribution per domain using the average occurrence, mean and standard deviations of the HRS intensity recorded from aqueous solution (black curve, open circles in Fig. 5.6).

5.5.4 From SH intensity to surface potential difference

The SH intensity was converted to surface potential difference as described previously [80]. By recording the SH intensity as a function of external bias (U) it is possible to determine the unknown values of $\Delta\chi_s^{(2)} = \chi_{s1}^{(2)} - \chi_{s2}^{(2)}$ and $\Delta\Phi_0$. We use a liquid asymmetric membrane composed of 30:70 mol % negatively charged (with a charge $-e$ per lipid):neutral lipid mixture on one leaflet in contact with a liquid neutral lipid on the other leaflet. Figure 5.8 shows the image integrated SH intensity as a function of applied electrical bias U . Since this curve represents the average of the image, it can be described using a mean-field model. Explicitly, Eq. 5.2 becomes

$$\langle I(2\omega) \rangle_{x,y} = C \langle I(\omega)^2 \rangle_{x,y} \left| \langle \Delta\chi_s^{(2)} \rangle_{x,y} + f_3 \chi^{(3)'} \langle \Delta\Phi_0 \rangle_{x,y} \right|^2 \quad (5.2)$$

The average membrane potential is represented by a linear relation, retrieved from a COMSOL simulation [80], $\langle \Delta\Phi_0 \rangle_{x,y} = \langle \Delta\Phi_{0,init} \rangle_{x,y} + \beta U$, where $\beta = 0.97$ (retrieved from the COMSOL simulation), and $\langle \Delta\Phi_{0,init} \rangle$ is the spatially averaged value of $\Delta\Phi_0$ at $U = 0$, which is identical to the negative bias, for which Eq. 5.2 has a minimum. With the effective third-order susceptibility of water known, $\chi^{(3)'} = -10.3 \cdot 10^{-22} \text{ m}^2/\text{V}^2$ [185], a fit to Eq. 5.2 of the data in Fig. 5.8 yields the image averaged value for $\Delta\chi_s^{(2)} = \chi_{s1}^{(2)} - \chi_{s2}^{(2)}$ ($5 \cdot 10^{-24} \text{ m}^2/\text{V}$ [185]). Knowing $\Delta\chi_s^{(2)}$ and $\chi^{(3)'}$ it is now possible to calculate $\Delta\Phi_0(x, y)$ for each pixel that has a different intensity. Using Eq. 5.1 and assuming that $\Delta\chi_s^{(2)} = \chi_{s1}^{(2)} - \chi_{s2}^{(2)}$, the variation in SH intensity can be converted to membrane potential differences. For the data in Figs. 5.1 and 5.2, we use a symmetric membrane with the same composition (30:70 mol % negatively charged (with a charge $-e$ per lipid):neutral lipid mixture on both leaflets). The divalent cations bind with part of the negatively charged head groups and neutralize them, effectively achieving a membrane that has a similar composition as one that has a partially charged leaflet in contact with a neutral leaflet.

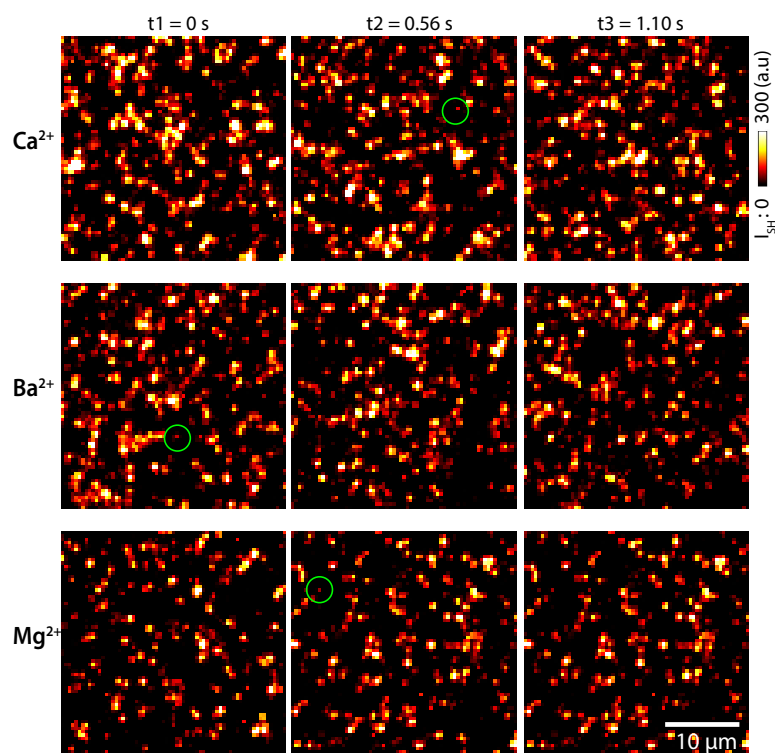


Figure 5.7 – Single frame SH images of ion-induced ordered water domains. (A) Time series of SH images (560 ms each) of a symmetric membrane composed of 70:30 mol % DPhPC:DPhPA with the top leaflet in contact with $(\text{CaCl}_2)_{aq}$ and the bottom leaflet in contact with $(\text{KCl})_{aq}$. (B) Time series of SH images (560 ms each) of a symmetric membrane composed of 70:30 mol % DPhPC:DPhPA with the top leaflet in contact with $(\text{BaCl}_2)_{aq}$ and the bottom leaflet in contact with $(\text{KCl})_{aq}$. (C) Time series of SH images (560 ms each) of a symmetric membrane composed of 70:30 mol % DPhPC:DPhPA with the top leaflet in contact with $(\text{MgCl}_2)_{aq}$ and the bottom leaflet in contact with $(\text{KCl})_{aq}$. All images were collected with all beams P-polarized. The green circles represent examples for potential hyper-Rayleigh contributions.

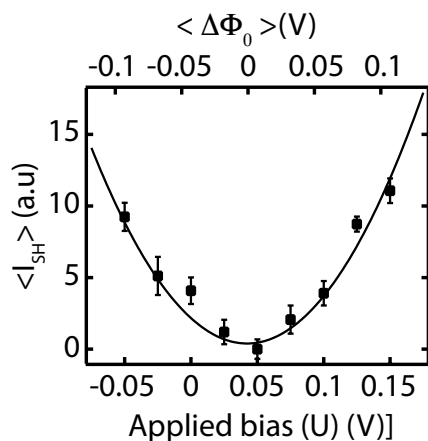


Figure 5.8 – SH intensity as a function of applied external bias. Spatially averaged SH intensity as a function of external bias for an asymmetric membrane composed of 30:70 mol % negatively charged / neutral lipid mixture on one leaflet in contact with a neutral lipid on the other leaflet. The solid line is a fit to Eq. 1. The top axis was computed by calculating $\langle \Delta\Phi_0(x, y) \rangle_{x,y} = \langle \Delta\Phi_{0,ini} \rangle_{x,y} + \beta U$, knowing $\langle \Delta\Phi_{0,ini} \rangle_{x,y}$, β and U .

6 Spatiotemporal imaging of water in operating voltage-gated ion channels reveals the slow motion of interfacial ions

Ion channels are responsible for numerous physiological functions and rely on a complex molecular interfacial architecture that heavily relies on water. Although ion channel structure has been studied, the molecular mechanism of operational ion channels and in particular the role of water in it has not been achieved. Here, we perform spatiotemporal second harmonic imaging and capacitance measurements of operational voltage-gated alamethicin ion channels in a freestanding lipid membrane surrounded by aqueous solution on either side and having the same physiologically relevant salt concentration. The image contrast of the opening and closing of ion channels that is controlled by an external bias is due to changes in the orientational distribution of water molecules induced by electric field gradients. Only a fraction of 10^{-4} of the transported ions arrives at the hydrated membrane interface, leading to interfacial electrostatic changes on the timescale of a second. Finally, we quantify the spatiotemporal distribution of ion channels and record their activity during a gating cycle. Ion channels in high-density areas exhibit a lower rate of interfacial charge buildup, which is likely caused by crowding. Our study shows that ion transport along the membrane, which is thought to be involved in the propagation of action potential, is taking place over seconds. This observation suggests a more complex mechanism for the propagation of action potentials.

This chapter is based on the author's journal article: **O. B. Tarun**, M.Yu. Eremchev, A. Radenovic, and S. Roke. Submitted (2018).

6.1 Introduction

Transport of ions across membranes is crucial to the survival of cells and extends to the organism level. In order to transport ions across the membrane, the cell uses active and passive transport. One example of these is voltage-gated ion channels that selectively transport ions in and out of the cell and generate membrane potential gradients that form the basis of neuronal signaling [218]. As ion channels are fundamentally important for cell functioning, the dysfunction of ion-channels is related to a number of diseases including neuronal disorders such as epilepsy, ataxia [115] and hypertension [116], and secretion related disorders such as cystic fibrosis and hypoglycemia [117]. Understanding the operation of voltage-gated ion channels on a molecular level, without modifying the molecular environment of the membrane is a formidable challenge that needs to be solved if we are to develop better drugs and treatment to cure ion-channel related diseases.

The study of ion channels follows a structural biology approach that involves crystallographic, cryo-electron microscopy (cryo-EM), and NMR measurements of subunits. In addition, using volumetric mapping by AFM and cryo-EM, dynamic fluorescence to tag side chain motion and advance molecular dynamics simulations, it is possible to map the structure of certain channels [219]. Operational parameters such as current, efficiency and selectivity are determined by electric characterization methods, such as patch clamp or micro-electrode arrays [220, 221, 222, 223, 224]. Although many computational studies exist that address the question of how ion channels operate [219, 225, 226, 227, 228], experimental molecular level information, that also includes following the structure of water of operating ion channels has not been achieved so far. This is a challenge given the expected low number of water molecules inside a channel ($\sim <50$). Recent reflection sum frequency generation (SFG) studies on artificial pores deposited onto a silica supported lipid bilayer showed promising results that indicated the possibility of measuring alamethicin adsorption [229] and changes in the water structure in proximity to I-quartet artificial pores [230]. Using a different approach, we demonstrated spatiotemporal second harmonic (SH) imaging of the dynamic movement of water confined and electrically stimulated inside a <1 -micron wide glass pore, on a sub-second timescale [88]. Water aligned with the externally applied field generated a bright SH response, while in the absence of the field no response was measured. This experiment suggests that it may be possible to use the same approach to measure ion channels operation in real time on a molecular level.

Here, we performed SH imaging experiments on operational voltage-gated alamethicin peptide ion channels inserted into a freestanding lipid membrane that is surrounded by an aqueous solution on either side. Figure 6.1A illustrates the transport of ions when voltage-gated ion channels are activated. Upon application of an electrostatic potential gradient the channels open and cations are transported towards the negative electrode, while anions are transported towards the positive electrode. Figure 6.1B shows a measured macroscopic current-voltage (I-V) trace, typical for multi-pore ion channels [128, 134, 231, 125, 232, 132], of alamethicin incorporated in a neutral symmetric 1,2-diphytanoyl-sn-glycero-3-phosphocholine (DPhPC) bilayer for 100 mM and 500 mM KCl salt concentration. Changing the salt concentration of alamethicin results to more ion channels incorporated in the bilayer. This response is due to the shift in adsorption equilibrium of alamethicin at the membrane interface (salting-out effect), whereby at higher salt concentration, there is a higher concentration of alamethicin monomers adsorbed at the interface. Furthermore, since alamethicin has a preferred directionality to incorporate in the membrane, the I-V curve is not symmetric [135, 136]. Applying dynamic SH imaging to this system, we observe that the opening and closing of ion channels leads to changes in the SH contrast. These changes are surprisingly slow and occur on the order of seconds. With the aid of capacitance measurements, the SH intensity change is traced back to the change in the orientation

distribution of water molecules induced by the electric field gradients inside and in the vicinity of the pore as being the main source of SH contrast. We find that, as the channel opens only a small fraction (10^{-4}) of ions that are transported arrives at the hydrated membrane interface, which explains why the interfacial electrostatic changes are so slow. Finally, we quantify the spatiotemporal distribution of ion channels and record their activity during a gating cycle. Ion channels in high-density areas exhibit a lower rate of interfacial charge buildup, which is likely caused by crowding. Overall our study suggests that membrane lateral diffusion of ions is too slow to be involved in the propagation of action potentials.

6.2 Materials and Methods

6.2.1 Chemicals and lipids

Alamethicin from *Trichoderma viride* (Sigma-Aldrich, >98%), DPhPC in powder form (>99%) (Avanti Polar Lipids, Alabama, USA), hexadecane ($C_{16}H_{34}$, 99.8%, Sigma-Aldrich), squalene ($C_{30}H_{50}$, >98%, Sigma-Aldrich), hexane (C_6H_{14} , Sigma-Aldrich, >99%), chloroform (>99.8%, Merck), hydrogen peroxide (30%, Reactolab SA), sulfuric acid (95-97%, ISO, Merck), KCl (99.999%, Aros) were used as received. Aqueous solutions were made with ultra-pure water (H_2O , Milli-Q UF plus, Millipore, Inc., electrical resistance of $18.2\text{ M}\Omega\text{ cm}$). All aqueous solutions were filtered with $0.1\ \mu\text{m}$ Millex filters. The coverslips used in the imaging were pre-cleaned with piranha solution (1:3 - 30% H_2O_2 : 95-97% H_2SO_4) and thoroughly rinsed with ultrapure water. The chamber and Teflon films that were used in forming freestanding planar lipid bilayers were cleaned with ethanol, methanol, and chloroform and thoroughly rinsed with ultrapure water.

6.2.2 Formation of freestanding lipid bilayers and incorporation of alamethicin peptides

Freestanding horizontal planar lipid bilayers were formed by monolayer apposition, following the Montal-Mueller technique (see Chapter 2.2 for details). To incorporate alamethicin ion channels, we added $5\ \mu\text{L}$ of alamethicin peptide solution (in absolute ethanol with a concentration of $9.8\ \mu\text{g}/\text{mL}$). The corresponding concentration of alamethicin in solution is $\sim 50\ \text{nM}$ (or $98\ \text{ng}/\text{mL}$), the top compartment having $500\ \mu\text{L}$ of aqueous solution. Unless otherwise stated, we added peptides on the top compartment (see Fig. 6.1C). The bottom compartment was the electrical ground of the system (Fig. 6.1C). Incorporation of voltage-gated alamethicin pores was confirmed by performing current – voltage (I-V) curves by ramping the voltage from $-250\ \text{mV}$ to $250\ \text{mV}$. Typical IV curves show a voltage threshold where the current exponentially jumps as shown in Fig. 6.1B.

6.2.3 Second harmonic (SH) imaging.

The optical setup was characterized in detail in Chapter 2.1. The images were collected with a 50x objective lens (Mitutoyo Plan Apo NIR HR Infinity-Corrected Objective, 0.65 NA). All images were recorded with the beams polarized parallel to the plane of incidence (P).

Chapter 6. Spatiotemporal imaging of water in operating voltage-gated ion channels reveals the slow motion of interfacial ions

6.2.4 Capacitance measurements of activated channels

To measure the membrane capacitance of operating ion channels, we used the "SINE + DC" lock-in mode of HEKA patch clamp amplifiers which was describe in Chapter 2.3.1. Briefly, we used a stimulus (U) with an AC excitation U_1 and a DC bias U_0 ,

$$U = U_0 + U_1 \sin 2\pi f t \quad (6.1)$$

where $U_0 = 1$ mV for close channels and $U_0 > 100$ mV for open channels (depending on the voltage threshold to open the channels, we set U_0 20-30 mV above threshold), $U_1 = 10$ mV, $f = 1$ kHz and $t = 100$ ms, corresponding to 100 sine wave cycles. We obtained capacitance measurement every 200 ms of activated and deactivated ion channels by setting U_0 to a block square pulse stimulus (see Fig 6.2B).

6.3 Results & Discussions

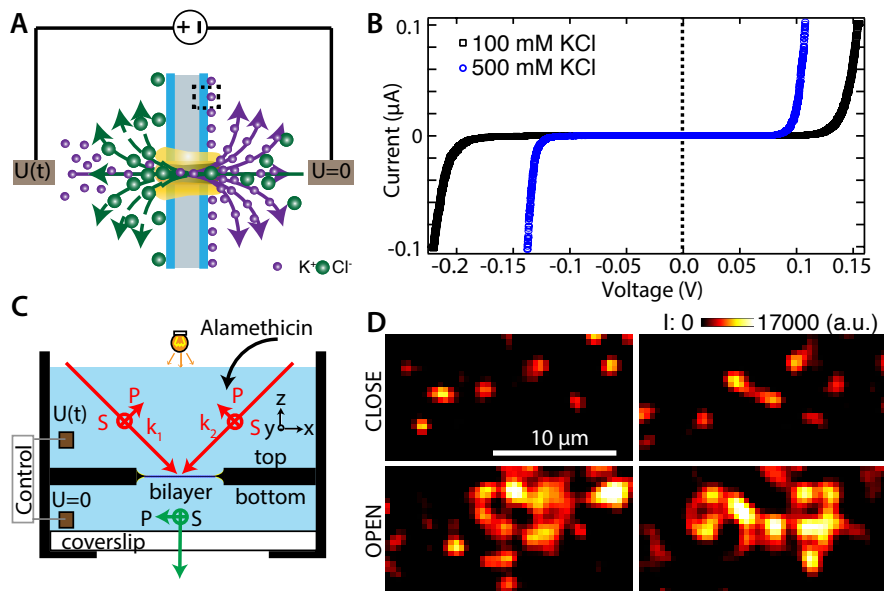


Figure 6.1 – SH imaging of voltage-gated ion channel operation. (A) Schematic of ion transport and charge separation when ion channels are activated by an applied bias. The arrows point to the direction of ion transport. (B) Alamethicin-induced macroscopic current-voltage response for 100 mM KCl and 500 mM KCl, 0.1 $\mu g/mL$ alamethicin added to one side of a symmetric bilayer composed of DPhPC. (C) Schematic of the optical layout where two counter-propagating beams (red arrows: $\omega = 1032$ nm, $\tau = 190$ fs pulse duration, $f = 200$ kHz repetition rate) are incident under an angle of 45° with respect to the surface normal and overlap in space and time to illuminate the bilayer. SH photons (green arrow, 2ω) are collected in the phase-matched direction. Alamethicin peptides are added to the top side of the bilayer. Abbreviations: P: polarization direction in the plane of the beams, S: polarization direction out of plane of the beams, $k_{1/2}$: wave vector of the exciting beams and k_0 : wave vector of the emitted beam. (D) SH images (single frame, 560 ms; magnification: 50 \times , NA = 0.65, Gaussian smooth $\sigma=1$) following the closing (top row) and opening (160 mV, bottom row) of voltage-gated alamethicin ion channels. The images are collected with all beams P-polarized.

6.3.1 SH imaging of ion channels

Freestanding horizontal planar lipid membranes are formed in a $\sim 100\text{-}\mu\text{m}$ sized circular aperture in a $25\text{-}\mu\text{m}$ thick Teflon film by following the procedure of Montal-Mueller [49, 146]. Here, two lipid monolayers are formed at two separate air/water interfaces and subsequently apposed to form a lipid bilayer. The horizontally mounted planar freestanding lipid membranes are second harmonic (SH) imaged with a medium repetition rate wide field second harmonic (SH) microscope. The SH microscope consists of two counter-propagating 1032 nm 190 fs pulsed beams at 200 kHz repetition rate that are incident at an angle of 45° with respect to the surface normal (Fig. 6.1C). The SH photons are generated in the phase matched direction (green arrow, Fig. 6.1C) and collected using a $50\times$ objective with a numerical aperture (NA) of 0.65 . From previous measurements of non-resonant SH imaging (see Chapter 4.3.1), we showed that SH photons are not detectable from the symmetric membranes. SH photons are absent because the bilayer is centrosymmetric along the normal direction (and thus within the dipole approximation no coherent SH photons are generated [73, 80]). In contrast, the asymmetric membrane does emit coherent SH photons due to the breaking of centrosymmetry. We showed in Chapter 4, where we changed the membrane composition, pH and ionic strength of the solution, and altered the polarization combinations of the beams showed that the SH membrane response arises from an anisotropic orientational ordering of water molecules (which is most pronounced in the PPP polarization combination) [80].

To incorporate voltage-gated ion channels in the DPhPC symmetric bilayer, we added alamethicin peptides to the solution adjacent to the top leaflet (Fig. 6.1C). To do so, $5\text{ }\mu\text{L}$ solution of alamethicin, dissolved in absolute ethanol, is added to the aqueous phase of the top leaflet corresponding to a final concentration of $0.10\text{ }\mu\text{g/mL}$. The aqueous phase consists of a pH neutral 100 mM KCl solution on either side of the membrane (unless otherwise stated). Ion channel activity is controlled by two Ag/AgCl electrodes that are placed on either side of the membrane.

6.3.2 The interfacial structure

We SH imaged the symmetric DPhPC bilayer with added alamethicin. Figure 6.1D shows SH images (560 ms acquisition time) of a bilayer with alamethicin ion channels that are subsequently opened (Fig. 6.1D, bottom row) and closed (Fig. 6.1D, top row) by the application of a 10 s voltage step (160 mV), obtained in the PPP polarization combination. It can be seen that the SH intensity increases when the channels are activated and decreases when the channels are deactivated. The intensity increase is localized and is related to the transport process. When the channels are opened, charges are transported through them. Since both the ions as well as the bilayer membrane are centrosymmetric these are likely not the source of the SH intensity change. The charge transport does result in a separation of charge between the two solutions, which should increase the capacitance of the membrane, and could also provide local electric fields that are strong enough to orient water molecules in and around the channel. These electric field oriented water molecules could be responsible for the increase in SH intensity observed in Fig. 6.1D.

To obtain more insight in the responsible molecular mechanism, we measured the timescale of the change in SH intensity after the opening and closing of a 160 mV 10 s voltage block pulse and compared it to the changes in capacitance. The block pulse voltage step occurs within $5\text{ }\mu\text{s}$. Figure 6.2A shows the time series of the integrated SH intensity over the whole image for a sequence of activation and deactivation cycles. The stimulus (green curve) indicates the timing when the channels are activated and when the channels are deactivated. Black dots are SH intensity data points, and the red and blue

Chapter 6. Spatiotemporal imaging of water in operating voltage-gated ion channels reveals the slow motion of interfacial ions

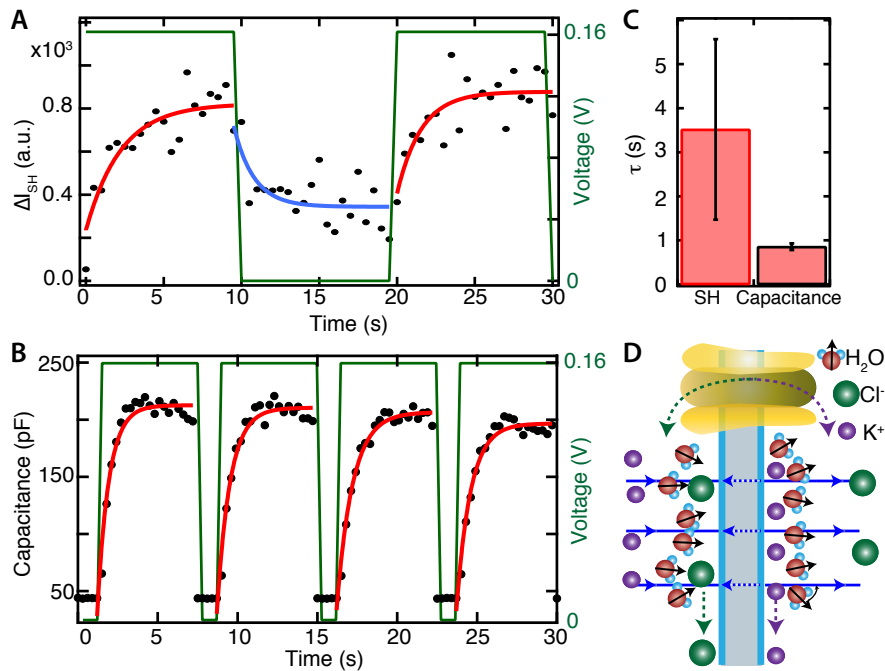


Figure 6.2 – Dynamic electrical and spatiotemporal imaging of voltage-gated ion channel activity in lipid membranes. (A) Time series of SH intensity (left axis) following the activation and deactivation of alamethicin channels (100 mM KCl, 0.1 $\mu\text{g}/\text{mL}$ alamethicin added to one side of the bilayer). The 10 s stimulus (green curve) indicates the timing when the channels are activated (160 mV) and when the channels are deactivated (0 mV). Each data point (black dot) represent the spatially averaged SH intensity (500 ms acquisition time) of the membrane. The data points in each activation and deactivation steps are piece-wise fitted with an exponential curve ($y_0 + Ae^{(t-t_0)/\tau}$), where τ is the time constant, y_0 the offset and A the magnitude. Red solid curves are exponential fits for activation steps while blue solid curves are exponential fits for deactivation steps. (B) Time series of the membrane capacitance following the activation and deactivation of alamethicin-induced channels for the same experimental conditions in (A). The stimulus (green curve) indicates the timing when the channels are activated (160 mV) or deactivated (0 mV). The length of the activation cycle is 6 seconds whereas the deactivation cycle is 1.5 seconds. Black points are data points while solid red lines are piecewise exponential fits for each activation cycle. (C) Average time constants for the activation cycle comparing the temporal change in SH intensity and capacitance measurements. (D) Schematic of the orientation of water at membrane interfaces. Field lines (blue) from both the positive and negative ions are shown with the corresponding ordering of interfacial water molecules.

lines represent piecewise exponential fits to the increase and decrease of the SH intensity. Figure 6.2B shows the change in capacitance (black data), for a 160 mV, 6 s block pulse. The capacitance increases as a function of time, up to a value of 220 pF, corresponding to a transport of $2.2 \cdot 10^8$ ions (averaged over the whole membrane). To quantify the timescale of this effect, we fitted a piecewise exponential (red solid line) for each activation cycle. Figure 6.2C shows a comparison of the timescales: ~ 3.5 s for the SH intensity increase and ~ 1 s for the change in capacitance. These are surprisingly slow processes, given the duration of the block pulse and the onset of current flow that both occur on microsecond timescales. However, we can understand what is happening on the molecular level by comparing the timescale of processes involved in the build-up of membrane-related charge and thus capacitance. First, upon switching the channels on, ions are transported at a rate of $\sim 10^8$ ions/s per channel [128, 132]. The number of open ion channels in our membrane can be estimated by

comparing the measured current (500 nA) for a given voltage gate to the known single channel ion transport (1.3 nS per channel, $V=160$ mV), resulting in a total number (N) of open ion channels of $2.4 \cdot 10^3$. For a membrane area of $\sim 3.8 \cdot 10^3 \mu\text{m}^2$, the average area per active ion channel is $\sim 2.1 \mu\text{m}^2$, meaning that there are ~ 0.1 channel per pixel (430 nm x 430 nm), on average. The total transport of ions is $\sim 2.4 \cdot 10^{11}$ changing the concentration by 2 pM, a negligible effect on the ionic solution. From the current measurements (50 nA) and capacitance change (220 pF) of Fig. 6.2B, we can estimate the number of ions that have accumulated at the membrane (500 nA, 2.2 nF). Since the interfacial charge, Q , the capacitance, C , and V the gated voltage are related by $Q = CV$, and the number of ions n per ion channel given by $n = Q/eN$, we obtain using the above numbers and $e=1.6 \cdot 10^{-19}$ C, $n=9.1 \cdot 10^5$ for the number of ions that are associated with the interfacial area around the ion channel. In addition, estimating the local concentration, c , to be given by $c = n/Ad$, with an area per channel (A) of $2.1 \cdot 10^6 \text{ nm}^2$, and a thickness (d) estimated by a Debye length (0.96 nm for 100 mM), we estimate the local concentration of ions in the electric double layer to become ~ 1.1 M in agreement with expectations [233].

The above analysis means that only a fraction of $\sim 10^{-4}$ of the ions that are transported across the membrane will modify the interfacial electric double layer region and contribute to the capacitance. With diffusion rates in the bulk given by $\sim 2800 \mu\text{m}^2/\text{s}$ for K^+ (calculated self-diffusion coefficient using MD simulations) [234], the transport / building up of charge would be on the order of $\sim 28.0 \text{ nm}^2/\text{s}$ ($2800 \cdot 10^{-8}$), meaning that the build-up of capacitive charge takes seconds, a remarkably slow process. That the SH intensity increase is on the same order of magnitude as the creation of a capacitive interfacial layer suggests that this too is related to the interfacial changes around the ion channels. The transport of ions in the channel and the creation of a charged layer at the interface adjacent to the channel by means of lateral diffusion of ions results in higher electric field strength and a higher number of oriented water molecules per channel, as illustrated in Fig. 6.2D. This will give rise to an increase in the SH intensity. It is possible that given the high interfacial concentration of ions there is also a contribution from interfacial ion pairs, but that will be a smaller contribution to the SH signal [233].

6.3.3 Crowding and spatiotemporal effects

So far, we have used averages from integrating the whole image. It is however expected that ion channel density may also play a role in how ion channels operate [218]. Next, we proceed to investigate the spatiotemporal dynamics of ion channel activity. Figure 6.3A shows the SH image of the change in SH intensity ($\Delta I(x, y)$) for a symmetric bilayer (500 mM KCl, pH neutral, 0.1 $\mu\text{g}/\text{mL}$ alamethicin) after an activation-deactivation cycle. $\Delta I(x, y) = I_{ON}(x, y) - I_{OFF}(x, y)$ and the subscripts ON/OFF refer to the temporally average recorded intensities (20 images, 1 second each) when the channels are activated (I_{ON} , $V=210$ mV) or deactivated (I_{OFF} , $V=0$) respectively. Note that, with a higher gating voltage and ionic strength in the solution, there will likely be more active ion channels in the membrane (see Fig. 6.1B). Figure 6.3A shows that the change in SH intensity is spatially heterogeneous. This distribution likely reflects the density of ion channels. To quantify the density of open channels, we use the image-averaged change in SH intensity, together with the image-averaged number of open ion channels (see Appendix 6.5 for details). The ratio of these numbers provides us with an average change in SH intensity per channel $\Delta I_{channel}$, allowing for the construction of images of the distribution of ion channels. This is shown in Fig. 6.3B. Spatial fluctuations in the density of open ion channels of up to 3 orders of magnitude per pixel are observed. We next examine if this has an influence on the local interfacial charging and structure. Figure 6.3C shows the time series of the spatially average SH intensity for three

Chapter 6. Spatiotemporal imaging of water in operating voltage-gated ion channels reveals the slow motion of interfacial ions

different regions of interests (ROIs) in Fig. 6.3A. The stimulus (green) shows the timing of the activation and deactivation cycles. It can be seen that the magnitude of the change in SH intensity, as well as the rate of increase, is different for the three ROIs and in all cases slower than what we observed in Fig. 6.2A. The latter observation can be explained by noting that these experiments are performed at higher salt concentrations (500 mM), leading to the slower build-up of the interfacial charge (due to crowding). Figure 6.3D shows the first activation cycle for the three ROIs (dashed rectangle in Fig. 6.3C). The exponential fits (given by the lines) indicate that there is a different time needed to build up the interfacial ionic-water layer for different ion channel densities: The time constant is longer when the change in SH intensity is higher and shorter when the change in SH intensity is lower. This means that in an area with many ion channels it takes more time to create a separation of ions. This is most likely caused by the presence of the other ion channels whose interfacial ion populations all have to compete for the same space. This crowding effect could be important in regulatory structures where the ion channel density is high.

6.4 Summary and Conclusions

SH imaging experiments were performed on operational voltage-gated alamethicin peptide ion channels inserted into a freestanding lipid membrane that is surrounded by aqueous solution on either side and having the same physiologically relevant salt concentration. The opening and closing of ion channels lead to changes in the SH contrast. These changes occur on the order of seconds. Combining capacitance and SH imaging, we identify the change in the orientation distribution of water molecules induced by the electric field gradients inside and in the vicinity of the pore as the main source of SH contrast. Only a fraction of 10^{-4} of the transported ions arrives at the hydrated membrane interface, which explains why the interfacial electrostatic changes are so slow. Finally, we quantify the spatiotemporal distribution of ion channels and record their activity during a gating cycle. Ion channels in high-density areas exhibit a lower rate of interfacial charge buildup, which is likely caused by crowding.

The lateral transport of ions is thought to be involved in the transport of action potentials, but it is not clear what the exact mechanism is. Our study shows that the timescale for ion transport along the membrane is taking place over seconds. This suggests that membrane lateral diffusion of ions is likely too slow to be directly involved in the propagation of action potentials. It may be important to induce local chemical changes, but it might not be related to the movement of electric signals that occurs on a sub-millisecond timescale.

6.5 Appendix

6.5.1 Estimation of the number of incorporated ion channels

Figure 6.4 shows the macroscopic conductance – voltage ($G - V$; with $G = I/V$) curve. The red line represents an exponential fit that is common for alamethicin ion channels [128, 134, 231, 125, 232, 132]. Macroscopic conductance (G) curves can be used to estimate the number of open ion channels (N), provided the single channel conductance γ is known. Assuming γ does not depend on V we have $G(V) = N(V)\gamma$. For the single ion channel conductance, we rely on a study [128], where the current through single pores was measured. In Ref. [128] the average single channel conductance was determined for alamethicin in a bilayer composed of phosphatidyl ethanolamine (PE) lipids, and with two different salt concentration: for 1 M NaCl solution, and $0.6 \cdot 10^{-7}$ g/mL total alamethicin

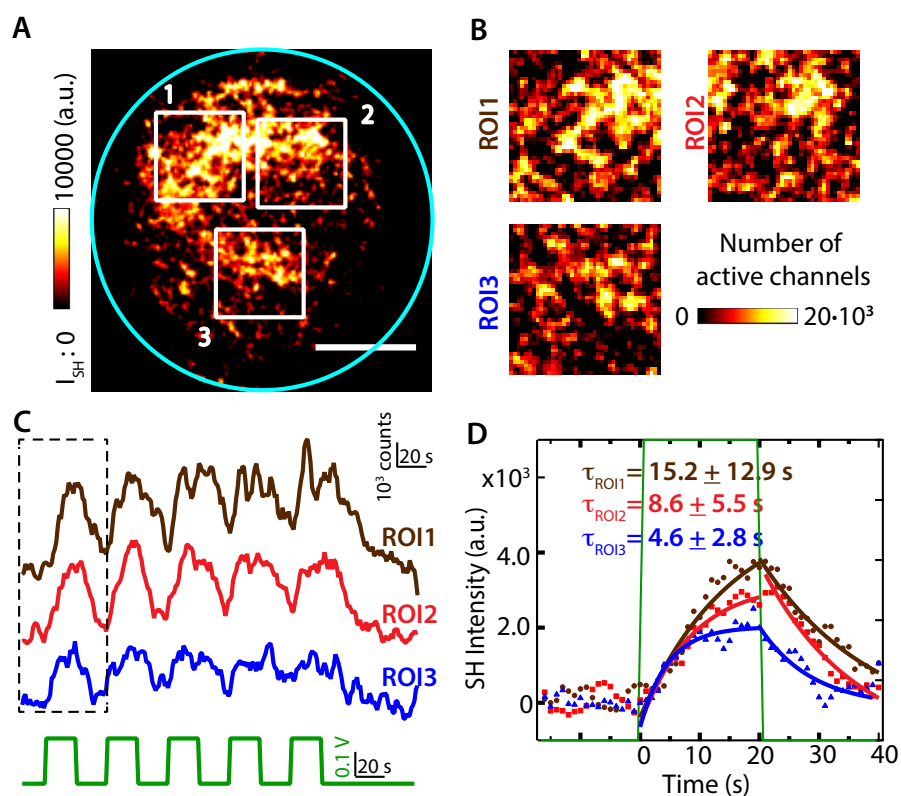


Figure 6.3 – Quantifying the spatiotemporal distribution of ion channel opening in membranes. (A) SH image of the change in intensity, $\Delta I(x, y)$ where $\Delta I(x, y) = I_{ON}(x, y) - I_{OFF}(x, y)$ and $I_{ON}(x, y)$ is the temporally average recorded intensities when the channels are activated ($V=210$ mV, 20 frames, 1 second each) and $I_{OFF}(x, y)$ is the temporally average recorded intensities when the channels are deactivated ($V=0$ mV, 20 frames, 1 second each). The solid squares define the region of interest (ROI) labeled 1, 2 and 3. The scale bar is $20 \mu\text{m}$. (B) Time series of the average SH intensity following the activation and deactivation of alamethicin channels for the corresponding region of interest defined in (A). Each curve represents the 5-point smooth average SH intensity per pixel (1 second acquisition time). The stimulus (green) shows the timing of the activation ($V=210$ mV) and deactivation ($V=0$ mV) cycles. The first activation step (dashed black rectangle in (B)) is plotted in detail in (C) and was fitted with an exponential curve for each ROI. The time constants from the fit are displayed. (D) Map of the number of open channels for three different ROI. The size of the ROI is $17 \mu\text{m} \times 17 \mu\text{m}$.

concentration, $\gamma = 2.5 \cdot 10^{-9}$ S and for 0.05 M NaCl solution, $2.0 \cdot 10^{-6}$ g/mL, $\gamma = 2.08 \cdot 10^{-10}$ S. Interpolating between these two single conductance values, at 0.5 M salt concentration, we get $\gamma = 1.3 \cdot 10^{-9}$ S. Using this number, we obtain the values displayed on the right axis of Fig. 6.4. For a 200 mV potential difference, the total number of open ion channels is $4 \cdot 10^7$ and given our membrane area of $\sim 100 \mu\text{m}^2$, the average area per ion channel is $\sim 200 \text{nm}^2$, meaning there are on average ~ 900 opened ion channels per pixel ($430 \text{nm} \times 430 \text{nm}$).

Chapter 6. Spatiotemporal imaging of water in operating voltage-gated ion channels reveals the slow motion of interfacial ions

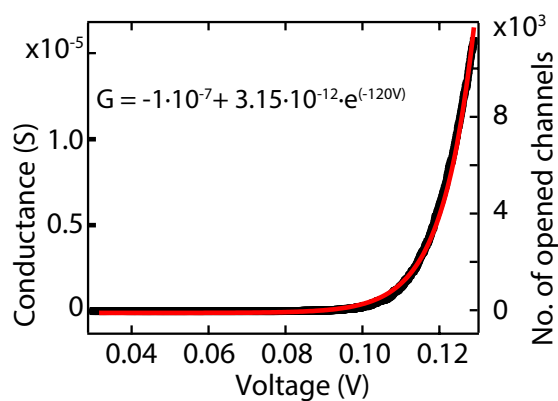


Figure 6.4 – Macroscopic conductance-voltage curve of alamethicin channel in 500 mM KCl. The conductance was derived from the positive stimulus of Fig. 6.1B. Data points (black) are fitted with an exponential curve (solid red line). The right axis shows the calculated number of opened channels using the average single pore conductance from Ref 14. (1.3 nS per channel)

7 Summary & Outlook

In this thesis, high throughput wide-field second harmonic (SH) microscopy was used to image water-membrane interactions at sub-second time scale to follow the spatiotemporal evolution of membrane fluctuations in freestanding lipid membranes. These fluctuations lead to diversification of membrane properties, and couples local chemical interactions with microscopic behavior. For example, changes in local electrical gradient across the bilayer lead to changes in membrane curvature. The observations in this thesis highlight the multi-scale response of lipid membranes to external stimuli and vice versa. Such effects potentially play an important role in membrane structuring, signaling, and transport. On a more fundamental level, the influence of structural and temporal heterogeneity needs to be included in biochemical, physical and molecular models of membranes.

7.0.1 Summary

In chapter 2, we improved the throughput of SH imaging by implementing changes in the optical layout and laser source. We achieved 2-3 orders of magnitude improvement in the imaging throughput by employing a wide-field geometry and medium repetition rate laser source in combination with gated detection. The pulse duration was measured directly at the sample and was not distorted. Furthermore, the optical layout allowed probing of 8 possible polarization combinations. Moreover, we integrated the apparatus to form freestanding lipid membranes for simultaneous electrical and optical characterization of membranes. The apparatus to form freestanding membranes. The ease of modifying the membrane environment coupled with surface-selective, label-free and high throughput SH imaging paved the way for dynamic imaging of lipid membranes.

In chapter 3, we investigated the interaction of oil with freestanding lipid bilayers in aqueous solution using second harmonic and white-light imaging. We found that differences in oil structure lead to differences in membrane structure. We showed that the curvature of monolayers at the edge of the Teflon film of freestanding bilayers prepared with hexadecane is higher compared with squalene and that hexadecane formed a narrower annulus compared with squalene. These findings indicate that less hexadecane was present within the bilayer. Conversely, it seems there was a higher quantity of squalene remaining in the bilayer. We tracked the diffusion of excess oil droplets within the bilayer and show that hexadecane droplets follow directed diffusion, moving from the center of the bilayer to the annulus, with a diffusion coefficient of $1.8 \mu\text{m}^2/\text{s}$, similar to single lipids, whereas squalene show no directed motion with a diffusion coefficient of $0.16 \mu\text{m}^2/\text{s}$, similar to lipid domains. We proposed that this difference was caused by the difference in structure: hexadecane can stay within a single leaflet

Chapter 7. Summary & Outlook

and diffuse through the liquid phase of the lipids. Squalene on the other hand is bigger than a single leaflet and also more branched, so it will couple to both leaflets and move slower.

In chapter 4, we showed in a series of experiments involving symmetric and asymmetric free-standing lipid membranes, and changes in the ionic and pH content of adjacent solutions, that the non-resonant response of water can be SH imaged on sub-second time scales. This water response has a nonrandom orientation, as it was oriented by the charge-dipole interactions between charged lipid head groups and water dipoles. We used this water response as a contrast mechanism to probe domain diffusion of DPPS-rich domains and to compute the electrostatic membrane potential, and map its dependence on an externally applied field. We showed that the average membrane potential follows the quadratic dependence on external bias that was modeled by nonlinear optical theory. However, individual images showed dynamic spatiotemporal fluctuations on the order of ~ 100 mV.

In chapter 5, we probed the interactions of divalent cations with water and negatively charged freestanding lipid bilayers and showed that at physiological concentration, Ca^{2+} , Ba^{2+} and Mg^{2+} induce short-lived (<500 ms) and micron sized ($\sim 1.5 \mu\text{m}$) domains of ordered interfacial water. We converted the SH intensity into membrane hydration free energy, and membrane-ion binding dissociation constant maps. We obtained trends in the order $\text{Ca}^{2+} > \text{Mg}^{2+} > \text{Ba}^{2+}$, for all quantities. We quantified the ion binding dissociation constants and showed domain values that deviate up to 4 orders of magnitude from average binding dissociation constants. The transient structural domains exhibited membrane potential fluctuations of up to -386 mV (with $\Delta G = 28.6$ kT) induced strain in the membrane resulting in temporal and spatial variations in membrane curvature.

In chapter 6, we performed spatiotemporal SH imaging of operational voltage-gated alamethicin ion channels in freestanding lipid membranes surrounded by aqueous solution on either side and having the same physiologically relevant salt concentration. We showed that the opening and closing of ion channels lead to the increase and decrease of SH intensity. Combining SH imaging with capacitance measurements, we attributed the changes in SH intensity to the orientational distribution of water molecules induced by electric field gradients. Only a fraction, that is, 10^{-4} of the transported ions arrives at the hydrated membrane interface, leading to interfacial electrostatic changes on the time scale of a second. We quantified the spatiotemporal distribution of ion channels and recorded their activity during gating. Regions with high-density of ion channels exhibit a lower rate of interfacial charge buildup, which is likely caused by crowding.

7.0.2 Outlook

The properties of cells highly depend on the structural and chemical properties of lipid membranes. Several studies have focused on studying the hydrophobic core of the bilayer and have provided information about lipid-lipid interactions but have ignored hydration, electrostatic and hydrogen bonding interactions and the influence of the electric double layer. This thesis is a step towards understanding the effects of these interactions and understand their spatiotemporal evolution in real membranes.

In chapter 3, we showed that differences in oil structure and the related interaction mechanisms with lipids are important when considering what type of bilayer system to be used. In biological systems, it maybe important to consider the implications of lipid droplets in the structuring of membranes.

In chapter 4, the imaging method can be extended to live neurons to map membrane potential.

This was indeed demonstrated in our latest measurements of neuronal membrane potential (see Dider et al., Ref [235]), without the need to physically patch the cells, thus providing a future noninvasive and clinically viable method to map membrane potentials.

In chapter 5, we showed that aside from having a local specific interaction with lipids, divalent ions also influence the chemical, electrical and mechanical properties of membrane leading to a diversification of membrane environments. These effects provide and a mechanism for coupling local chemical interactions with microscopic behavior that could potentially play an important role in membrane protein interactions, important for structuring, signaling, and transport.

In chapter 6, we showed that the time scale for ion transport along the membrane is taking place over seconds. The lateral transport of ions is thought to be involved in the transport of action potentials, but it is not clear what the exact mechanism is. Our study suggests a more complex mechanism for the propagation of action potentials that may not be directly related to lateral diffusion of ions.

Electrostatic and hydrogen bonding interactions are at the core of many important processes in biochemistry, as such a wide variety of applications are foreseen. For example, the complex interaction between cations, surface charges, polar and hydrophobic groups in membrane fusion, in signaling through ion specific channels in synapses, the folding of proteins [95, 96], the formation of secondary structures [97, 98] and the binding of proteins to membrane, for example the binding of G-coupled protein receptors to membranes. Furthermore, SH imaging is directly applicable to functional studies of membrane asymmetry such as protein induce membrane curvature. Moreover, a variety of diseases are related to the dysfunction of ion channels as described in the introduction (see Chapter 1.4.4). The use of SH imaging as spatiotemporal diagnosis for the development of drug-related ion-channel diseases may prove crucial in the field of medicine and biology. Lastly, it may be expected that the interfacial hydration and interactions in the electric double layer might be connected to biochemical processes in a more complex way than by providing a mean field background to the interactions of lipids.

8 List of Publications

This thesis is based on the following publications:

Chapter 2 and Chapter 4

O. B. Tarun, C. Hanneschläger, P. Pohl, S. Roke. Proceedings of the National Academy of Sciences, 115(16), 4081 (2018).

C. Macias-Romero, M. E. P. Didier, P. Jourdain, P. Marquet, P. Magistretti, **O. B. Tarun**, V. Zubkovs, A. Radenovic, S. Roke. Optics express 22, 31102-31112 (2014).

Chapter 3

O. B. Tarun, M. Yu Eremchev, S. Roke. Langmuir, 34, 11305-11310 (2018).

Chapter 5

O. B. Tarun, H. I. Okur, P. Rangamani, S. Roke. Divalent ions induce transient domains of interfacial ordered water in lipid membranes. Submitted (2018)

Chapter 6

O. B. Tarun, M.Yu. Eremchev, A. Radenovic, and S. Roke. Spatiotemporal imaging of water in operating voltage-gated ion channels reveals the slow motion of interfacial ions. Submitted (2018).

Additional publications by the same author:

M. Didier, **O. B. Tarun**, P. Jourdain, P. Magistretti, S. Roke. Nature Communications, 9(1), 5287 (2018).

Bibliography

- [1] Philip Ball. Water as an active constituent in cell biology. *Chemical Reviews*, 108(1):74–108, 2008.
- [2] David Deamer. The role of lipid membranes in life's origin. *Life*, 7(1):5, 2017. life-07-00005[PII] 28106741[pmid] Life (Basel).
- [3] Julian Lewis Martin Raff Keith Roberts Bruce Alberts, Alexander Johnson and Peter Walter. *Molecular Biology of the Cell, 4th edition*. Garland Science, 2002.
- [4] Pietro Cicuta, Sarah L. Keller, and Sarah L. Veatch. Diffusion of liquid domains in lipid bilayer membranes. *The Journal of Physical Chemistry B*, 111(13):3328–3331, 2007.
- [5] Marcus D. Collins and Sarah L. Keller. Tuning lipid mixtures to induce or suppress domain formation across leaflets of unsupported asymmetric bilayers. *Proceedings of the National Academy of Sciences*, 105(1):124–128, 2008.
- [6] S. L. Veatch, I. V. Polozov, K. Gawrisch, and S. L. Keller. Liquid domains in vesicles investigated by nmr and fluorescence microscopy. *Biophysical journal*, 86(5):2910–2922, 2004.
- [7] Sarah L. Veatch and Sarah L. Keller. Seeing spots: Complex phase behavior in simple membranes. *Biochimica et Biophysica Acta (BBA) - Molecular Cell Research*, 1746(3):172–185, 2005.
- [8] O. Bakht, P. Pathak, and E. London. Effect of the structure of lipids favoring disordered domain formation on the stability of cholesterol-containing ordered domains (lipid rafts): identification of multiple raft-stabilization mechanisms. *Biophys J*, 93(12):4307–18, 2007. Bakht, Omar Pathak, Priyadarshini London, Erwin eng GM 48596/GM/NIGMS NIH HHS/ Research Support, N.I.H., Extramural 2007/09/04 09:00 Biophys J. 2007 Dec 15;93(12):4307-18. Epub 2007 Aug 31.
- [9] C. Dietrich, L. a Bagatolli, Z. N. Volovyk, N. L. Thompson, M. Levi, K. Jacobson, and E. Gratton. Lipid rafts reconstituted in model membranes. *Biophysical journal*, 80(3):1417–1428, 2001.
- [10] Jacob N. Israelachvili. *Intermolecular and Surface Forces. 3rd edition*. Elsevier, 2011.

Bibliography

- [11] Sylvie Roke and Grazia Gonella. Nonlinear light scattering and spectroscopy of particles and droplets in liquids. *Annu. Rev. Phys. Chem.*, 63(1):353–378, 2012.
- [12] Alireza Mashaghi, Samaneh Mashaghi, Ilya Reviakine, Ron M. a Heeren, Vahid Sandogh-dar, and Mischa Bonn. Label-free characterization of biomembranes: from structure to dynamics. *Chemical Society reviews*, 43(3):887–900, 2014.
- [13] Sandhya Gopalakrishnan, Dingfang Liu, Heather C. Allen, Margaret Kuo, and Mary Jane Shultz. Vibrational spectroscopic studies of aqueous interfaces: salts, acids, bases, and nanodrops. *Chemical Reviews*, 106(4):1155–1175, 2006.
- [14] Paul A. Covert and Dennis K. Hore. Geochemical insight from nonlinear optical studies of mineral–water interfaces. *Annual Review of Physical Chemistry*, 67(1):233–257, 2016.
- [15] Yanjie Zhang and Paul S. Cremer. Interactions between macromolecules and ions: the hofmeister series. *Current Opinion in Chemical Biology*, 10(6):658–663, 2006.
- [16] O. Alvarez and R. Latorre. Voltage-dependent capacitance in lipid bilayers made from monolayers. *Biophysical journal*, 21(1):1–17, 1978.
- [17] Thomas Heimburg. The capacitance and electromechanical coupling of lipid membranes close to transitions: The effect of electrostriction. *Biophysical Journal*, 103(5):918–929, 2012.
- [18] Uwe Peterson, David a Mannoek, Ruthven N. a H. Lewis, Peter Pohl, Ronald N. McEl-haney, and Elena E. Pohl. Origin of membrane dipole potential: Contribution of the phospholipid fatty acid chains. *Chemistry and Physics of Lipids*, 117(1-2):19–27, 2002.
- [19] Robert J. Hunter. *Foundations of Colloid Science*. Oxford University Press, 2001.
- [20] S. J. Singer and Garth L. Nicolson. The fluid mosaic model of the structure of cell membranes. *Science*, 175(4023):720, 1972.
- [21] Kai Simons and Elina Ikonen. Functional rafts in cell membranes. *Nature*, 387(6633):569–572, 1997. 10.1038/42408.
- [22] Howard Brockman. Lipid monolayers: why use half a membrane to characterize protein-membrane interactions? *Current Opinion in Structural Biology*, 9(4):438–443, 1999.
- [23] Vladimir M. Kaganer, Helmuth Möhwald, and Pulak Dutta. Structure and phase transitions in langmuir monolayers. *Reviews of Modern Physics*, 71(3):779–819, 1999. RMP.
- [24] Sylvie Roke, Juleon Schins, Michiel Müller, and Mischa Bonn. Vibrational spectroscopic investigation of the phase diagram of a biomimetic lipid monolayer. *Physical Review Letters*, 90(12):128101–128101, 2003.
- [25] R. Lipowsky Sackmann and E. *Structure and dynamics of membranes, Handbook of biological physics*. Elsevier Science, New York, 1995.

- [26] P. Guyot-Sionnest, J. H. Hunt, and Y. R. Shen. Sum-frequency vibrational spectroscopy of a langmuir film: Study of molecular orientation of a two-dimensional system. *Physical Review Letters*, 59(14):1597–1600, 1987. PRL.
- [27] Sylvie Roke, Wim G. Roeterdink, Judith E. G. J. Wijnhoven, Andrei V. Petukhov, Aart W. Kleyn, and Mischa Bonn. Vibrational sum frequency scattering from a submicron suspension. *Physical Review Letters*, 91(25):258302, 2003. PRL.
- [28] Marc C. Gurau, Edward T. Castellana, Fernando Albertorio, Sho Kataoka, Soon-Mi Lim, Richard D. Yang, and Paul S. Cremer. Thermodynamics of phase transitions in langmuir monolayers observed by vibrational sum frequency spectroscopy. *Journal of the American Chemical Society*, 125(37):11166–11167, 2003.
- [29] Jonathan F. D. Liljeblad, Vincent Bulone, Eric Tyrode, Mark W. Rutland, and C. Magnus Johnson. Phospholipid monolayers probed by vibrational sum frequency spectroscopy: Instability of unsaturated phospholipids. *Biophysical Journal*, 98(10):L50–L52, 2010.
- [30] Xiangke Chen, Wei Hua, Zishuai Huang, and Heather C. Allen. Interfacial water structure associated with phospholipid membranes studied by phase-sensitive vibrational sum frequency generation spectroscopy. *Journal of the American Chemical Society*, 132(32):11336–11342, 2010.
- [31] Gang Ma and Heather C. Allen. Dppc langmuir monolayer at the airwater interface: probing the tail and head groups by vibrational sum frequency generation spectroscopy. *Langmuir*, 22(12):5341–5349, 2006.
- [32] Mischa Bonn, Sylvie Roke, Otto Berg, Juurlink, Amalia Stamouli, and Michiel Müller. A molecular view of cholesterol-induced condensation in a lipid monolayer. *The Journal of Physical Chemistry B*, 108(50):19083–19085, 2004.
- [33] G. Denisov, S. Wanaski, P. Luan, M. Glaser, and S. McLaughlin. Binding of basic peptides to membranes produces lateral domains enriched in the acidic lipids phosphatidylserine and phosphatidylinositol 4,5-bisphosphate: An electrostatic model and experimental results. *Biophysical Journal*, 74(2):731–744, 1998.
- [34] Dietmar Möbius. Morphology and structural characterization of organized monolayers by brewster angle microscopy. *Current Opinion in Colloid Interface Science*, 3(2):137–142, 1998.
- [35] Dirk Hoenig and Dietmar Moebius. Direct visualization of monolayers at the air-water interface by brewster angle microscopy. *The Journal of Physical Chemistry*, 95(12):4590–4592, 1991.
- [36] Michalakis Savva, Balasubramanian Sivakumar, and Bilge Selvi. The conventional langmuir trough technique as a convenient means to determine the solubility of sparingly soluble surface active molecules: Case study cholesterol. *Colloids and surfaces. A*,

Bibliography

- Physicochemical and engineering aspects*, 325(1-2):1–6, 2008. 19609337[pmid] Colloids Surf A Physicochem Eng Asp.
- [37] Yixing Chen, Kailash C. Jena, Cornelis Lütgebaucks, Halil I. Okur, and Sylvie Roke. Three dimensional nano “langmuir trough” for lipid studies. *Nano Letters*, 15(8):5558–5563, 2015.
- [38] Joel M. Goodman. The gregarious lipid droplet. *The Journal of Biological Chemistry*, 283(42):28005–28009, 2008.
- [39] Qiang Gao and Joel M. Goodman. The lipid droplet—a well-connected organelle. *Frontiers in Cell and Developmental Biology*, 3:49, 2015. 26322308[pmid] Front Cell Dev Biol.
- [40] A. Rachid Thiam, Robert V. Farese, and Tobias C. Walther. The biophysics and cell biology of lipid droplets. *Nature reviews. Molecular cell biology*, 14(12):775–786, 2013. 24220094[pmid] Nat Rev Mol Cell Biol.
- [41] Ilya Reviakine and Alain Brisson. Formation of supported phospholipid bilayers from unilamellar vesicles investigated by atomic force microscopy. *Langmuir*, 16(4):1806–1815, 2000.
- [42] Ralf P. Richter, Rémi Bérat, and Alain R. Brisson. Formation of solid supported lipid bilayers an integrated view. *Langmuir*, 22(8):3497–3505, 2006.
- [43] Marie-Paule Mingeot-Leclercq, Magali Deleu, Robert Brasseur, and Yves F. Dufrêne. Atomic force microscopy of supported lipid bilayers. *Nature Protocols*, 3:1654, 2008.
- [44] Mary L. Kraft, Peter K. Weber, Marjorie L. Longo, Ian D. Hutcheon, and Steven G. Boxer. Phase separation of lipid membranes analyzed with high-resolution secondary ion mass spectrometry. *Science*, 313(5795):1948, 2006.
- [45] Ralf P. Richter, Nicolas Maury, and Alain R. Brisson. On the effect of the solid support on the interleaflet distribution of lipids in supported lipid bilayers. *Langmuir*, 21(1):299–304, 2005.
- [46] Tobias Baumgart, Samuel T. Hess, and Watt W. Webb. Imaging coexisting fluid domains in biomembrane models coupling curvature and line tension. *Nature*, 425:821, 2003.
- [47] Gerald W. Feigenson. Phase boundaries and biological membranes. *Annual Review of Biophysics and Biomolecular Structure*, 36(1):63–77, 2007.
- [48] V. Kiessling, C. Wan, and L. K. Tamm. Domain coupling in asymmetric lipid bilayers. *Biochim. Biophys. Acta, Biomembr.*, 1788(1):64–71, 2009.
- [49] M. Montal and P. Mueller. Formation of bimolecular membranes from lipid monolayers and a study of their electrical properties. *Proceedings of the National Academy of Sciences of the United States of America*, 69(12):3561–3566, 1972.

- [50] Matthew A. Kriech and John C. Conboy. Imaging chirality with surface second harmonic generation microscopy. *Journal of the American Chemical Society*, 127(9):2834–2835, 2005.
- [51] Trang T. Nguyen and John C. Conboy. High-throughput screening of drug–lipid membrane interactions via counter-propagating second harmonic generation imaging. *Analytical Chemistry*, 83(15):5979–5988, 2011.
- [52] Ryan S. Ries, Hyeon Choi, Rikard Blunck, Francisco Bezanilla, and James R. Heath. Black lipid membranes: visualizing the structure, dynamics, and substrate dependence of membranes. *The Journal of Physical Chemistry B*, 108(41):16040–16049, 2004.
- [53] Kai Simons and Winchil L. C. Vaz. Model systems, lipid rafts, and cell membranes. *Annual review of biophysics and biomolecular structure*, 33:269–295, 2004.
- [54] Dylan Owen and Katharina Gaus. Imaging lipid domains in cell membranes: the advent of super-resolution fluorescence microscopy. *Frontiers in Plant Science*, 4:503, 2013.
- [55] Sang-Hee Shim, Chenglong Xia, Guisheng Zhong, Hazen P. Babcock, Joshua C. Vaughan, Bo Huang, Xun Wang, Cheng Xu, Guo-Qiang Bi, and Xiaowei Zhuang. Super-resolution fluorescence imaging of organelles in live cells with photoswitchable membrane probes. *Proceedings of the National Academy of Sciences*, 109(35):13978–13983, 2012.
- [56] Christian Eggeling, Christian Ringemann, Rebecca Medda, Gunter Schwarzmann, Konrad Sandhoff, Svetlana Polyakova, Vladimir N. Belov, Birka Hein, Claas von Middendorff, Andreas Schonle, and Stefan W. Hell. Direct observation of the nanoscale dynamics of membrane lipids in a living cell. *Nature*, 457(7233):1159–1162, 2009. 10.1038/nature07596.
- [57] Dylan M. Owen, Carles Rentero, Jérémie Rossy, Astrid Magenau, David Williamson, Macarena Rodriguez, and Katharina Gaus. Palm imaging and cluster analysis of protein heterogeneity at the cell surface. *Journal of Biophotonics*, 3(7):446–454, 2010.
- [58] Prabuddha Sengupta, Tijana Jovanovic-Taliman, Dunja Skoko, Malte Renz, Sarah L. Veatch, and Jennifer Lippincott-Schwartz. Probing protein heterogeneity in the plasma membrane using palm and pair correlation analysis. *Nature Methods*, 8:969, 2011.
- [59] Tobias Baumgart, Geoff Hunt, Elaine R. Farkas, Watt W. Webb, and Gerald W. Feigenson. Fluorescence probe partitioning between lo/l_d phases in lipid membranes. *Biochimica et Biophysica Acta (BBA) - Biomembranes*, 1768(9):2182–2194, 2007.
- [60] Yee-Hung M. Chan and Steven G. Boxer. Model membrane systems and their applications. *Current Opinion in Chemical Biology*, 11(6):581–587, 2007.
- [61] Michael C. Howland, Alan W. Szmodis, Babak Sanii, and Atul N. Parikh. Characterization of physical properties of supported phospholipid membranes using imaging ellipsometry at optical wavelengths. *Biophysical Journal*, 92(4):1306–1317, 2007.

Bibliography

- [62] Gabrielle de Wit, John S. H. Danial, Philipp Kukura, and Mark I. Wallace. Dynamic label-free imaging of lipid nanodomains. *Proceedings of the National Academy of Sciences*, 112(40):12299–12303, 2015.
- [63] Eric O. Potma, Wim P. de Boeij, Peter J. M. van Haastert, and Douwe A. Wiersma. Real-time visualization of intracellular hydrodynamics in single living cells. *Proceedings of the National Academy of Sciences*, 98(4):1577–1582, 2001.
- [64] Hilde A. Rinia, Koert N. J. Burger, Mischa Bonn, and Michiel Mu. Quantitative label-free imaging of lipid composition and packing of individual cellular lipid droplets using multiplex cars microscopy. 95(10):4908–4914, 2008.
- [65] L. Li and Ji-Xin Cheng. Label-free coherent anti-stokes raman scattering imaging of coexisting lipid domains in single bilayers. *The Journal of Physical Chemistry B*, 112(6):1576–1579, 2008.
- [66] Sapun H. Parekh, Young Jong Lee, Khaled A. Aamer, and Marcus T. Cicerone. Label-free cellular imaging by broadband coherent anti-stokes raman scattering microscopy. *Biophysical Journal*, 99(8):2695–2704, 2010.
- [67] Christian W. Freudiger, Wei Min, Brian G. Saar, Sijia Lu, Gary R. Holtom, Chengwei He, Jason C. Tsai, Jing X. Kang, and X. Sunney Xie. Label-free biomedical imaging with high sensitivity by stimulated raman scattering microscopy. *Science*, 322(5909):1857, 2008.
- [68] Almar F. Palonpon, Mikiko Sodeoka, and Katsumasa Fujita. Molecular imaging of live cells by raman microscopy. *Current Opinion in Chemical Biology*, 17(4):708–715, 2013.
- [69] Bin Liu, Hyeon Jeong Lee, Delong Zhang, Chien-Sheng Liao, Na Ji, Yuanqin Xia, and Ji-Xin Cheng. Label-free spectroscopic detection of membrane potential using stimulated raman scattering. *Applied Physics Letters*, 106(17):173704, 2015.
- [70] Hyeon Jeong Lee, Delong Zhang, Ying Jiang, Xiangbing Wu, Pei-Yu Shih, Chien-Sheng Liao, Brittani Bungart, Xiao-Ming Xu, Ryan Drenan, Edward Bartlett, and Ji-Xin Cheng. Label-free vibrational spectroscopic imaging of neuronal membrane potential. *The Journal of Physical Chemistry Letters*, 8(9):1932–1936, 2017.
- [71] P. A. Franken, A. E. Hill, C. W. Peters, and G. Weinreich. Generation of optical harmonics. *Physical Review Letters*, 7(4):118–119, 1961. PRL.
- [72] Alex G. Lambert, Paul B. Davies, and David J. Neivandt. Implementing the theory of sum frequency generation vibrational spectroscopy: A tutorial review. *Applied Spectroscopy Reviews*, 40(2):103–145, 2005.
- [73] Robert W. Boyd. *Nonlinear Optics, Third Edition*. Academic Press, 2008.
- [74] N. Bloembergen and P. S. Pershan. Light waves at the boundary of nonlinear media. *Physical Review*, 128(2):606–622, 1962. PR.

- [75] Fielding Brown and Masahiro Matsuoka. Effect of adsorbed surface layers on second-harmonic light from silver. *Physical Review*, 185(3):985–987, 1969. PR.
- [76] H. Wang, E. C. Y. Yan, E. Borguet, and K. B. Eisenthal. Second harmonic generation from the surface of centrosymmetric particles in bulk solution. *Chemical Physics Letters*, 259(1):15–20, 1996.
- [77] S. Ong, X. Zhao, and K. Eisenthal. Polarization of water molecules at a charged interface : second harmonic studies of the silica / water interface. *Chemical Physics Letters*, 191(3):327–335, 1992.
- [78] Cornelis Lütgebaucks, Grazia Gonella, and Sylvie Roke. Optical label-free and model-free probe of the surface potential of nanoscale and microscopic objects in aqueous solution. *Physical Review B*, 94(19):195410, 2016. PRB.
- [79] Cornelis Lütgebaucks, Carlos Macias-Romero, and Sylvie Roke. Characterization of the interface of binary mixed dopc:dops liposomes in water: The impact of charge condensation. *The Journal of Chemical Physics*, 146(4):044701, 2017.
- [80] Orly B. Tarun, Christof Hanneschläger, Peter Pohl, and Sylvie Roke. Label-free and charge-sensitive dynamic imaging of lipid membrane hydration on millisecond time scales. *Proceedings of the National Academy of Sciences*, 115(16):4081, 2018.
- [81] Yixing Chen, Halil I. Okur, Nikolaos Gomopoulos, Carlos Macias-Romero, Paul S. Cremer, Poul B. Petersen, Gabriele Tocci, David M. Wilkins, Chungwen Liang, Michele Ceriotti, and Sylvie Roke. Electrolytes induce long-range orientational order and free energy changes in the h-bond network of bulk water. *Science Advances*, 2(4), 2016.
- [82] W. Denk, J. H. Strickler, and W. W. Webb. Two-photon laser scanning fluorescence microscopy. *Science*, 248(4951):73, 1990.
- [83] Jeff Hecht. Short history of laser development. volume 49, page 23. SPIE, 2010.
- [84] Daniel A. Dombeck, Karl A. Kasischke, Harshad D. Vishwasrao, Martin Ingelsson, Bradley T. Hyman, and Watt W. Webb. Uniform polarity microtubule assemblies imaged in native brain tissue by second-harmonic generation microscopy. *Proceedings of the National Academy of Sciences*, 100(12):7081, 2003.
- [85] Boaz A. Nemet, Volodymyr Nikolenko, and Rafael Yuste. Second harmonic imaging of membrane potential of neurons with retinal. *Journal of Biomedical Optics*, 9(5):873–881, 2004. 10.1117/1.1783353.
- [86] M. Nuriya, J. Jiang, B. Nemet, K. B. Eisenthal, and R. Yuste. Imaging membrane potential in dendritic spines. *Proceedings of the National Academy of Sciences of the United States of America*, 103(3):786–790, 2006. Nuriya, M Jiang, J Nemet, B Eisenthal, KB Yuste, R.

Bibliography

- [87] J. I. Dadap, X. F. Hu, M. Russell, J. G. Ekerdt, J. K. Lowell, and M. C. Downer. Analysis of second-harmonic generation by unamplified, high-repetition-rate, ultrashort laser pulses at si(001) interfaces. *IEEE Journal of Selected Topics in Quantum Electronics*, 1(4):1145–1155, 1995.
- [88] Carlos Macias-Romero, Igor Nahalka, Halil I. Okur, and Sylvie Roke. Optical imaging of surface chemistry and dynamics in confinement. *Science*, 357(6353):784, 2017.
- [89] Drew Marquardt, Barbara Geier, and Georg Pabst. Asymmetric lipid membranes: Towards more realistic model systems. *Membranes*, 5(2), 2015.
- [90] Valerie A. Fadok and Peter M. Henson. Apoptosis: Getting rid of the bodies. *Current Biology*, 8(19):R693–R695, 1998.
- [91] F. Hofmeister. Zur lehre von der wirkung der salze. *Naunyn-Schmiedeberg's Arch. Pharmacol*, 24:247–260, 1888.
- [92] F. Hofmeister. Zur lehre von der wirkung der salze. *Naunyn-Schmiedeberg's Arch. Pharmacol*, 25:130., 1888.
- [93] Werner Kunz. *Specific Ion Effects*. WORLD SCIENTIFIC, 2009. doi:10.1142/7261.
- [94] Halil I. Okur, Jana Hladílková, Kelvin B. Rembert, Younhee Cho, Jan Heyda, Joachim Dzubiella, Paul S. Cremer, and Pavel Jungwirth. Beyond the hofmeister series: Ion-specific effects on proteins and their biological functions. *The Journal of Physical Chemistry B*, 121(9):1997–2014, 2017.
- [95] Juris Kiskis, Istvan Horvath, Pernilla Wittung-Stafshede, and Sandra Rocha. Unraveling amyloid formation paths of parkinson's disease protein -synuclein triggered by anionic vesicles. *Quarterly Reviews of Biophysics*, 50:e3, 2017.
- [96] Wei Liu, Li Fu, Zhuguang Wang, Zahra Sohrabpour, Xiaobai Li, Yuting Liu, Hong-fei Wang, and Elsa C. Y. Yan. Two dimensional crowding effects on protein folding at interfaces observed by chiral vibrational sum frequency generation spectroscopy. *Physical Chemistry Chemical Physics*, 20(35):22421–22426, 2018.
- [97] Elsa C. Y. Yan, Zhuguang Wang, and Li Fu. Proteins at interfaces probed by chiral vibrational sum frequency generation spectroscopy. *The Journal of Physical Chemistry B*, 119(7):2769–2785, 2015.
- [98] Ethan A. Perets and Elsa C. Y. Yan. The h₂o helix: The chiral water superstructure surrounding dna. *ACS Central Science*, 3(7):683–685, 2017.
- [99] Kelvin B. Rembert, Jana Paterová, Jan Heyda, Christian Hilty, Pavel Jungwirth, and Paul S. Cremer. Molecular mechanisms of ion-specific effects on proteins. *Journal of the American Chemical Society*, 134(24):10039–10046, 2012.

- [100] Xin Chen, Tinglu Yang, Sho Kataoka, and Paul S. Cremer. Specific ion effects on interfacial water structure near macromolecules. *Journal of the American Chemical Society*, 129(40):12272–12279, 2007.
- [101] P. Viswanath, A. Aroti, H. Motschmann, and E. Leontidis. Vibrational sum frequency generation spectroscopic investigation of the interaction of thiocyanate ions with zwitterionic phospholipid monolayers at the air/water interface. *The Journal of Physical Chemistry B*, 113(44):14816–14823, 2009.
- [102] Jinsuk Song, John Franck, Philip Pincus, Mahn Won Kim, and Songi Han. Specific ions modulate diffusion dynamics of hydration water on lipid membrane surfaces. *Journal of the American Chemical Society*, 136(6):2642–2649, 2014.
- [103] Diana Smetters, Ania Majewska, and Rafael Yuste. Detecting action potentials in neuronal populations with calcium imaging. *Methods*, 18(2):215–221, 1999.
- [104] Tadanao Ito and Shun-Ichi Ohnishi. Ca²⁺-induced lateral phase separations in phosphatidic acid-phosphatidylcholine membranes. *Biochimica et Biophysica Acta (BBA) - Biomembranes*, 352(1):29–37, 1974.
- [105] D. Papahadjopoulos and G. Poste. Calcium-induced phase separation and fusion in phospholipid membranes. *Biophysical Journal*, 15(9):945–948, 1975. 1182269[pmid] Biophys J.
- [106] D. Papahadjopoulos, W. J. Vail, W. A. Pangborn, and G. Poste. Studies on membrane fusion. ii. induction of fusion in pure phospholipid membranes by calcium ions and other divalent metals. *Biochimica et Biophysica Acta (BBA) - Biomembranes*, 448(2):265–283, 1976.
- [107] Aniket Magarkar, Piotr Jurkiewicz, Christoph Allolio, Martin Hof, and Pavel Jungwirth. Increased binding of calcium ions at positively curved phospholipid membranes. *The Journal of Physical Chemistry Letters*, 8(2):518–523, 2017.
- [108] Pavel Jungwirth and Douglas J. Tobias. Specific ion effects at the air/water interface. *Chemical Reviews*, 106(4):1259–1281, 2006.
- [109] Cornelia G. Sinn, Markus Antonietti, and Rumiana Dimova. Binding of calcium to phosphatidylcholine–phosphatidylserine membranes. *Colloids and Surfaces A: Physicochemical and Engineering Aspects*, 282-283(Supplement C):410–419, 2006.
- [110] Maria Sovago, George W. H. Wurpel, Marc Smits, Michiel Müller, and Mischa Bonn. Calcium-induced phospholipid ordering depends on surface pressure. *Journal of the American Chemical Society*, 129(36):11079–11084, 2007.
- [111] Adéla Melcrová, Sarka Pokorna, Saranya Pullanchery, Miriam Kohagen, Piotr Jurkiewicz, Martin Hof, Pavel Jungwirth, Paul S. Cremer, and Lukasz Cwiklik. The complex nature of calcium cation interactions with phospholipid bilayers. *Scientific Reports*, 6:38035, 2016.

Bibliography

- [112] Gastone G. Celesia. Disorders of membrane channels or channelopathies. *Clinical Neurophysiology*, 112(1):2–18, 2001.
- [113] Christian A. Hübner and Thomas J. Jentsch. Ion channel diseases. *Human Molecular Genetics*, 11(20):2435–2445, 2002. 10.1093/hmg/11.20.2435.
- [114] B. Dworakowska and K. Dołowy. Ion channels-related diseases. *Acta biochimica Polonica*, 47(3):685–703, 2000.
- [115] David L. Browne, Stephen T. Gancher, John G. Nutt, Ewout R. P. Brunt, Eric A. Smith, Patricia Kramer, and Michael Litt. Episodic ataxia/myokymia syndrome is associated with point mutations in the human potassium channel gene, *kcna1*. *Nature Genetics*, 8:136, 1994.
- [116] Sue S. Chang, Stefan Grunder, Aaron Hanukoglu, Ariel Rösler, P. M. Mathew, Israel Hanukoglu, Laurent Schild, Yin Lu, Richard A. Shimkets, Carol Nelson-Williams, Bernard C. Rossier, and Richard P. Lifton. Mutations in subunits of the epithelial sodium channel cause salt wasting with hyperkalaemic acidosis, pseudohypoaldosteronism type 1. *Nature Genetics*, 12:248, 1996.
- [117] J. R. Riordan, J. M. Rommens, B. Kerem, N. Alon, R. Rozmahel, Z. Grzelczak, J. Zielenski, S. Lok, N. Plavsic, J. L. Chou, and et al. Identification of the cystic fibrosis gene: cloning and characterization of complementary dna. *Science*, 245(4922):1066, 1989.
- [118] B. A. Niemeyer, L. Mery, C. Zawar, A. Suckow, F. Monje, L. A. Pardo, W. Stuhmer, V. Flock-erzi, and M. Hoth. Ion channels in health and disease. 83rd boehringer ingelheim fonds international titisee conference. *EMBO reports*, 2(7):568–573, 2001. 11463739[pmid] PMC1083959[pmcid] 2/7/568[PII] EMBO Rep.
- [119] Nobuya Inagaki, Tohru Gono, John P. Clement, Noriyuki Namba, Johji Inazawa, Gabriela Gonzalez, Lydia Aguilar-Bryan, Susumu Seino, and Joseph Bryan. Reconstitution of *hHv1*: An inward rectifier subunit plus the sulfonylurea receptor. *Science*, 270(5239):1166, 1995.
- [120] Qing Wang, Jiayang Shen, Igor Splawski, Donald Atkinson, Zhizhong Li, Jennifer L. Robinson, Arthur J. Moss, Jeffrey A. Towbin, and Mark T. Keating. *Scn5a* mutations associated with an inherited cardiac arrhythmia, long qt syndrome. *Cell*, 80(5):805–811, 1995.
- [121] K. A. Quane, J. M. S. Healy, K. E. Keating, B. M. Manning, F. J. Couch, L. M. Palmucci, C. Doriguzzi, T. H. Fagerlund, K. Berg, H. Ording, D. Bendixen, W. Mortier, U. Linz, C. R. Muller, and T. V. McCarthy. Mutations in the ryanodine receptor gene in central core disease and malignant hyperthermia. *Nature Genetics*, 5:51, 1993.
- [122] Yilin Zhang, Hai Shiene Chen, Vijay K. Khanna, Stella De Leon, Michael S. Phillips, Keith Schappert, Beverley A. Britt, A. Keith W. Brownell, and David H. MacLennan. A mutation

- in the human ryanodine receptor gene associated with central core disease. *Nature Genetics*, 5:46, 1993.
- [123] Uwe Kornak, Dagmar Kasper, Michael R. Bösl, Edelgard Kaiser, Michaela Schweizer, Ansgar Schulz, Wilhelm Friedrich, Günter Delling, and Thomas J. Jentsch. Loss of the clc-7 chloride channel leads to osteopetrosis in mice and man. *Cell*, 104(2):205–215, 2001.
- [124] Eric Gouaux and Roderick MacKinnon. Principles of selective ion transport in channels and pumps. *Science*, 310(5753):1461, 2005.
- [125] J. E. Hall, I. Vodyanoy, T. M. Balasubramanian, and G. R. Marshall. Alamethicin. a rich model for channel behavior. *Biophysical Journal*, 45(1):233–247, 1984.
- [126] C. E. Meyer and F. Reusser. A polypeptide antibacterial agent isolated from *trichoderma viride*. *Experientia*, 23(2):85–86, 1967.
- [127] Paul Mueller and Donald O. Rudin. Action potentials induced in biomolecular lipid membranes. *Nature*, 217:713, 1968.
- [128] Moisés Eisenberg, James E. Hall, and C. A. Mead. The nature of the voltage-dependent conductance induced by alamethicin in black lipid membranes. *The Journal of Membrane Biology*, 14(1):143–176, 1973.
- [129] C. Li and T. Salditt. Structure of magainin and alamethicin in model membranes studied by x-ray reflectivity. *Biophysical Journal*, 91(9):3285–3300, 2006.
- [130] K. He, S. J. Ludtke, D. L. Worcester, and H. W. Huang. Neutron scattering in the plane of membranes: structure of alamethicin pores. *Biophysical Journal*, 70(6):2659–2666, 1996.
- [131] Robert O. Fox Jr and Frederic M. Richards. A voltage-gated ion channel model inferred from the crystal structure of alamethicin at 1.5-Å resolution. *Nature*, 300:325, 1982.
- [132] R. Latorre and O. Alvarez. Voltage-dependent channels in planar lipid bilayer membranes. *Physiological Reviews*, 61(1):77–150, 1981.
- [133] D. Chapman, R. J. Cherry, E. G. Finer, H. Hauser, M. C. Phillips, G. G. Shipley, and A. I. McMullen. Physical studies of phospholipid/alamethicin interactions. *Nature*, 224:692, 1969.
- [134] D. A. Haydon L. G. M. Gordon. Potential-dependent conductances in lipid membranes containing alamethicin. *Philosophical Transactions of the Royal Society of London. B, Biological Sciences*, 270(908):433, 1975.
- [135] Savko P. Schwarz, G. Structural and dipolar properties of the voltage-dependent pore former alamethicin in octanol/dioxane. *Biophysical Journal*, 39:211–219, 1982.

Bibliography

- [136] Gerhard Schwarz, Stefan Stankowski, and Vincenzo Rizzo. Thermodynamic analysis of incorporation and aggregation in a membrane: Application to the pore-forming peptide alamethicin. *Biochimica et Biophysica Acta (BBA) - Biomembranes*, 861:141–151, 1986.
- [137] Günther Boheim. Statistical analysis of alamethicin channels in black lipid membranes. *The Journal of Membrane Biology*, 19(1):277–303, 1974.
- [138] F. Salin, P. Georges, G. Roger, and A. Brun. Single-shot measurement of a 52-fs pulse. *Applied Optics*, 26(21):4528–4531, 1987.
- [139] Claude Rulliere. *Femtosecond Laser Pulses Principles and Experiments*. Springer-Verlag New York, 2005.
- [140] Carlos Macias-Romero, Marie E. P. Didier, Pascal Jourdain, Pierre Marquet, Pierre Magistretti, Orly B. Tarun, Vitalijs Zubkovs, Aleksandra Radenovic, and Sylvie Roke. High throughput second harmonic imaging for label-free biological applications. *Optics express*, 22(25):31102–12, 2014.
- [141] Periklis Pantazis, James Maloney, David Wu, and Scott E. Fraser. Second harmonic generating (shg) nanoprobe for in vivo imaging. *Proceedings of the National Academy of Sciences*, 107(33):14535, 2010.
- [142] Mark D. Peterson, Patrick L. Hayes, Imee Su Martinez, Laura C. Cass, Jennifer L. Achtyl, Emily A. Weiss, and Franz M. Geiger. Second harmonic generation imaging with a khz amplifier [invited]. *Optical Materials Express*, 1(1):57–66, 2011.
- [143] R. Le Harzic, I. Riemann, K. König, C. Wüllner, and C. Donitzky. Influence of femtosecond laser pulse irradiation on the viability of cells at 1035, 517, and 345nm. *Journal of Applied Physics*, 102(11):114701, 2007.
- [144] C. Macias-Romero, V. Zubkovs, S. Wang, and S. Roke. Wide-field medium-repetition-rate multiphoton microscopy reduces photodamage of living cells. *Biomedical Optics Express*, 7(4):1458–1467, 2016.
- [145] Anthony Yasmann and Sergei Sukharev. Properties of diphytanoyl phospholipids at the air–water interface. *Langmuir*, 31(1):350–357, 2015.
- [146] Thomas Gutschmann, Thomas Heimbürg, Ulrich Keyser, Kozhinjampara R. Mahendran, and Mathias Winterhalter. Protein reconstitution into freestanding planar lipid membranes for electrophysiological characterization. *Nature Protocols*, 10(1):188–198, 2014.
- [147] a V. Krylov, P. Pohl, M. L. Zeidel, and W. G. Hill. Water permeability of asymmetric planar lipid bilayers: leaflets of different composition offer independent and additive resistances to permeation. *The Journal of general physiology*, 118(4):333–340, 2001.
- [148] Andreas Horner, Sergey A. Akimov, and Peter Pohl. Long and short lipid molecules experience the same interleaflet drag in lipid bilayers. *Physical Review Letters*, 110(26):268101, 2013. PRL.

- [149] S. H. White, D. C. Petersen, S. Simon, and M. Yafuso. Formation of planar bilayer membranes from lipid monolayers. a critique. *Biophysical journal*, 16(5):481–489, 1976.
- [150] HEKA Elektronik. *PATCHMASTER Reference Manual*. Elektronik, Heka GmbH, Schulze, Germany.
- [151] Manfred Lindau and Erwin Neher. Patch-clamp techniques for time-resolved capacitance measurements in single cells. *Pflügers Archiv*, 411(2):137–146, 1988.
- [152] C. Joshi and J. M. Fernandez. Capacitance measurements. an analysis of the phase detector technique used to study exocytosis and endocytosis. *Biophysical journal*, 53(6):885–892, 1988. 3395658[pmid] PMC1330269[pmcid] S0006-3495(88)83169-2[PII] Biophys J.
- [153] Markin VS Sokolov VS, Cherny VV. Measurements by inner field compensation method of the potential induced by phloretin and phloretin adsorption on blm. *Biofizika*, 29:424–429, 1984.
- [154] Peter Pohl, Tatyana I. Rokitskaya, Elena E. Pohl, and Sapar M. Saparov. Permeation of phloretin across bilayer lipid membranes monitored by dipole potential and microelectrode measurements. *Biochimica et Biophysica Acta (BBA) - Biomembranes*, 1323(2):163–172, 1997.
- [155] Dawn L. Brasaemle. The perilipin family of structural lipid droplet proteins: Stabilization of lipid droplets and control of lipolysis. *Journal of Lipid Research*, 2007.
- [156] Amit Kessel, David S. Cafiso, and Nir Ben-Tal. Continuum solvent model calculations of alamethicin-membrane interactions: Thermodynamic aspects. *Biophysical Journal*, 78(2):571–583, 2000.
- [157] Derek Marsh, Micha Jost, Cristina Peggion, and Claudio Toniolo. Lipid chain-length dependence for incorporation of alamethicin in membranes: Electron paramagnetic resonance studies on toac-spin labeled analogs. *Biophysical Journal*, 92(11):4002–4011, 2007.
- [158] Wolfgang H. Binder, Veronique Barragan, and Fredric M. Menger. Domains and rafts in lipid membranes. *Angew. Chem., Int. Ed.*, 42(47):5802–5827, 2003.
- [159] Nikolay Smolentsev, Cornelis Lütgebaucks, Halil I. Okur, Alex G. F. de Beer, and Sylvie Roke. Intermolecular headgroup interaction and hydration as driving forces for lipid transmembrane asymmetry. *Journal of the American Chemical Society*, 138(12):4053–4060, 2016.
- [160] James C. S. Ho, Padmini Rangamani, Bo Liedberg, and Atul N. Parikh. Mixing water, transducing energy, and shaping membranes: Autonomously self-regulating giant vesicles. *Langmuir*, 32(9):2151–2163, 2016.

Bibliography

- [161] M. I. Angelova, S. Soléau, Ph Méléard, F. Faucon, and P. Bothorel. *Preparation of giant vesicles by external AC electric fields. Kinetics and applications*. Trends in Colloid and Interface Science VI. Steinkopff, Darmstadt, 1992.
- [162] Sebastian Leptihn, Oliver K. Castell, Brid Cronin, En-Hsin Lee, Linda C. M. Gross, David P. Marshall, James R. Thompson, Matthew Holden, and Mark I. Wallace. Constructing droplet interface bilayers from the contact of aqueous droplets in oil. *Nature Protocols*, 8:1048, 2013.
- [163] S.H. White. Studies of the physical chemistry of planar bilayer membranes using high precision measurements of specific capacitance. *Annals of the New York Academy of Sciences*, 303:243–265, 1977.
- [164] R. Benz, O. Fröhlich, P. Läuger, and M. Montal. Electrical capacity of black lipid films and of lipid bilayers made from monolayers. *Biochimica et Biophysica Acta (BBA) - Biomembranes*, 394(3):323–334, 1975.
- [165] Stephen H. White. Ion channel reconstitution. *Ion Channel Reconstitution*, pages 3–34, 1986.
- [166] Paolo F. Almeida, Winchil L. Vaz, and T.E Thomson. Lateral diffusion in the liquid phases of dimyristoylphosphatidylcholine/cholesterol lipid bilayers: A free volume analysis. *Biochemistry*, 32:6739–6747, 1992.
- [167] Eric Tyrode, Mark W. Rutland, and Colin D. Bain. Adsorption of ctab on hydrophilic silica studied by linear and nonlinear optical spectroscopy. *Journal of the American Chemical Society*, 130(51):17434–17445, 2008.
- [168] S. Roke. Nonlinear optical spectroscopy of soft matter interfaces. *Chemphyschem*, 10(9-10):1380–1388, 2009.
- [169] Joanna L. Richens, Jordan S. Lane, Melissa L. Mather, and Paul O’Shea. The interactions of squalene, alkanes and other mineral oils with model membranes; effects on membrane heterogeneity and function. *Journal of Colloid and Interface Science*, 457:225–231, 2015.
- [170] Pontus Boström, Linda Andersson, Mikael Rutberg, Jeanna Perman, Ulf Lidberg, Bengt R. Johansson, Julia Fernandez-Rodriguez, Johanna Ericson, Tommy Nilsson, Jan Borén, and Sven-Olof Olofsson. Snare proteins mediate fusion between cytosolic lipid droplets and are implicated in insulin sensitivity. *Nature Cell Biology*, 9:1286, 2007.
- [171] Miroslava Spanova, Dagmar Zweytick, Karl Lohner, Lisa Klug, Erich Leitner, Albin Hermetter, and Günther Daum. Influence of squalene on lipid particle/droplet and membrane organization in the yeast *saccharomyces cerevisiae*. *Biochimica et Biophysica Acta*, 1821(4):647–653, 2012. S1388-1981(12)00020-0[PII] 22342273[pmid] *Biochim Biophys Acta*.

- [172] Gerrit van Meer and Anton I. P. M. de Kroon. Lipid map of the mammalian cell. *Journal of Cell Science*, 124(1):5–8, 2010.
- [173] Derek Marsh. *Handbook of Lipid Bilayers, Second Edition*. CRC Press, 2013.
- [174] John David Jackson. *Classical Electrodynamics, Third Edition*. Wiley, 1998.
- [175] Alla Kress, Xiao Wang, Hubert Ranchon, Julien Savatier, Hervé Rigneault, Patrick Ferland, and Sophie Brasselet. Mapping the local organization of cell membranes using excitation-polarization-resolved confocal fluorescence microscopy. *Biophysical Journal*, 105(1):127–136, 2013. S0006-3495(13)00630-9[PII] 23823231[pmid] Biophys J.
- [176] Jonas Korklach, Petra Schwille, Watt W. Webb, and Gerald W. Feigenson. Characterization of lipid bilayer phases by confocal microscopy and fluorescence correlation spectroscopy. *Proceedings of the National Academy of Sciences of the United States of America*, 96(15):8461–8466, 1999. 2122[PII] 10411897[pmid] Proc Natl Acad Sci U S A.
- [177] Jin Liu and John C. Conboy. Direct measurement of the transbilayer movement of phospholipids by sum-frequency vibrational spectroscopy. *Journal of the American Chemical Society*, 126(27):8376–8377, 2004.
- [178] Anibal E. Dissalvo. *Membrane Hydration The Role of Water in the Structure and Function of Biological Membranes*, volume 71 of *Subcellular Chemistry*. Springer International Publishing, 2015.
- [179] R. Bersohn, Yoh-Han Pao, and H. L. Frisch. Double-quantum light scattering by molecules. *The Journal of Chemical Physics*, 45(9):3184–3198, 1966.
- [180] Halil I. Okur, Jaibir Kherb, and Paul S. Cremer. Cations bind only weakly to amides in aqueous solutions. *Journal of the American Chemical Society*, 135(13):5062–5067, 2013.
- [181] F. C. Tsui, D. M. Ojcius, and W. L. Hubbell. The intrinsic pka values for phosphatidylserine and phosphatidylethanolamine in phosphatidylcholine host bilayers. *Biophysical Journal*, 49(2):459–468, 1986. 3955180[pmid] Biophys J.
- [182] Erdinc Sezgin, Ilya Levental, Michal Grzybek, Günter Schwarzmann, Veronika Mueller, Alf Honigmann, Vladimir N. Belov, Christian Eggeling, Ünal Coskun, Kai Simons, and Petra Schwille. Partitioning, diffusion, and ligand binding of raft lipid analogs in model and cellular plasma membranes. *Biochimica et Biophysica Acta (BBA) - Biomembranes*, 1818(7):1777–1784, 2012.
- [183] A. S. Klymchenko and Rémy Kreder. Fluorescent probes for lipid rafts: From model membranes to living cells. *Chemistry and Biology*, 21(1):97–113, 2014.
- [184] C. H. Lee, R. K. Chang, and N. Bloembergen. Nonlinear electroreflectance in silicon and silver. *Physical Review Letters*, 18(5):167–170, 1967. PRL.

Bibliography

- [185] Grazia Gonella, Cornelis Lütgebaucks, Alex G. F. de Beer, and Sylvie Roke. Second harmonic and sum-frequency generation from aqueous interfaces is modulated by interference. *The Journal of Physical Chemistry C*, 120(17):9165–9173, 2016.
- [186] Gerald S. Manning. Counterion condensation on charged spheres, cylinders, and planes. *The Journal of Physical Chemistry B*, 111(29):8554–8559, 2007.
- [187] James Hall Ramon Latorre. Dipole potential measurements in asymmetric membranes. *Nature*, 264:361–363, 1976.
- [188] Sven O. Hagge, Andre Wiese, Ulrich Seydel, and Thomas Gutschmann. Inner field compensation as a tool for the characterization of asymmetric membranes and peptide-membrane interactions. *Biophysical journal*, 86(2):913–22, 2004.
- [189] Joseph M. Crowley. Electrical breakdown of bimolecular lipid membranes as an electromechanical instability. *Biophysical Journal*, 13(7):711–724, 1973. 4715586[pmid] Biophys J.
- [190] A. Engel and D. J. Muller. Observing single biomolecules at work with the atomic force microscope. *Nat Struct Biol*, 7(9):715–8, 2000. Engel, A Muller, D J Research Support, Non-U.S. Gov't Review United States Nat Struct Biol. 2000 Sep;7(9):715-8.
- [191] Ralf P. Richter and Alain R. Brisson. Following the formation of supported lipid bilayers on mica: A study combining afm, qcm-d, and ellipsometry. *Biophysical Journal*, 88(5):3422–3433, 2005.
- [192] Fatemeh Ahmadpoor and Pradeep Sharma. Flexoelectricity in two-dimensional crystalline and biological membranes. *Nanoscale*, 7(40):16555–16570, 2015.
- [193] Supriyo Ray, Adam Kassar, Anna R. Busija, Padmini Rangamani, and Hemal H. Patel. The plasma membrane as a capacitor for energy and metabolism. *American journal of physiology. Cell physiology*, 310(3):C181–C192, 2016. 26771520[pmid] PMC4888523[pmcid] ajpcell.00087.2015[PII] Am J Physiol Cell Physiol.
- [194] Andreas Horner, Christine Siligan, Alex Cornean, and Peter Pohl. Positively charged residues at the channel mouth boost single-file water flow. *Faraday Discussions*, 209(0):55–65, 2018.
- [195] Darcy S. Peterka, Hiroto Takahashi, and Rafael Yuste. Imaging voltage in neurons. *Neuron*, 69(1):9–21, 2011.
- [196] Andreas Horner, Florian Zocher, Johannes Preiner, Nicole Ollinger, Christine Siligan, Sergey A. Akimov, and Peter Pohl. The mobility of single-file water molecules is governed by the number of h-bonds they may form with channel-lining residues. *Science Advances*, 1(2), 2015.

- [197] Sandhya Gopalakrishnan, Dingfang Liu, Heather C. Allen, Margaret Kuo, and Mary Jane Shultz. Vibrational spectroscopic studies of aqueous interfaces: salts, acids, bases, and nanodrops. *Chemical Reviews*, 106(4):1155–1175, 2006.
- [198] Yu-Hsiu Wang, Agnieszka Collins, Lin Guo, Kathryn B. Smith-Dupont, Feng Gai, Tatyana Svitkina, and Paul A. Janmey. Divalent cation-induced cluster formation by polyphosphoinositides in model membranes. *Journal of the American Chemical Society*, 134(7):3387–3395, 2012.
- [199] Karim El Kirat, Françoise Besson, Annie-France Prigent, Jean-Paul Chauvet, and Bernard Roux. Role of calcium and membrane organization on phospholipase d localization and activity: Competition between a soluble and an insoluble substrate. *Journal of Biological Chemistry*, 277(24 <http://www.jbc.org/content/277/24/21231.abstract>):21231–21236, 2002. 10.1074/jbc.M106449200.
- [200] David J. Griffiths. *Introduction to Electrodynamics, 4th edition*. CAMBRIDGE UNIVERSITY PRESS, Cambridge, United Kingdom.
- [201] Jordi Farauo and Alex Travesset. Phosphatidic acid domains in membranes: Effect of divalent counterions. *Biophysical Journal*, 92(8):2806–2818, 2007.
- [202] Jeanne C. Stachowiak, Frances M. Brodsky, and Elizabeth A. Miller. A cost-benefit analysis of the physical mechanisms of membrane curvature. *Nat. Cell Biol.*, 15(9):1019–1027, 2013.
- [203] Isak Bivas. Electrostatic and mechanical properties of a flat lipid bilayer containing ionic lipids: Possibility for formation of domains with different surface charges. *Colloids Surf. A Physicochem. Eng. Asp.*, 282-283:423–434, 2006.
- [204] David Steigmann and Ashutosh Agrawal. Electromechanics of polarized lipid bilayers. *Mathematics and Mechanics of Complex Systems*, 4(1):31–54, 2016.
- [205] Alexander G. Petrov. Flexoelectricity of model and living membranes. *Biochimica et Biophysica Acta (BBA) - Biomembranes*, 1561(1):1–25, 2002.
- [206] I. Bivas and M. M. Kozlov. Effect of flexoelectricity on the curvature elasticity of the membrane. *Liq. Cryst.*, 8(6):813–817, 1990.
- [207] Padmini Rangamani, Ashutosh Agrawal, Kranthi K. Mandadapu, George Oster, and David J. Steigmann. Interaction between surface shape and intra-surface viscous flow on lipid membranes. *Biomechanics and Modeling in Mechanobiology*, 12(4):833–845, 2013.
- [208] Reinhard Lipowsky. Spontaneous tubulation of membranes and vesicles reveals membrane tension generated by spontaneous curvature. *Faraday Discussions*, 161(0):305–331, 2013.

Bibliography

- [209] N. O. Petersen, P. L. Höddelius, P. W. Wiseman, O. Seger, and K. E. Magnusson. Quantitation of membrane receptor distributions by image correlation spectroscopy: concept and application. *Biophysical Journal*, 65(3):1135–1146, 1993. 8241393[pmid] Biophys J.
- [210] Benedict Hebert, Santiago Costantino, and Paul W. Wiseman. Spatiotemporal image correlation spectroscopy (stics) theory, verification, and application to protein velocity mapping in living cho cells. *Biophysical Journal*, 88(5):3601–3614, 2005. 54874[PII] 15722439[pmid] Biophys J.
- [211] David L. Kolin, David Ronis, and Paul W. Wiseman. k-space image correlation spectroscopy: A method for accurate transport measurements independent of fluorophore photophysics. *Biophysical Journal*, 91(8):3061–3075, 2006. 82768[PII] 16861272[pmid] Biophys J.
- [212] D. L. Kolin and P. W. Wiseman. *Advances in image correlation spectroscopy: measuring number densities, aggregation states, and dynamics of fluorescently labeled macromolecules in cells*. 2007.
- [213] Paul W. Wiseman, Claire M. Brown, Donna J. Webb, Benedict Hebert, Natalie L. Johnson, Jeff A. Squier, Mark H. Ellisman, and A. F. Horwitz. Spatial mapping of integrin interactions and dynamics during cell migration by image correlation microscopy. *Journal of Cell Science*, 117(23):5521, 2004.
- [214] Paul W. Wiseman. Image correlation spectroscopy: Principles and applications. *Cold Spring Harbor Protocols*, 2015(4):pdb.top086124, 2015.
- [215] T. R. Gaborski, M. N. Sealander, M. Ehrenberg, R. E. Waugh, and J. L. McGrath. Image correlation microscopy for uniform illumination. *Journal of microscopy*, 237(1):39–50, 2010. 20055917[pmid] PMC3147011[pmcid] JMI3300[PII] J Microsc.
- [216] Alex Herbert. Genome damage and stability center (gdsc) plugin.
- [217] David Gardner. Characterizing digital cameras with the photon transfer curve.
- [218] *Neuroscience, 2nd edition*. Sinauer Associates, Inc., Sunderland, Massachusetts, USA, 2001.
- [219] M. Dal Peraro and F. G. van der Goot. Pore-forming toxins: ancient, but never really out of fashion. *Nature Reviews Microbiology*, 14(2):77–92, 2016.
- [220] P. Kongsuphol, K. B. Fang, and Z. P. Ding. Lipid bilayer technologies in ion channel recordings and their potential in drug screening assay. *Sensors and Actuators B-Chemical*, 185:530–542, 2013.
- [221] P. K. Hansma, B. Drake, O. Marti, S. A. C. Gould, and C. B. Prater. The scanning ion-conductance microscope. *Science*, 243(4891):641–643, 1989.

- [222] J. Dunlop, M. Bowlby, R. Peri, D. Vasilyev, and R. Arias. High-throughput electrophysiology: an emerging paradigm for ion-channel screening and physiology. *Nature Reviews Drug Discovery*, 7(4):358–368, 2008.
- [223] C. A. Thomas, P. A. Springer, L. M. Okun, Berwaldn.Y, and G. E. Loeb. Miniature microelectrode array to monitor bioelectric activity of cultured cells. *Experimental Cell Research*, 74(1):61–, 1972.
- [224] M. E. Spira and A. Hai. Multi-electrode array technologies for neuroscience and cardiology. *Nature Nanotechnology*, 8(2):83–94, 2013.
- [225] R. S. Eisenberg. From structure to function in open ionic channels. *Journal of Membrane Biology*, 171(1):1–24, 1999.
- [226] M. O. Jensen, V. Jogini, D. W. Borhani, A. E. Leffler, R. O. Dror, and D. E. Shaw. Mechanism of voltage gating in potassium channels. *Science*, 336(6078):229–233, 2012.
- [227] E. Khurana, M. Dal Peraro, R. DeVane, S. Vemparala, W. F. DeGrado, and M. L. Klein. Molecular dynamics calculations suggest a conduction mechanism for the m2 proton channel from influenza a virus. *Proceedings of the National Academy of Sciences of the United States of America*, 106(4):1069–1074, 2009.
- [228] S. Capponi, M. Heyden, A. N. Bondar, D. J. Tobias, and S. H. White. Anomalous behavior of water inside the secy translocon. *Proceedings of the National Academy of Sciences of the United States of America*, 112(29):9016–9021, 2015.
- [229] Shuji Ye, Hongchun Li, Feng Wei, Joshua Jasensky, Andrew P. Boughton, Pei Yang, and Zhan Chen. Observing a model ion channel gating action in model cell membranes in real time in situ: Membrane potential change induced alamethicin orientation change. *Journal of the American Chemical Society*, 134(14):6237–6243, 2012.
- [230] Istvan Kocsis, Mirco Sorci, Heather Vanselous, Samuel Murail, Stephanie E. Sanders, Erol Licsandru, Yves-Marie Legrand, Arie van der Lee, Marc Baaden, Poul B. Petersen, Georges Belfort, and Mihail Barboiu. Oriented chiral water wires in artificial transmembrane channels. *Science Advances*, 4(3), 2018.
- [231] Günther Boehm and Hans-Albert Kolb. Analysis of the multi-pore system of alamethicin in a lipid membrane. *The Journal of Membrane Biology*, 38(1):99–150, 1978.
- [232] D. S. Cafiso. Alamethicin: A peptide model for voltage gating and protein-membrane interactions. *Annual Review of Biophysics and Biomolecular Structure*, 23(1):141–165, 1994.
- [233] Yixing Chen, Halil I. Okur, Chungwen Liang, and Sylvie Roke. Orientational ordering of water in extended hydration shells of cations is ion-specific and is correlated directly with viscosity and hydration free energy. *Physical Chemistry Chemical Physics*, 19(36):24678–24688, 2017.

Bibliography

- [234] R. W. Impey, P. A. Madden, and I. R. McDonald. Hydration and mobility of ions in solution. *The Journal of Physical Chemistry*, 87(25):5071–5083, 1983.
- [235] M. E. P. Didier, O. B. Tarun, P. Jourdain, P. Magistretti, and S. Roke. Membrane water for probing neuronal membrane potentials and ionic fluxes at the single cell level. *Nature Communications*, 9(1):5287, 2018.

Orly Tarun

Chemin des Côtes 74
1020 Renens

Mobile: +41 (0)79 651 28 17
Email: orly.tarun@gmail.com

Birthdate: 16.06.1987
Marital status: Single



Education

- 2014 – 2019 **Ph.D** in Photonics, École Polytechnique Fédérale de Lausanne, Switzerland
2010 – 2013 **M. Sc.** in Physics, University of the Philippines Diliman, Philippines
2004 – 2009 **B. Sc.** in Applied Physics, University of the Philippines Diliman, Philippines

Professional experiences

- 2010 – 2014 **Jr. Test Engineer** (2010-2012), **Sr. Test Engineer** (2012-2014) HGST, a Western Digital Company, Philippines.
Together with three engineers, we pioneered the design, conceptualization, construction and operation of a testing facility to qualify the reliability of prototype hard disk drives. As a test engineer, I primarily developed and designed new testing protocols for prototype products. As a whole, I lead the maintenance of testing equipment (gage repeatability and reproducibility), testing of new designs, writing technical reports and interacting with customers.

Awards and Honors

- 2019 Winner of an **Enable** grant (EPFL). Enable “invests in tomorrow’s technology.”
2018 **Invited Speaker** at the International Conference on Non-equilibrium Dynamics of Condensed Matter in the Time Domain, Kerkrade, Netherlands.
2018 **Invited Speaker** at the 13th Annual Water Conference, Sofia, Bulgaria.
2018 **Best Poster Prize**: Physical Approaches to Membrane Asymmetry, Germany.
2013 **Most Outstanding Master of Science in Physics** of 2013.
2009 Bachelor graduate with great honor (**Magna cum Laude**), <7% of all graduates.
2005 University of the Philippines Presidential Scholarship
2003 Best in Applied Science Research, Intel Philippines National Level Science Fair
2000 Philippine Science High School Scholar

Journal Publications

- O. B. Tarun**, C. Hanneschläger, P. Pohl, S. Roke. *Proceedings of the National Academy of Sciences*, 115(16), 4081 (2018).
 - Featured in more than 10 news outlet: <https://actu.epfl.ch/news/using-water-molecules-to-read-electrical-activity/>
- M. Didier, **O. B. Tarun**, P. Jourdain, P. Magistretti, S. Roke. *Nature Communications*, 9(1), 5287 (2018).
 - Featured in more than 10 news outlet: <https://actu.epfl.ch/news/using-water-molecules-to-unlock-neurons-secrets/>
- O. B. Tarun**, M. Yu Eremchev, S. Roke. *Langmuir*, 34, 11305-11310 (2018).
O. B. Tarun. 256th National Meeting and Exposition of the American-Chemical-Society (ACS) - *Nanoscience, Nanotechnology and Beyond* (2018).
C. Macias-Romero, M. E. P. Didier, P. Jourdain, P. Marquet, P. Magistretti, **O. B. Tarun**, V.

Zubkovs, A. Radenovic, S. Roke. *Optics express* 22, 31102-31112 (2014).
O. B. Tarun, Nichols M. A. *IEEE Transactions on Magnetism* 49(6): 2870-2872 (2013).
O. B. Tarun, Nichols MA A. *IEEE Transactions on Magnetism* 49(12): 5616-5619 (2013).
O. B. Tarun, M.Yu. Eremchev, A. Radenovic, and S. Roke. Spatiotemporal imaging of water in operating voltage-gated ion channels reveals the slow motion of interfacial ions. *Submitted* (2019).
O. B. Tarun, H. I. Okur, P. Rangamani, S. Roke. Membrane diversification by transient ion-induced ordered water domains. *Submitted* (2018).

Key skills and certifications

Instrumentation: Optics, nonlinear microscopy (second harmonic generation, two-photon fluorescence), nonlinear spectroscopy (second harmonic scattering), linear microscopy derivatives, signal and image processing, data analysis.

Certifications:

- “Think Like a GM” by Harvard Business Publishing and John Clements.
- Management of Innovation and Technology Transfer (EPFL).
- Innosuisse Business Concept (EPFL).
- Entrepreneurial Opportunity Identification and Exploitation (EPFL).
- Trained Lean Six Sigma Green Belt.

Testing and design of experiments: Extensive knowledge in testing, in particular I worked with prototype designs of hard disk drives.

IT: Languages: C, C++; Software: Matlab, Mathematica, Python, ImageJ, MS Office, LaTeX, Adobe Illustrator, Photoshop, SolidWorks; Web development: PHP & MySQL.

Selected Scientific Conferences

- International Conference on Non-equilibrium Dynamics of Condensed Matter in the Time Domain, Kerkrade, Netherlands (2018).
- 13th Annual Water Conference, Sofia, Bulgaria (2018).
- Physical Approaches to Membrane Asymmetry, 665 WE-Heraeus-Seminar, DE (2018).
- The International Conference on Optics of Surfaces and Interfaces, Texas, USA (2015).
- Sum frequency spectroscopy workshop, Wiesbaden, Naurod, DE (2015).

Teaching Activities

2015 – 2018 Teaching Assistant: “Interfaces for Biology and Nanotechnology (IBN)”, Bachelor course, EPFL
2017 – 2018 Teaching Assistant: “Phys-608 Nonlinear optics” PhD course, EPFL.

Research Affiliations

Member of the Laboratory for Fundamental Biophotonics, lbp.epfl.ch, (2014-present).
Member of the Swiss Chemical Society (scg.ch), (2016-present).
Member of the Instrumentation Physics Laboratory, University of the Philippines, (2007-2010).

Languages

English Fluent (written and oral, C2); **French** Working proficiency; **Filipino** Mother tongue

